Studies of positron identification with the PAMELA calorimeter
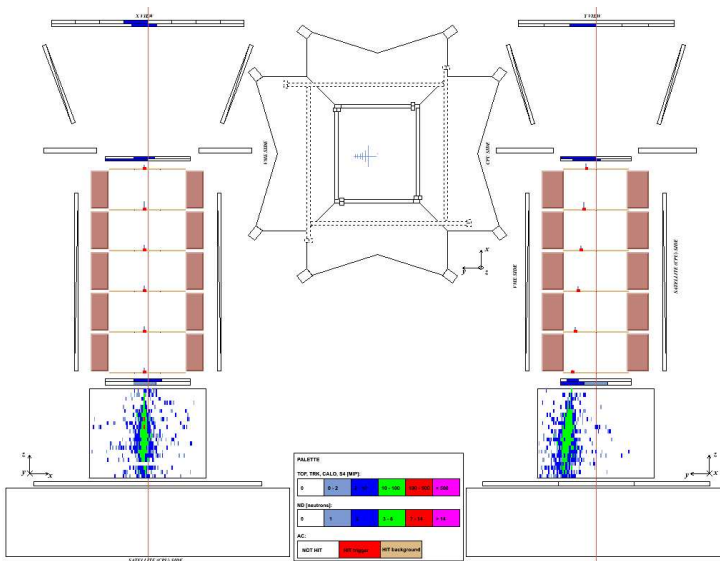
LAURA ROSSETTO

Licentiate Thesis
Stockholm, Sweden 2010

KTH
VETENSKAP
OCH KONST

KTH Engineering Sciences

Licentiate Thesis

Studies of positron identification with the PAMELA calorimeter

Laura Rossetto

Particle and Astroparticle Physics, Department of Physics,
Royal Institute of Technology, SE-106 91 Stockholm, Sweden

Stockholm, Sweden 2010

Cover illustration: Hadronic shower development in the PAMELA calorimeter initiated by a proton with a tracker reconstructed rigidity of 41.6 GV. The event was generated by simulations where all the charged pions were modified into neutral ones.

Akademisk avhandling som med tillstånd av Kungliga Tekniska Högskolan i Stockholm framlägges till offentlig granskning för avläggande av teknologie doktorsexamen onsdagen den 10 november 2010 kl 13:00 i sal FB42, AlbaNova Universitetscentrum, Roslagstullsbacken 21, Stockholm.

Avhandlingen försvaras på engelska.

Abstract

PAMELA is a satellite-borne experiment mounted on board of the Russian Resurs DK1 satellite which was launched from the Baikonur cosmodrome in Kazakhstan on June 15th 2006. The satellite orbits around the Earth on a semi-polar and elliptical trajectory and PAMELA has been acquiring data for approximately four years. The detector was designed and optimised for the study of the antimatter component in the cosmic radiation. The PAMELA apparatus consists of a time-of-flight system, a permanent magnetic spectrometer, an electromagnetic calorimeter, a neutron detector and an anticoincidence system. Combining information from different detectors and in particular from the calorimeter, positrons can be identified from the significant background due to cosmic ray protons.

Simulations of electromagnetic and hadronic interactions in the calorimeter were performed with the purpose of studying π^0 production in hadronic cascades within the context of positron identification. The number of π^0s produced in hadronic showers was artificially boosted in order to study the consequences for positron identification. The positron selection criteria used to produce the widely discussed positron fraction published by the PAMELA Collaboration in 2009 were applied to simulations in the energy range $20 - 100$ GeV. Results of this analysis show that the reported rise in the positron fraction cannot be accounted for by π^0 contamination.

A new approach for positron identification based on shower profile variables in the calorimeter has been studied with the aim of extending positron identification beyond 100 GeV. The proton-to-positron flux ratio is $\sim 10^4$ at 100 GV. In the energy range $20 - 100$ GeV a positron selection efficiency of ~ 0.50 was found together with a proton contamination of order of 10^{-5}.

iv

Contents

Introduction

Outline of the thesis

The work presented in this thesis concerns simulation studies of hadronic and electromagnetic showers in the calorimeter of the PAMELA satellite experiment. The goal is to study potential proton contamination in positron identification due to neutral pion production. In chapter 1 basic concepts and features of cosmic rays are presented together with a description of acceleration and propagation mechanisms throughout the galaxy. Particular attention is focused on cosmic ray positrons and on the positron fraction published by the PAMELA Collaboration in 2009. Chapter 2 is dedicated to a detailed description of the components which constitute the PAMELA experiment. The main scientific goals are briefly summarized together with performance for the detection of cosmic ray particles and antiparticles. In chapter 3 electromagnetic and hadronic shower development inside the calorimeter are described; neutral pion contamination in hadronic showers is also presented. Furthermore, a detailed description of the transverse shower profile variables used in the analysis work is presented. Chapter 4 is dedicated to GEANT3 simulation studies of hadronic and electromagnetic showers induced by protons and positrons inside the calorimeter. Positron selection criteria used to derive the published PAMELA positron fraction are then presented and applied to the simulated samples. A new approach using shower profile variables in the calorimeter is also described: the purpose of this analysis was to study a method for discriminating positrons and protons which is also applicable at higher energies (> 100 GeV).

The author's contribution

I joined the PAMELA Collaboration in October 2007 when I started working as a PhD student in the Astroparticle and Particle Physics group at KTH. The first year was mainly focused on learning about the PAMELA experiment. Some months were spent studying the so-called $p\beta$ method applied to the PAMELA calorimeter in order to separate particles and antiparticles with same charge but different mass. The analysis was performed on simulations of antiprotons and negative pions which I produced. This analysis was documented as a PAMELA Collaboration note but

is not described further in this thesis. In the second year of my PhD I started working on simulations which focused on the study of neutral pion production in hadronic showers inside the calorimeter. I used the PAMELA Collaboration's official simulation code and I modified it in order to artificially increase the number of neutral pions produced in hadronic showers and study the consequences for positron identification. I studied and applied to my simulations standard positron selection criteria used by the Collaboration in the positron analysis. I also developed new selection criteria in the calorimeter with the goal of obtaining an efficient positron selection efficiency with less proton contamination, with a view to extending this analysis to higher energies.

The work presented in this thesis was presented at several PAMELA Collaboration meetings and it will be part of a future publication concerning the high energy behaviour of the positron fraction and the absolute positron flux.

I am co-author of the following articles published by the PAMELA Collaboration:

- O. Adriani et al. *Measurements of quasi-trapped electron and positron fluxes with PAMELA*. Journal of Geophysical Research, **114**: A12218, 2009.

- O. Adriani et al. *A statistical procedure for the identification of positrons in the PAMELA experiment*. Astroparticle Physics, **34**: $1 - 11$, 2010.

- O. Adriani et al. *PAMELA Results on the Cosmic-Ray Antiproton Flux from 60 MeV to 180 GeV in Kinetic Energy*. Physical Review Letters, **105**: $121101-1 - 5$, 2010.

Chapter 1

Cosmic rays

Cosmic rays are high energy particles travelling through outer space and arriving at the Earth. About 98 % of these particles are *protons* and *nuclei* while about 2 % are *electrons*. The hadronic component comprises protons ($\sim$ 87 %), helium nuclei ($\sim$ 12 %) and heavier nuclei ($\sim$ 1 %) [1]. These particles come from galactic or extragalactic astrophysical sources and are so called *primary* cosmic rays. They are deflected by magnetic fields and thus travel a random path before arriving to the Earth. Along this path they can interact with the interstellar medium and create *secondary* particles. Also, when these high energy particles enter the Earth's atmosphere, they collide with the molecules of atmospheric gases and produce a shower of lower energy particles called *Extensive Air Showers*. Only particles with energy greater than 10^{14} eV generate particle showers which can pass through all the atmosphere and can be detected by surface array detectors. Particles with energy below 10^{14} eV can only be detected outside the atmosphere using balloon-borne or satellite experiments.

In this first chapter basic concepts and features of cosmic rays are presented together with some recent experimental results. Particular attention is focused on the results published by the PAMELA collaboration.

1.1   The energy spectrum

The cosmic ray energy spectrum extends from E $\sim$ 10^8 eV up to E $\sim$ 10^{20} eV. Figure 1.1 shows the all particle energy spectrum of cosmic rays [2].

The energy spectrum is well represented by a power-law distribution $I(E) \propto E^{-\alpha}$ but two changes in the spectral index are visible. For E > 10^9 eV the spectrum has a spectral index α = 2.7; the spectrum becomes then steeper at E $\sim$ 3 $\cdot 10^{15}$ eV with a spectral index α = 3.1: this is the so called *knee* of the spectrum. The spectral index changes again around 10^{18} eV, the so called *ankle* of the spectrum [3]. Recent measurements obtained from the Pierre Auger Observatory show that the
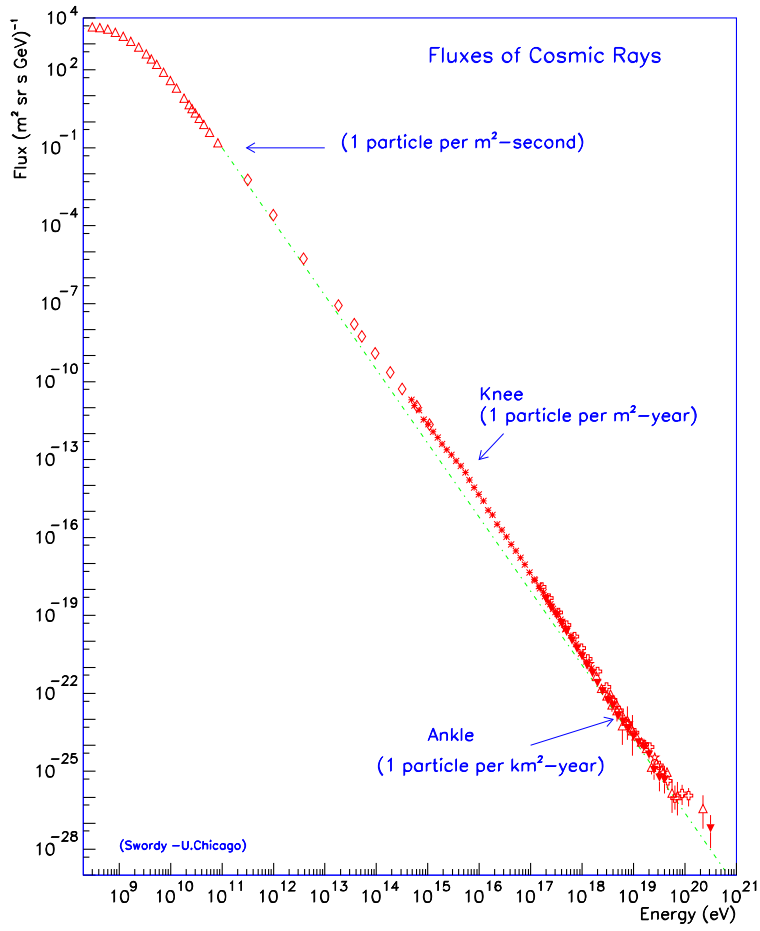
Figure 1.1. The all particle energy spectrum of cosmic rays [2].

ankle is located at E $= 10^{18.6}$ eV and that the spectral index is $\alpha \sim 3.3$ below the ankle and $\alpha \sim 2.6$ above the ankle [4].

The origin of the knee and the ankle in the cosmic ray energy spectrum is still unknown but there are theories which provide several explanations. For instance, the knee energy could represent the boundary between particles accelerated inside our galaxy and those of extragalactic origin. In our galaxy cosmic rays can be accelerated up to an energy $E_{max} \propto Z \cdot (L \cdot B)$ which depends on the size L and the magnetic field strength B of the acceleration region and on the charge Z of the primary particle. Another theory is that particles are constrained within the galaxy by the galactic magnetic field up to the knee energy, i.e. $E_{max} \approx Z \cdot 3 \cdot 10^{15}$ eV. The knee energy depends on the charge Z of the primary particle and thus the knee is expected at higher energies for particles with higher Z values. Data from Extensive Air Showers detected by the EAS-TOP array show a dominance of helium primaries around the knee at $3.5 \cdot 10^{15}$ eV; they indicate also the knee energy for elements like carbon, nitrogen and oxygen to be around $(6 - 7) \cdot 10^{15}$ eV [5]. Furthermore measurements from the KASCADE array show the knee at $(3 - 5) \cdot 10^{15}$ eV to be caused by a steepening in the light-element spectra (mostly hydrogen and helium) [6], [7]. Unfortunately, a change in the spectral index for heavier mass primary particles it has not been found yet: recent measurements performed by the KASCADE-Grande array do not show any change in the primary iron energy spectrum in the range $10^{16} - 10^{18}$ eV [8].Particles beyond the ankle are thought to be of extragalactic origin because their gyroradius is larger than the size of the galaxy. Furthermore, a sharp cut-off is expected around $\sim 5 \cdot 10^{19}$ eV, the so called GZK cut-off, due to interactions of particles with the cosmic microwave background photons [3]. This effect was predicted by Greisen [9], Zatsepin and Kuz'min [10] in 1966 and so called the GZK cut-off. Measurements performed by the Pierre Auger Observatory point out a strong flux suppression above $4 \cdot 10^{19}$ eV [11].

For energies less than $\sim 10^{9}$ eV the cosmic ray flux undergoes the effect of *solar modulation*. Thus, the attenuation of the power-law spectrum observed at low energies varies with the phase of the solar cycle (see section 1.4).

Another important feature is that the slopes of energy spectra are different for different elements. This is due to the fact that there are *primary* and *secondary* cosmic rays elements. The primary elements, such as carbon and oxygen, are accelerated in large abundances in sources of high energy particles while secondary particles, like lithium, beryllium and boron, are created by nuclear interactions of primary cosmic rays with the nuclei of the interstellar gas. This last process is known as *spallation*. Secondary particles show significantly steeper spectra than those of primary ones [1]. Figure 1.2 shows relative abundances of galactic cosmic rays at the top of the Earth's atmosphere compared with the relative abundances of these elements in the solar system. The relative abundances of elements like carbon and oxygen are similar in both cases, thus demonstrating that these are primary elements. On the other hand, some elements that are rare in the solar system such as lithium, beryllium and boron are more abundant in galactic cosmic rays: this is a proof that these elements are secondary ones produced by spallation process.
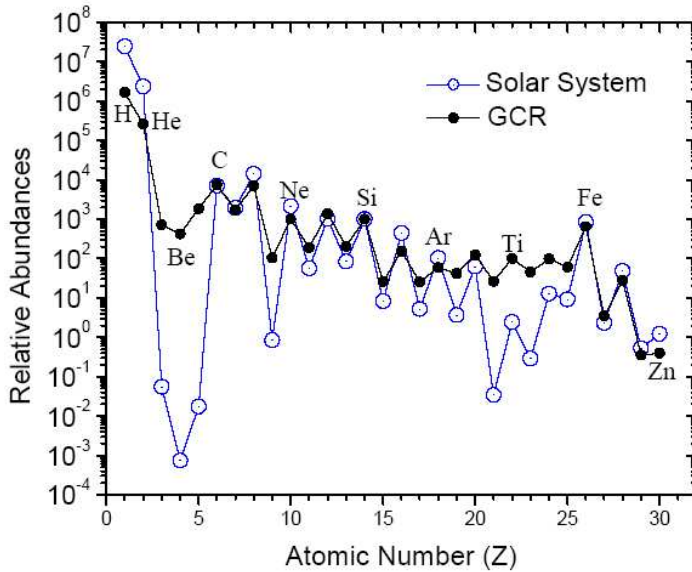
Figure 1.2. Relative abundances of galactic cosmic rays (GCR) at the top of
the Earth's atmosphere (black full circles) compared with the relative abundances of
these elements in the solar system (blue open circles). Abundances of both GCR and
solar system elements are normalized to $Si = 10^3$. Data of cosmic-ray abundances
for elements heavier than helium are taken from the ACE/CRIS experiment [12],
[13].

1.2 Acceleration mechanisms

The mechanism by which charged particles are accelerated to high energies was
first introduced by Fermi in 1949 and is based on the acceleration in strong shock
waves, such as those produced in *supernovae explosions*. This mechanism is based
on the assumption that particles have an isotropic velocity distribution behind the
shock and that they diffuse from behind the shock to the upstream region in front
of the shock itself. The important thing is that particles receive an increase of
energy every time they cross the shock front and this increment in energy is the
same going in both directions (head-on collisions). The average energy gained on
crossing the shock is:

$$\left\langle \frac{\Delta E}{E} \right\rangle = \frac{2}{3} \cdot \frac{V}{c} \tag{1.1}$$

where V is the velocity of the gas behind the shock and c is the velocity of light
[14]. This mechanism is also called *first order Fermi acceleration* due to the fact
that it is first order in V/c. In the *second order acceleration* mechanism the average

energy gained is:

$$\left\langle \frac{\Delta E}{E} \right\rangle = \frac{2}{3} \cdot \left(\frac{V}{c}\right)^2 \tag{1.2}$$

In this case charged particles are reflected by irregularities in the Galactic magnetic field assumed to move randomly with velocity V: since V is very small compared to the velocity of light ($V/c \leq 10^{-4}$) the rate of energy gain by particles is very slow and the *second order acceleration* is not so efficient. Equation 1.1 is a very important result because using this acceleration mechanism a power-law differential energy spectrum of the high energy particles can be obtained [14]:

$$N(E)dE \propto E^{-2}dE. \tag{1.3}$$

There is an upper limit to the energy to which particles can be accelerated by this mechanism. The first order Fermi acceleration is in fact a slow process and particles have to diffuse back and forth across the shock wave in order to gain a lot of energy. Considering for instance the shock wave of a *Supernova remnant*, its acceleration phase last typically about 10^5 years and the upper limit to the energy of particles which can be accelerated in typical supernova explosions is about 10^{14} eV/nucleon. As already mentioned, the cosmic ray spectrum extends well beyond this upper limit and so shock acceleration in supernovae cannot account for the complete range of energies observed [14].

One of the possible candidates for a source of the highest energy cosmic rays is the *pulsar magnetosphere* (figure 1.3). Pulsars with strong magnetic fields and short periods, such as the Crab pulsar, have such strong electric potentials within the magnetospheres that particles can be accelerated to high energies. Using Maxwell's first equation one can evaluate the maximum amount of energy which a particle can attain in a magnetic field of strength B and dimension L:

$$E_{max} = \gamma m c^2 \sim zeBcL \tag{1.4}$$

and considering for instance the magnetic field of a pulsar during its first phases, B $= 10^6$ T and a region of dimension L ~ 100 km, the total energy given to the particle is:

$$E_{max} = 5J = 3 \cdot 10^{19}eV \tag{1.5}$$

Thus, this result shows that particles could be accelerated to the highest energies in the vicinity of pulsars [14]. In the same way charged particles can be confined in other large astrophysical objects, like active galactic nuclei (AGN) or gamma ray bursts (GRB), and can be accelerated through repeated crossing of the plasma shock fronts. The so called Hillas plot is displayed in figure 1.4: the diagram shows the maximum kinetic energy at which particles can be accelerated (black lines) in relation to the size and the magnetic field strength of some celestial objects [15].
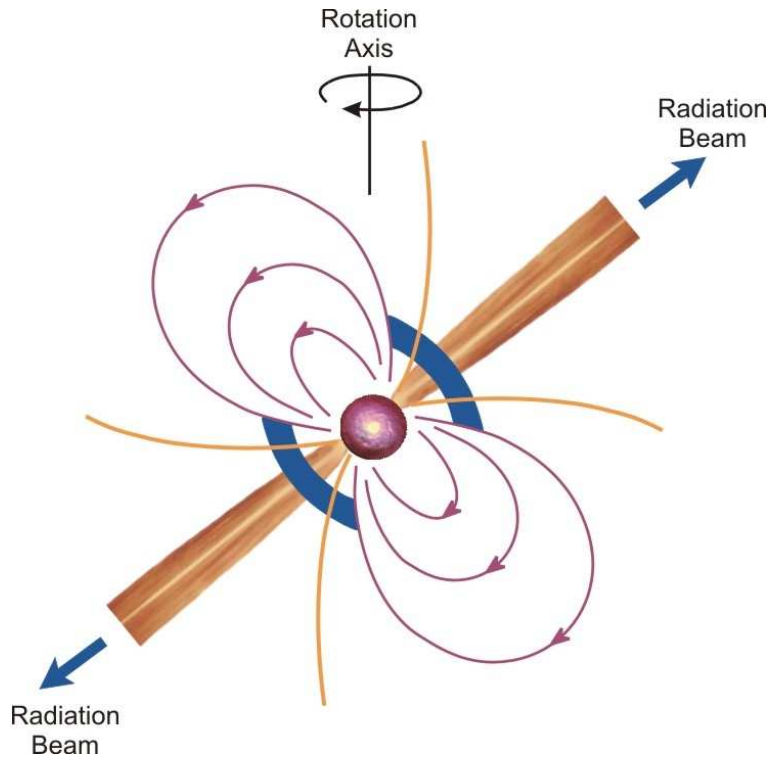
Figure 1.3. A schematic model of a pulsar: the sphere in the middle represents the rotating neutron star in which the magnetic and rotation axes are misaligned, the curves indicate the magnetic field lines and the two cones represent the emission beams. The radio pulses are caused by radio emission from the poles of the magnetic field distribution. Typical parameters for a neutron star are: $M = 1.4\ M_\odot$, $R = 10$ km, $\vec{B} = 10^4 - 10^9$ T.
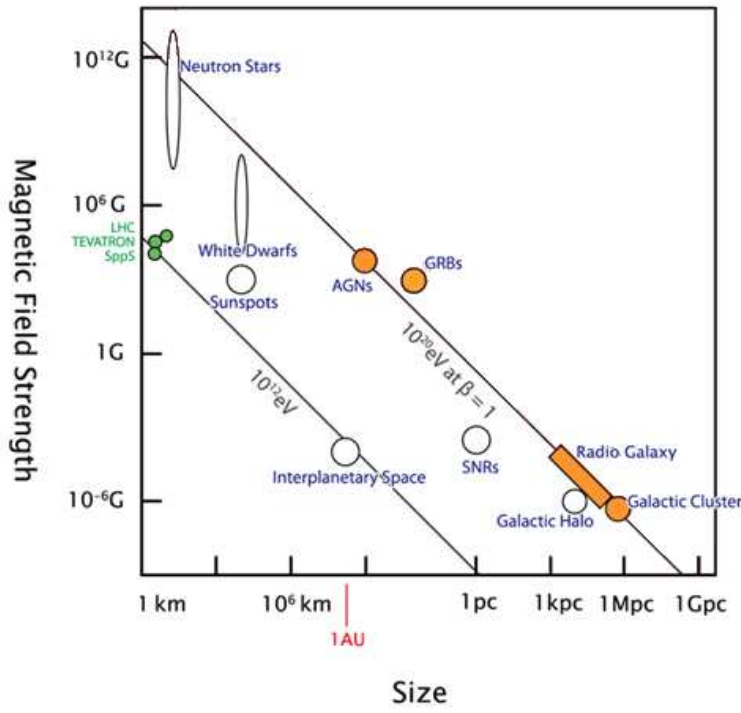
Figure 1.4. Hillas plot: size L and magnetic field strength B diagram for some celestial objects. The minimum product $B \cdot L$ for containing particles with energy 10^{12} eV and 10^{20} eV is also shown (black lines) [15].

1.3   Propagation mechanisms

Once these particles are accelerated to very high energies, as described in the paragraph 1.2, they propagate through the interstellar medium before reaching the Earth. During the propagation phase the particles lose energy interacting with matter, magnetic fields and radiation. The processes which participate in the particles transportation are diffusion, convection and re-acceleration.

1.3.1   Diffusion processes

A way to describe cosmic ray propagation is the *diffusion-loss equation*:

$$\frac{dN(E)}{dt} = \frac{d}{dE}\Big[b(E)N(E)\Big] + Q(E,t) + D \bigtriangledown^2 N(E) \tag{1.6}$$

for high energy electrons and

$$\frac{dN_i(E)}{dt} = \frac{d}{dE}\Big[b(E)N_i(E)\Big] + Q_i(E,t) + D \bigtriangledown^2 N_i(E) - \frac{N_i(E)}{\tau_i} + \sum_{j>i} \frac{P_{ij}}{\tau_j} N_j \tag{1.7}$$

for light nuclei [14].

In both cases, the term $d[b(E)N]/dE$ describes the temporal evolution of the particle energy spectrum in an elementary volume dV subject only to energy gains and losses while the term $Q(E,t)$ is the rate of injection of particles per unit volume. The *diffusion process* which permits particles to enter and leave the volume dV is described by the term $D \bigtriangledown^2 N(E)$: this process depends upon the gradient of particle density $N(E)$ and the scalar diffusion coefficient D. Typical values of the diffusion coefficient are $D \sim (3 - 5) \cdot 10^{28}$ cm^2 s^{-1} at energy ~ 1 GeV/n. This value increases with magnetic rigidity as R$^{0.3}$ - R$^{0.6}$ in different diffusion models of cosmic rays propagation [16]. In the light nuclei case all these quantities are identified by the letter i because they refer to a particular species i. Furthermore, the last two terms describe the effects of spallation gains and losses: τ_i and τ_j are the spallation lifetimes of particles of species i and j and P_{ij} is the probability that the species i is created during an inelastic collision involving the destruction of the nucleus j. As indicated by the sum in the last term, it is the spallation of all species with $j > i$ which gives contributions to the number density of nuclei of species i, N_i [14].

1.3.2   Convection processes

Although the most important propagation process is diffusion, experimental data show that diffusion alone cannot account for the entire propagation process. Cosmic rays can be transported also through the galactic winds existing in many galaxies.

Galactic winds are streams of charged particles, mostly equivalent to solar wind but on galactic scale. They result from different contributions: solar winds of very massive and bright stars, accretion processes of massive stars, Supernovae explosions and accretion processes of supermassive black holes at the centre of galaxies.

Nowadays, two models describing this process have been studied: the one-zone and the two-zone model. In the so called one-zone model convection and diffusion processes are both present through-out the galaxy. In the two-zone model diffusion plays a role alone up to 1 kpc distance from the plane of the galaxy and both diffusion and convection are present beyond [16].

1.3.3 Reacceleration processes

Cosmic ray particles can be accelerated also by magnetohydrodynamic (MHD) waves due to inhomogeneities in the galactic magnetic field. This process is called *reacceleration* to distinguish it from the primary acceleration process. Reacceleration depends on the velocity of disturbances propagating in a magnetic field (Alvén velocity). Data on secondary nuclei abundances can be well explained considering reacceleration processes in the energy range 1-100 GeV/nucleon: the increase of the relative abundance of secondary nuclei, in this part of the spectrum, as the energy increases could be explained by the fact that particles spend longer time in the region due to reacceleration [16]. Furthermore, for energies greater than ~ 100 GeV/nucleon diffusion and/or convection processes starts being predominant thus explaining the decreasing of secondary nuclei abundances as function of energy. For instance, diffusive-reacceleration models described in [17] adapt well to the measured boron-to-carbon ratio, showing also that models predicting reacceleration of cosmic rays produce the characteristic peak observed in the B/C ratio spectra at approximately 1 GeV/nucleon. Theoretical B/C ratio energy spectra are shown in figure 1.5 together with experimental data from AMS-01 and HEAO-3-C2 experiments.

1.4 Solar modulation

When cosmic ray particles enter the solar system they experience the solar wind and their energy spectra are consequently modified. This effect is called *solar modulation* and can have a significant effect on cosmic rays with energies less than ~ 10 GeV [20]. The intensity of the solar activity is periodic with a 11-year cycle. During periods of maximum activity solar flares become more frequent. Solar flares are explosions which occur in the Sun's atmosphere, usually near sunspots: during solar flares charged particles, mostly protons and electrons, are accelerated and the solar wind consequently increases. Furthermore, at each maximum the polarity of the solar magnetic field reverses so that a complete solar cycle is 22 years long.

The flux of low energy particles decreases during periods of high solar activity and reaches the minimum at the solar maximum and vice-versa. This phenomenon
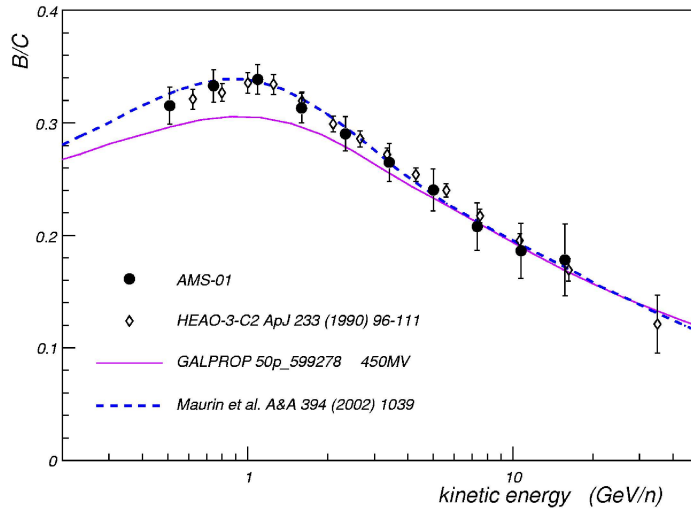
Figure 1.5. B/C ratio energy spectrum as measured by AMS-01 (filled black points) [18]; measurements from HEAO-3-C2 experiment are shown too (open diamonds). Experimental data are compared to two propagation models of cosmic rays in the galaxy: a *diffusive-reacceleration* model (violet line) [17] and a *diffusion/convection/reacceleration* model (blue dashed line) [19].

is due to the fact that the greater the solar activity, the greater the disturbances in the interplanetary magnetic field which impedes the propagation of particles, mainly of low energy, to the Earth. The sinusoidal time dependence of the solar activity and of the cosmic rays flux is clearly visible on figure 1.6: cosmic rays data are derived from neutron monitor detector located at different points on the globe (Neutron Monitor Network [21]). Neutrons are produced by interactions of primary cosmic rays with nuclei constituting the atmosphere, mainly nitrogen and oxygen, and thus the flux detected on the ground is directly proportional to the flux of galactic cosmic rays arriving at the top of the atmosphere. Figure 1.6 shows clearly the anticorrelation between cosmic ray flux and solar activity: during periods of maximum solar activity the flux of cosmic ray particles on the Earth is attenuated.
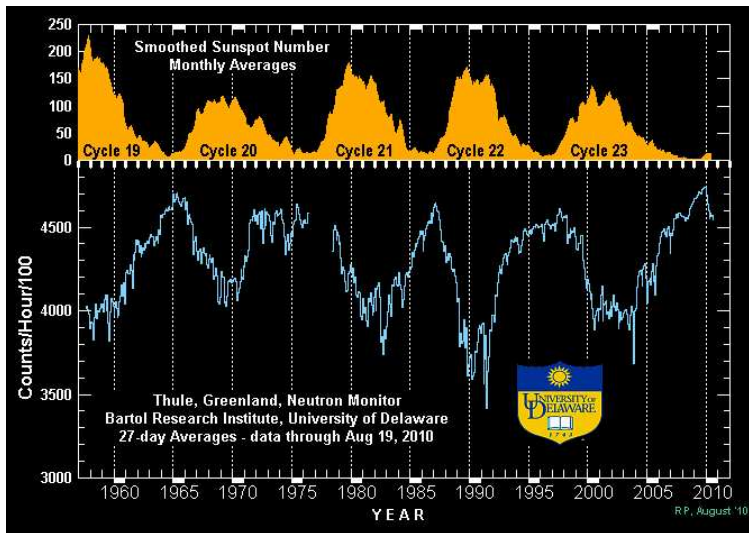

Figure 1.6. The sinusoidal time dependence of the solar activity (yellow line) compared to the count rate recorded by a neutron monitor detector in Thule, Greenland (blue line) [22].

Furthermore, the reversal of the solar polarity causes a reversal in the magnetic field profile too. Positive and negative particles drift in different directions in the heliospheric magnetic field causing a charge sign dependence. Due to this effect positive particles are favoured during an A > 0 solar magnetic field phase and are instead suppressed during an A < 0 phase [23]; this configuration is shown in figure 1.7. The most recent reversal of the solar magnetic field from an A > 0 to an A < 0 configuration took place during year 2000.
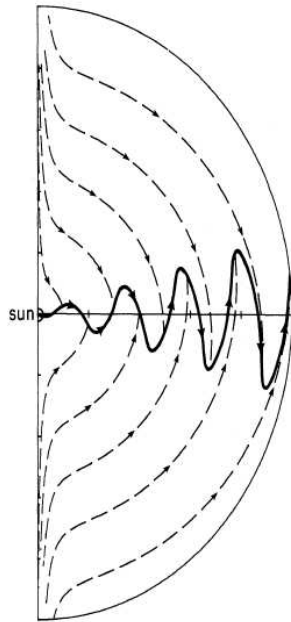
Figure 1.7. Drift trajectories for 2 GeV protons in an A > 0 solar magnetic field configuration. The tick marks are at 5 AU intervals. The direction of the arrows changes for an A < 0 phase or for negative charged particles [23].

1.5   Cosmic ray positrons

As already mentioned at the beginning of this chapter, electrons account for ~ 2 % of the cosmic ray particles. The proton-to-positron flux ratio is $\sim 10^3$ at 1 GV and increases to $\sim 10^4$ at 100 GV [20]. Even if electrons and positrons are very few compared to protons, they are of very high interest nowadays because of the astrophysical questions they could answer. Since they loose energy very efficiently as they propagate they could give useful information about acceleration mechanisms and propagation processes of cosmic rays in our Galaxy.

Positrons are believed to be mainly secondary particles, produced during interactions of primary cosmic ray nuclei with the interstellar medium. When primary cosmic ray protons interact with protons of the interstellar gas, charged pions and kaons are produced; thus secondary positrons are decay products of π^+ and K^+. The so called *positron fraction*, i.e. $\Phi(e^+)$ / $[\Phi(e^+) + \Phi(e^-)]$, obtained from models considering a pure secondary positron production and with or without reacceleration processes are shown by Moskalenko & Strong [24] (see figure 1.8). According to these models the positron fraction is expected to decrease as the energy increases and this trend is consistent with experimental data up to 10 GeV. For energies
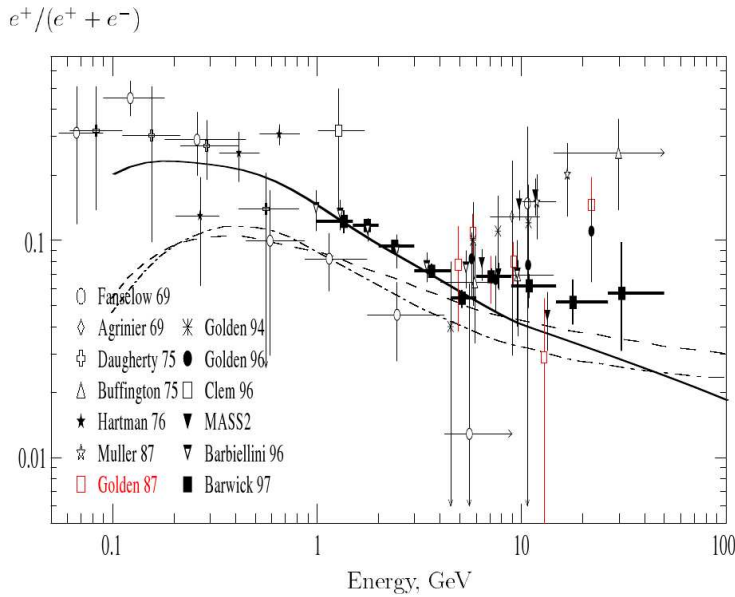
$e^+/(e^+ + e^-)$

Figure 1.8. Positron fraction for a pure secondary positron production and without reacceleration processes as evaluated by Moskalenko & Strong [24] (black solid line). Predictions for the positron fraction considering a leaky-box model (dashed-dot line) and a diffusion model (dashed line) [25] are also shown. The experimental data are taken from [26].

greater than 10 GeV data collected during the 90's possibly show an excess with weak statistical significance above the predicted ratio, although the observational errors are large and there are not so many measurements at higher energies [24].

Positrons could be also created as primary particles in high-energy particles astrophysical sources, such as in the magnetosphere of near-by pulsars and Supernova Remnants, or be produced by dark matter particle annihilations. Electrons can be accelerated in the magnetosphere of pulsars, magnetized neutron stars with high spin periods. In pulsar magnetic fields, about $10^6 - 10^9$ T [14], electrons lose energy via synchrotron radiation and consequently photons are produced; these photons can then produce pairs of electrons and positrons with lower energies. These particle pairs are then accelerated and confined in the pulsar nebula for $\sim 10^5$ years before escaping into the interstellar medium. The energy spectrum of these primary positrons is expected to be harder than that of the secondary ones with spectral index of about 1.5 - 1.6 according to Zhang & Cheng [27]. Thus, positrons originated from pulsars may dominate the high energy end of the cosmic rays positron spectrum. Only pulsars at a distance of 1 kpc or closer can contribute significantly to the positron energy spectrum due to the energy losses during the propagation into the interstellar medium [28]. For instance, it has been estimated by Hooper

et al. [29] that at 10 GeV only $\sim$ 20 % of the cosmic rays positrons originate from pulsars within 500 pc from the Solar System; furthermore, above $\sim$ 50 GeV the positron spectrum seems to be dominated by a single or small number of nearby pulsars.

Beside astrophysical sources, primary positrons could be produced also via annihilation of dark matter particles. Nowadays it is known that baryonic matter accounts only for 4 % of the total energy density of the Universe; the remaining is shared among dark matter ($\sim$ 23 %) and dark energy ($\sim$ 73 %). WIMPs are one of the favourite candidates for the dark matter component of the Universe. They are expected to form a halo around the disk and the bulge of our Galaxy. Few examples of WIMP particles are the *neutralino*, Majorana fermion in the supersymmetric scenario of the particle standard model, the lightest *Kaluza-Klein* particle in the Universal Extra Dimension model. In this last scenario, primary positrons could be produced via annihilation of some Kaluza-Klein dark matter particles, for instance through the process $\chi\chi \rightarrow e^+ \, e^-$.

1.5.1   PAMELA positron fraction

The PAMELA detector has been collecting data since July 2006. The first results obtained by the Collaboration concern the antiproton-to-proton flux ratio between 1 and 100 GeV and the positron fraction between 1.5 and 100 GeV. Those results are based on the data collected between July 2006 and February 2008: more than 10^9 triggers have been acquired during a total acquisition time of $\sim$ 500 days [30].

In figure 1.9-*top* the positron fraction is shown together with a theoretical trend for pure secondary positron production during the propagation of cosmic rays in the galaxy [20]. Comparing PAMELA data with those obtained from other experiments (figure 1.9-*bottom*) two disagreements are evident at lower and higher energies.

The difference at low energy is interpreted as a consequence of solar modulation effects. As explained in section 1.4 the solar wind affects the energy spectra of cosmic rays within the solar system. The most recent reversal of the solar magnetic field took place during year 2000 and it is clearly visible in the antiproton-to-proton flux ratio as measured by several flights of the BESS balloon-borne experiment between 1997 and 2000 [31]. CAPRICE94, HEAT95 and AMS-01 data (figure 1.9-*bottom*) have been collected during the previous solar cycle which favoured positively charged particles, explaining in this way the higher positron fraction at lower energies comparing to the PAMELA one. Furthermore, data collected during June 2006 by the AESOP balloon-borne experiment [32] show also a lower positron fraction at low energies compared to data collected before year 2000 (figure 1.9-*bottom*) in agreement with PAMELA data. Thus, the low energy PAMELA data show the most statistically significant charge-sign dependence for solar modulation to date [20].

At high energies, above 10 GeV, the PAMELA positron fraction increases clearly with energy. The theoretical calculations done considering a pure secondary production of positrons during the propagation of cosmic rays in the galaxy [24] is not able to fully describe PAMELA data. A study about uncertainties on this model

have been carried on by Delahaye et. al. [33]. This study concerns uncertainties on nuclear cross-section, effect induced by primary electron injection spectra and models of propagations throughout the galaxy. Considering these uncertainties and a soft electron spectrum, it seems that PAMELA data could be explained by the standard secondary production. However, PAMELA measurements of the electron spectrum indicate a hard spectral index [34]. On the other hand, changing the injection spectral index of primary electrons, i.e. for a harder electron spectrum, PAMELA data show an excess above ~ 10 GeV [33]. This means that either a significant modification in the acceleration and propagation models for cosmic rays is needed or a primary component is present. Even if the reason for this rise is still unclear, many models have been proposed in order to explain PAMELA data. These models concern astrophysical sources, mostly pulsars, or the annihilation of dark matter particles.

As already mentioned, pulsar magnetospheres could be sources of primary cosmic ray positrons. Some studies performed by Hooper et al. [29] show that PAMELA positron fraction can be well reproduced considering positrons produced by the sum of all pulsars in our Galaxy (figure 1.10); in particular, the best fit is obtained for about one pulsar birth each ~ 25 years.

Many different interpretations of PAMELA data regard production of positrons by annihilation of dark matter particles. Already in 1991 Kamionkowski and Turner postulated a rise in the positron fraction due to the annihilation of WIMPs particle in the galactic halo [35]. Nowadays, the *neutralino* seems to be the most favoured dark matter particle candidate even if it is difficult to interpret PAMELA data in a scenario where neutralino is the dominant dark matter component. In fact, the antiproton flux spectrum published by PAMELA collaboration [30] is in agreement with a pure secondary production. Neutralino suffer the helicity suppression in the annihilation process thus resulting in a softer positron spectrum than the one observed by PAMELA. To overcome this problem, many theories have been proposed. One of them requires neutralino annihilation into leptons (mainly $\chi\chi \rightarrow e^+ e^- \gamma$) and radiative corrections for propagation effects: this results in a harder positron spectrum (figure 1.11) with a negligible impact on the antiproton spectrum [36]. Other models consider *Kaluza-Klein* particles: for instance, a lightest Kaluza-Klein particle is a boson that can annihilate directly into positron-electron pairs without helicity suppression [37].
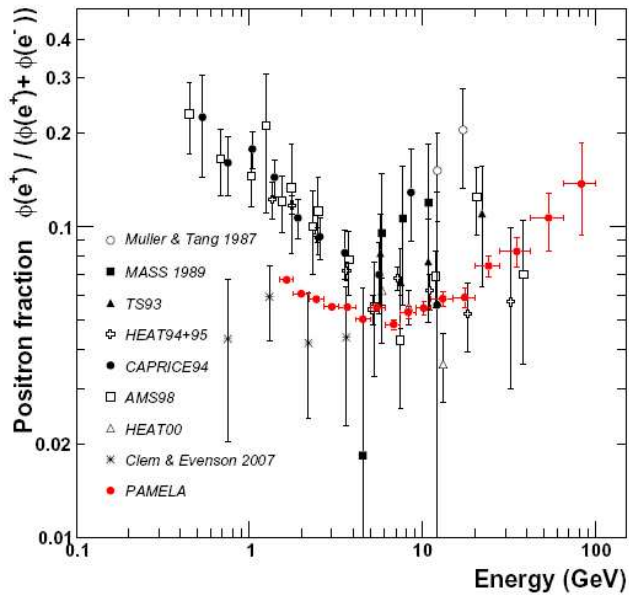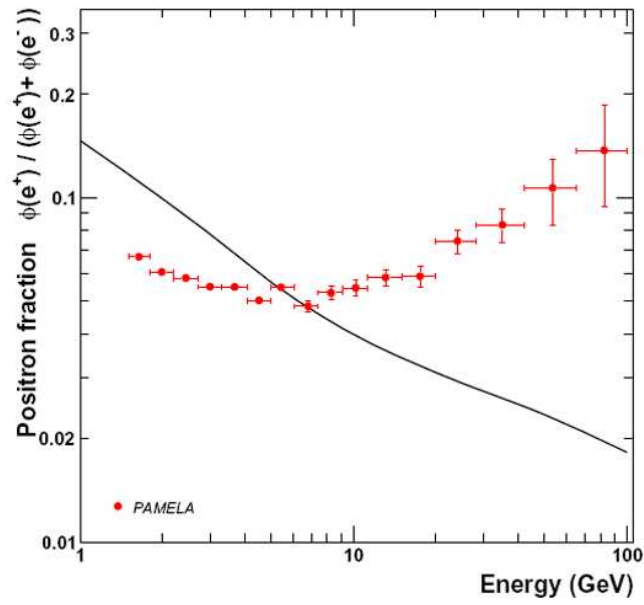
Figure 1.9. *Top*: the positron fraction as measured by the PAMELA experiment; the error bars corresponds to one standard deviation. The solid line represents the theoretical fraction for pure secondary positron production considering diffusion and convection as propagation mechanisms without reacceleration processes [20], [24]. *Bottom*: comparison between the PAMELA positron fraction (red points) and other recent experimental data [20].
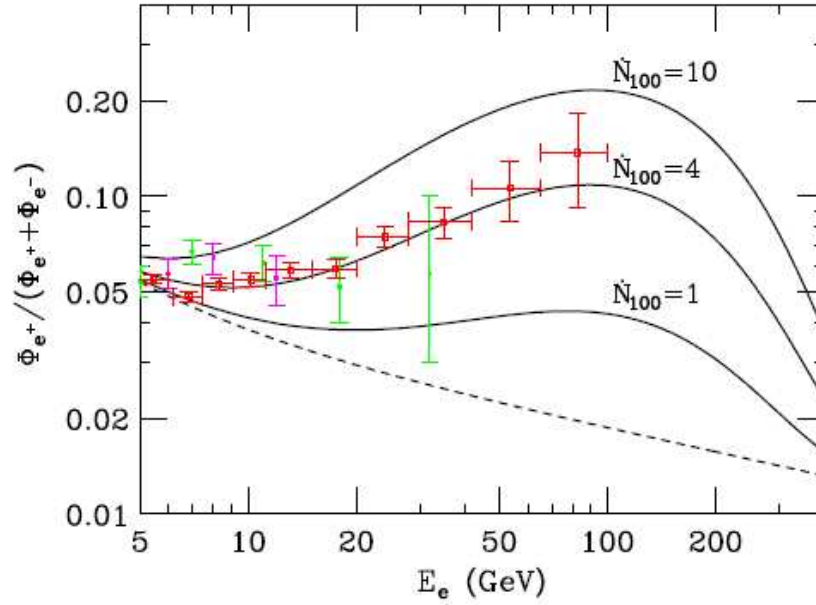
Figure 1.10. Positron fraction measured by the PAMELA experiment (red points) compared to theoretical positron fraction (black lines) resulting from the sum of all pulsars in our Galaxy within 500 pc of the Solar System. Calculations have been done considering different rates of pulsar birth: one per 10 years ($\dot{N}_{100} = 10$), one per 25 years ($\dot{N}_{100} = 4$) and one per 100 years ($\dot{N}_{100} = 1$). $\dot{N}_{100}$ is the rate of pulsar formation in units of pulsars per century [29]. The theoretical prediction considering a pure positron secondary production is also shown (dashed line) [24]. Pamela results are compared to data obtained by the HEAT experiment (green points) [26].
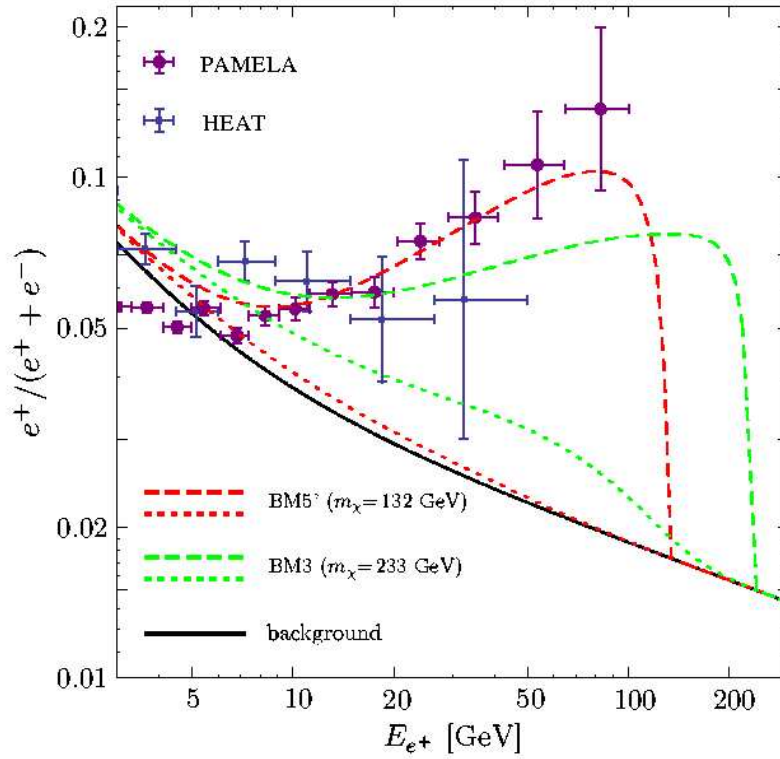
Figure 1.11. Positron fraction measured by the PAMELA experiment (violet points) compared to theoretical positron fraction considering dark matter particle annihilation models (green and red lines). The models taking into account different neutralino masses with radiative corrections (dashed lines) or without radiative corrections (dotted lines) [36]. The theoretical prediction considering a pure positron secondary production is also shown (black solid line) [24]. Pamela results are compared to data obtained by the HEAT experiment (blue points) [26].

Chapter 2

The PAMELA experiment

PAMELA (**P**ayload for **A**ntimatter **M**atter **E**xploration and **L**ight-nuclei **A**strophysics) is a satellite-borne experiment mounted on board of the Russian Resurs DK1 satellite. It was launched from the Baikonur cosmodrome in Kazakhstan on June 15th 2006. The satellite acquires high-quality images of the Earth's surface. Its mass is ~ 6.7 tonnes and its height is 7.4 m. The satellite orbit is elliptical and semi-polar and its altitude varies between 350 km and 600 km with an inclination of 70°. An overview of the Resurs DK1 satellite is shown in figure 2.1.

The PAMELA experiment is mounted in a pressurized container attached to the Resurs DK1 satellite (figure 2.1). It has been designed to study charged cosmic rays particles and mainly antiparticles, *antiprotons* and *positrons*.

In this chapter a detailed description of the PAMELA experiment is presented together with a summary of the main scientific goals.

2.1   The PAMELA apparatus

The PAMELA apparatus has an height of ~ 1.3 m, a mass of 470 kg and an average power consumption of 355 W. It is formed by the following subdetectors:

- a time-of-flight system (ToF)

- a magnetic spectrometer (Tracker)

- an electromagnetic calorimeter

- a neutron detector

- an anticoincidence system (AC)

The geometrical acceptance of the experiment is 21.5 cm^2 sr and is determined by the geometry of the magnetic spectrometer cavity [38].
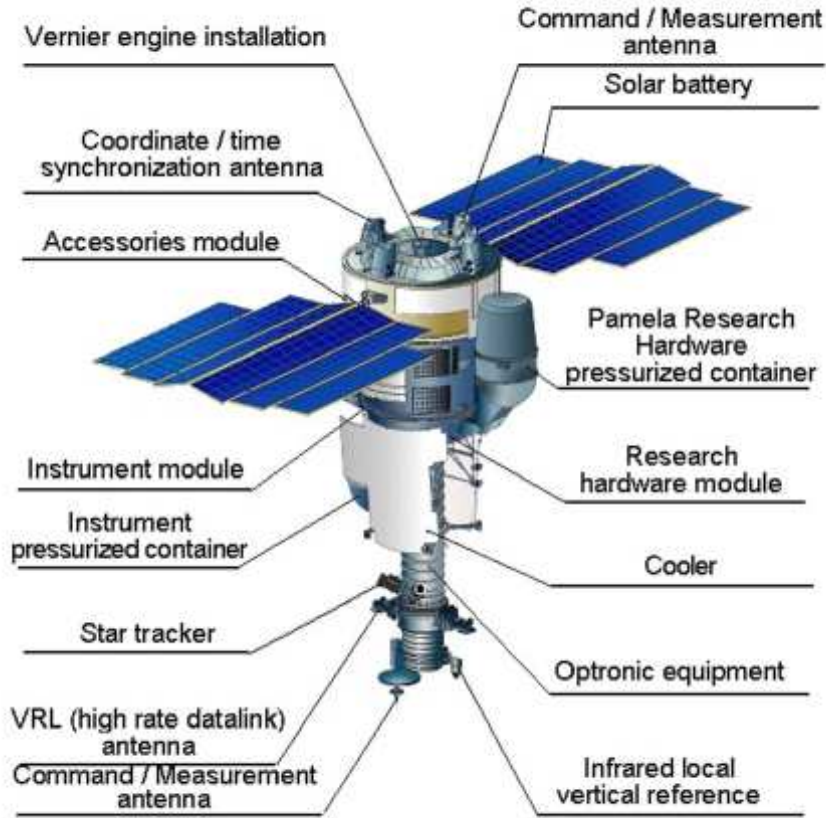
Figure 2.1. A schematic overview of the Resurs DK1 satellite which hosts the PAMELA experiment. The satellite has a mass of ~ 6.7 tonnes and a height of 7.4 m; the solar array span is ~ 14 m [38].
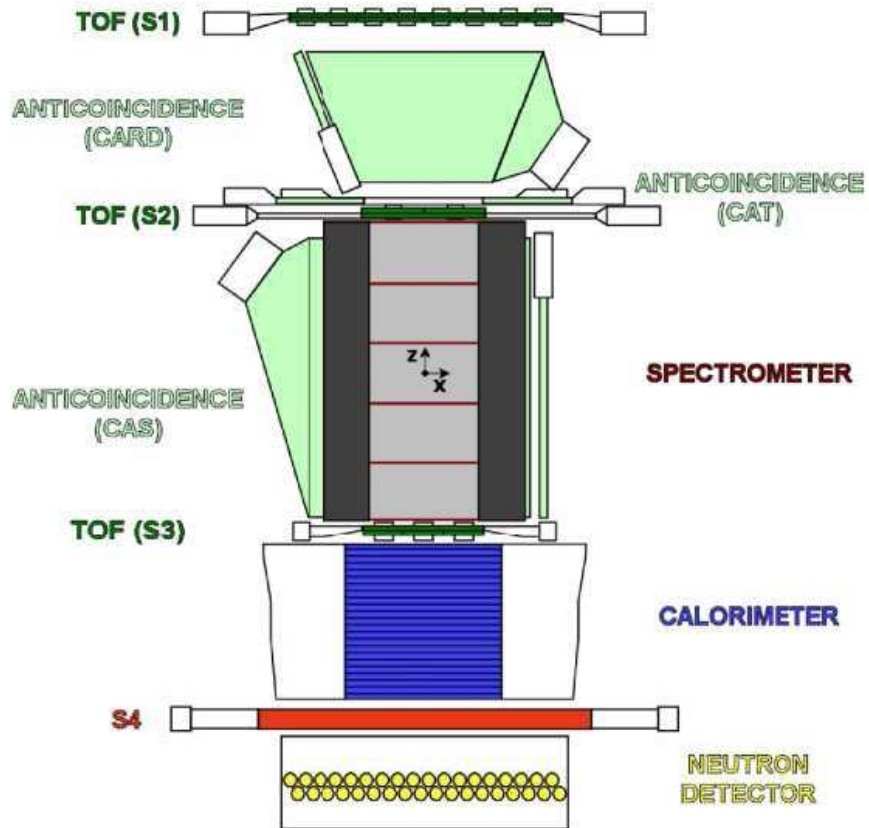
Figure 2.2. Schematic overview of the PAMELA detector. The instrument has an height of ∼ 1.3 m, a mass of 470 kg and an average power consumption of 355 W [38].
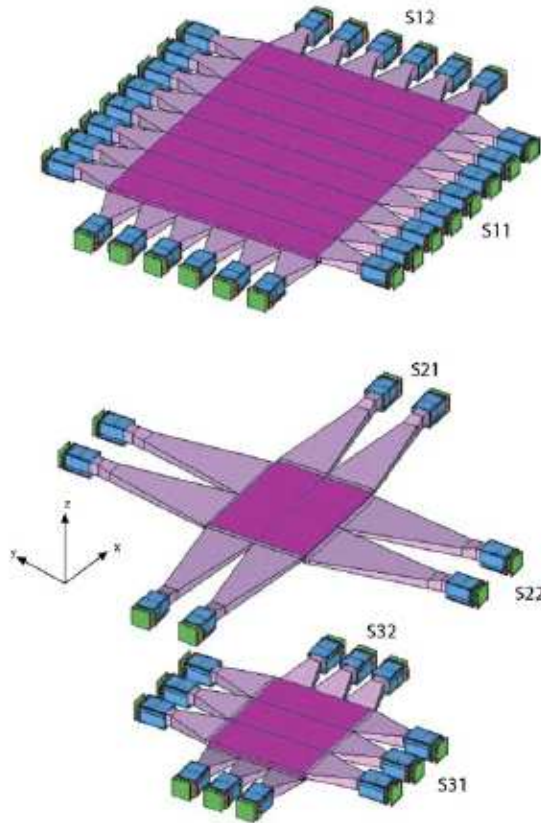
2.1.1   The time-of-flight system

Figure 2.3. Scheme of the time-of-flight system. The distance between the scintillator planes S1 and S3 is 77.3 cm. S1 has a sensitive area of (33×40.8) cm^2. Both S2 and S3 have a sensitive area of (15×18) cm^2 [38].

The *time-of-flight system* (ToF) consists of three planes labeled as S1, S2 and S3 and arranged as shown in figure 2.2. The plane S1 is situated on the top of the apparatus, S2 lies above the magnetic spectrometer while S3 lies between the spectrometer and the calorimeter; the distance between S1 and S3 is 77.3 cm. Each plane is formed by two fast plastic scintillators layers (Bicron BC-404) placed orthogonal to each other (figure 2.3). The two S1 layers, so-called S11 and S12, are divided into 8 and 6 bars respectively with a thickness of 7 mm and a total sensitive area of (33×40.8) cm^2. The S2 layers, S21 and S22, are segmented into 2×2 orthogonal bars with a thickness of 5 mm while S3 layers, S31 and S32, are segmented into 3×3 orthogonal bars. Both the planes S2 and S3 have a sensitive

area of (15×18) cm^2. Each of the ToF scintillator bars are glued at the ends to a plastic light guide which is read out by a photomultiplier (Hamamatsu R5900U).

The ToF system acts as the main PAMELA trigger by measuring the coincidental energy deposits in the scintillators. The measurement of the ionisation energy loss (dE/dx) in the scintillator planes determines the absolute value of charge, z, of the incident particles. Furthermore, the ToF measures the flight time of the particles passing through its planes: this information is combined with the track length derived from the spectrometer in order to derive the velocity β of incident particles. This also permits up-going particles, so-called albedo particles, to be rejected, excluding in this way misidentification between a particle and an antiparticle due to the bending of the spectrometer magnetic field. The flight time for a 1 GeV/c electron is 2.7 ns and for 1 GeV/c proton is 3.7 ns. Thus, since the time resolution is about 250 ps, the ToF allows to discriminate between electrons and antiprotons, or protons and positrons, up to $\sim$ 1 GeV/c [38], [39].

An extra scintillator plane, S4, is situated just under the calorimeter. It consists of a single scintillator plane of 1 cm thickness and an area of (48×48) cm^2 and it is read out by six photomultipliers. The main task of this scintillator plane is to detect showers which are not fully contained in the calorimeter improving in this way the electron-hadron separation performance of the all instrument.

2.1.2 The magnetic spectrometer

The magnetic spectrometer, or tracker, consists of a permanent magnet and six silicon detector planes (figure 2.4). The magnet has a tower which is 44.5 cm high and composed of five identical modules. Each module comprises twelve magnetic blocks made of a Nd-Fe-B alloy with a residual magnetisation of 1.3 T. These five modules form a rectangular cavity (13.1×16.1) cm^2 which defines the geometrical factor of the PAMELA experiment to be 21.5 cm^2 sr. The modules are also configured to provide an almost uniform magnetic field oriented along the y-direction with a mean value of 0.43 T inside the cavity and a value of 0.48 T at the centre. Furthermore, the magnet is enclosed by ferromagnetic shielding in order to attenuate the stray field outside of the cavity which could interfere with the satellite instruments.

Six 300 μm thick silicon detector planes are inserted inside the magnetic cavity separated by 8.9 cm. Each plane is formed by three ladders inserted into an aluminium frame which connects to the magnetic cavity. One ladder comprises two double sided sensors, (5.33×7.00) cm^2, with implanted strips orthogonal to each other on the two sides. This provides two independent impact coordinates on each plane. Also, no additional supporting structure is present above or below the planes in order to limit multiple scattering in dead layers [40].

The magnetic spectrometer allows charged particle deflection η to be measured as well as the rigidity R which is defined as $\eta = 1/R$. The momentum of a particle and the sign of its electric charge are then evaluated via the relation $R = c \cdot p \ / \ Z \cdot e,$
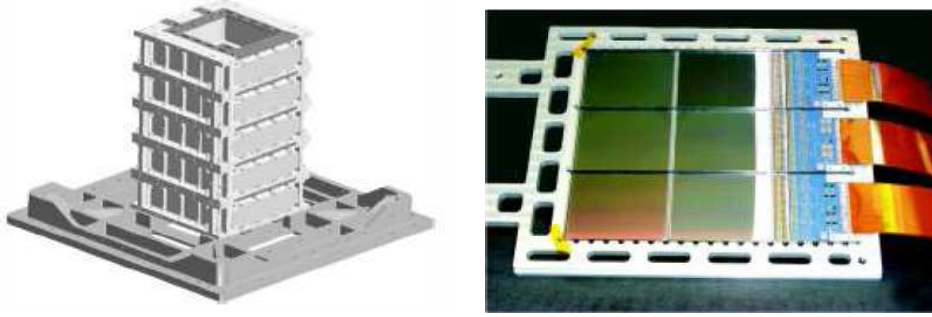
Figure 2.4. *Left*: design of the five modules which constituted the PAMELA
magnet.   The tower is 44.5 cm high and the rectangular cavity is (13.1×16.1)
cm^2 [40]. *Right*: picture of a silicon plane (300 μm thick) inserted in the magnetic
spectrometer cavity: the three silicon strip detectors and the front-end electronics
are clearly visible; each silicon detector has a surface of (5.33×7.00) cm^2 [41].

where e is the electron charge, p is the momentum, c is the speed of light and Z is
the absolute charge.

The resolution of the deflection measurement depends on several factors: the
geometry of the spectrometer, the intensity of the magnetic field and the spatial
resolution of the detector silicon sensors. Tests performed with particle beams show
a spatial resolution of (3.0 ± 0.1) μm in the bending x-view, (figure 2.5, left) and
(11.5 ± 0.6) μm in the non-bending y-view obtained for normally incident tracks.
The resulting deflection measurement error as a function of the rigidity obtained
with proton beams is shown in figure 2.5 (right): this determines the *maximum
detectable rigidity*, MDR, to be ~ 1 TV. The MDR is defined as 100 % uncertainty
in the particle rigidity measurement [42].

2.1.3   The electromagnetic calorimeter

The electromagnetic calorimeter is formed by 44 single-sided silicon sensor planes
interleaved with 22 plates of tungsten absorber. Each silicon plane is 380 μm thick
while each tungsten layer has a thickness of 0.26 cm which corresponds to 0.74 X_0,
radiation lengths. Thus, the total depth of the calorimeter is 16.3 X_0, correspond-
ing to ~ 0.6 nuclear interaction lengths. Each silicon detector has a sensitive area
of (8×8) cm^2 and is segmented into 32 read-out strips with a pitch of 2.4 mm. The
silicon detectors are then arranged in a 3×3 matrix thus forming a total sensitive
area of about (24×24) cm^2. Also, all the silicon strips are connected creating 24
cm long strips.
The strips of two consecutive layers are orthogonal (x-view and y-view) and there-
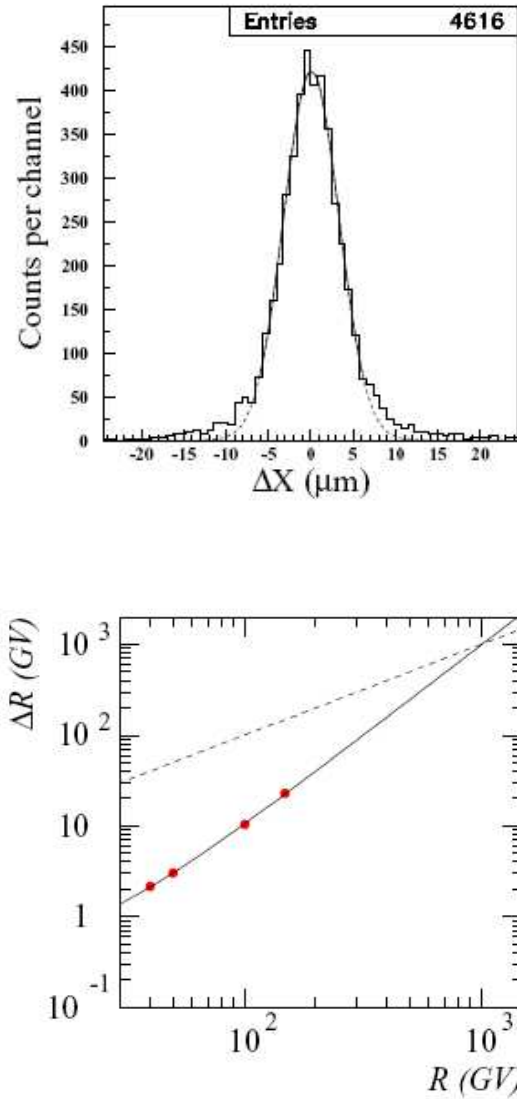fore provide two-dimensional spatial information. The signals are read out using

Figure 2.5. *Left*: the tracker spatial resolution in the bending x-view fitted by a Gaussian distribution. *Right*: the deflection error ΔR measured by the magnetic spectrometer as a function of R obtained with proton beams. The dashed line is the bisector $\Delta R = R$; the fitted function (solid line) depends on the multiple scattering and on the spatial resolution which both contribute to the deflection uncertainty. The intersection of the two curves gives the maximum detectable rigidity of the spectrometer, MDR ~ 1 TV [38].

six CR1.4P chips per plane with the outputs multiplexed into a single 16-bit ADC; also, the read-out is divided into four independent sections, corresponding to the x-even, y-even, x-odd and y-odd planes [43]. Figure 2.6 shows a picture of one single detection module and the whole detector.

The main aim of the calorimeter is to identify positron and antiproton events over large backgrounds of protons and electrons respectively. Since electromagnetic and hadronic showers differ in their longitudinal and transversal profile and energy distributions, a powerful way to distinguish these two events is to analyse the shower development inside the calorimeter. The PAMELA electromagnetic calorimeter was designed in order to reach this goal: its longitudinal (Z) and transverse segmentation (X and Y) described above, combined with the measurement of the particle energy loss in each silicon strip, allows reliable identification of electromagnetic and hadronic showers. The electron-hadron separation performance has been studied and it has been found that it provides a proton rejection factor of $\sim 10^5$ keeping 90 % efficiency in selecting electrons and positrons; an electron rejection factor of $\sim 10^5$ in antiprotons selections has been found too [38].
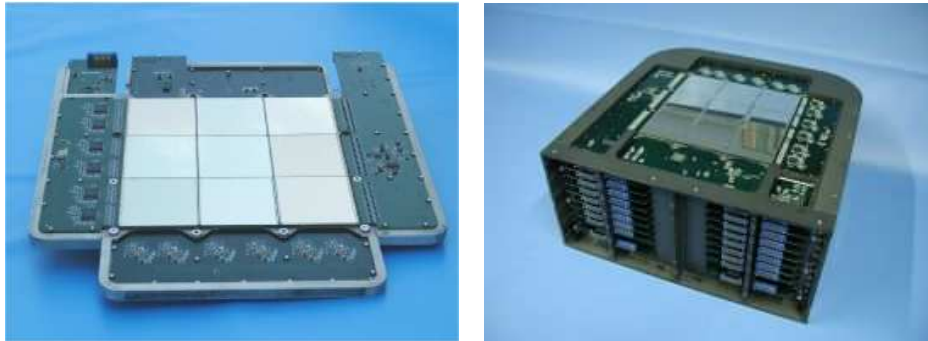

Figure 2.6. *Left*: picture of one *detection module* described in the text; the 3×3 matrix of silicon strips with a size of (24×24) cm^2 is clearly visible. *Right*: picture of the entire electromagnetic calorimeter [41].

2.1.4   The neutron detector

The neutron detector is situated below the S4 scintillator plane. It consists of 36 counters filled with ^{3}He and organized into two planes of 18 counters each. It is also enveloped by a polyethylene moderator in order to prevent thermal neutrons entering from the sides and from the bottom of the detector. The total size of the neutron detector is $(60 \times 55 \times 15)$ cm^3.

2.1.5   The anticoincidence system

The anticoincidence system consists of

- four plastic scintillators surrounding the sides of the magnetic spectrometer (CAS);

- one plastic scintillator covering the top of the spectrometer (CAT);

- four plastic scintillators surrounding the volume between the first two time-of-flight planes, S1 and S2 (CARD).

The CARD detectors geometry is the same of the CAS ones but with a reduced surface area. The CAT detector has a hole in the center corresponding to the spectrometer acceptance (figure 2.7). The anticoincidence plastic scintillators (Bicron BC-448M) are 8 mm thick and are read out by photomultipliers (Hamamatsu R5900U). Two photomultipliers are used for the CAS and CARD detectors in order to decrease the possibility of single point failure; for the same reason and due to its irregular shape the CAT detector is read out by eight photomultipliers.

The anticoincidence system is used to identify *false trigger events*. Simulations have shown that about 75 % of the triggers in orbit are generated by secondary particles produced via interactions of the primary ones with the PAMELA structures: for instance, events interacting into the calorimeter and backscattered or particles entering the apparatus from the side. These events are called false trigger events and they have to be removed during the offline data analysis.

2.2   The PAMELA data acquisition system

A schematic view of the on-board Data Acquisition System (DAQ) is shown in figure 2.8. The Intermediate Data Acquisition System (IDAQ) reads out information from the subdetectors at a rate of 2 Mbytes/s, every time a trigger event is detected. Data are then stored in the PAMELA mass memory before being transferred to the satellite on-board memory several times per day. The downlinking to the Russian ground station in Moscow (NTsOMZ) takes place 2-3 times per day with a total transmission rate of $\sim$ 16 Gbytes/day. The data are pre-processed in Moscow and then transferred via the GRID network from Moscow to the INFN facility at CNAF, Bologna (Italy).

The data acquisition and storage and all the communications with the satellite are control by the Pamela Storage and Control Unit (PSCU). The PSCU is constituted by four parts: two mass memory modules of 2 Gbytes, a CPU, the Pamela Interface Board (PIF) and the Telemetry and Control system (TMTC). The PIF performs communications with the IDAQ system and provides an interface to the mass memories and with the Very high-speed Radio Link (VRL) module of the satellite. The TMTC provides the housekeeping operations, like alarm, temperature and voltage monitoring. The PSCU organizes the data acquisition period in different runs, where each run corresponds to a continous data taking in which the trigger and the detectors configurations are constant.
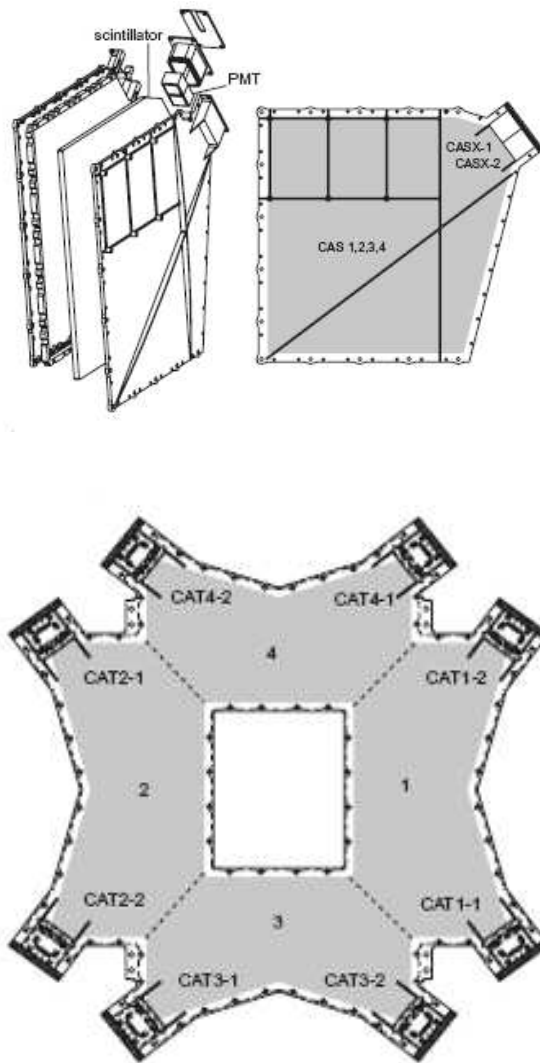
Figure 2.7. The anticoincidence system. *Left*: scheme of the CAS detector which surrounds the sides of the tracker. *Right*: scheme of the CAT detector which covers the top of the tracker; the hole in the centre corresponds to the tracker acceptance and measures (18×22) cm^2. The geometry of the CARD detector is the same of the CAS one but with a reduced surface area [38].
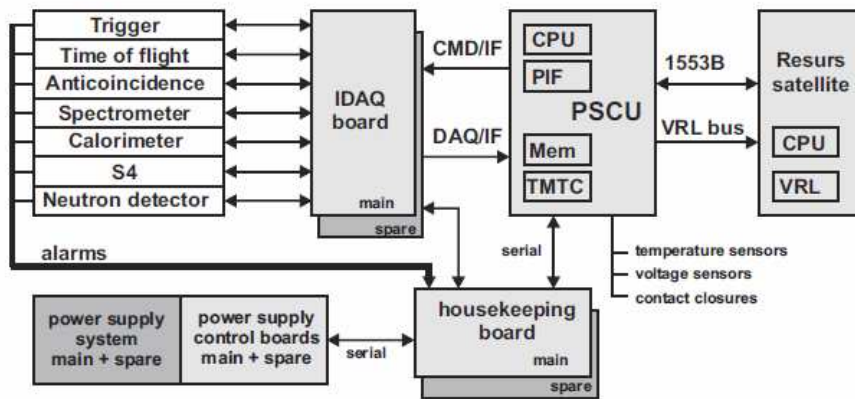
Figure 2.8. Scheme of the PAMELA Data Acquisition System (DAQ) [38].

2.2.1 The trigger configuration

The main PAMELA trigger is set by the time-of-flight system when coincidental energy deposits are detected in its scintillator layers. There are two default configurations:

- (S11 or S12) and (S21 or S22) and (S31 or S32) ⇒ *outside* the radiation belts and the South Atlantic Anomaly (SAA) regions;

- (S21 or S22) and (S31 or S32) ⇒ *inside* the radiation belts and the SAA regions.

Inside the radiation environments the first ToF layer S1 is not considered because of the high counting rate that can saturate it. S2 and S3 can still be used as main trigger in these regions because they are more shielded. Other trigger configurations can be implemented and changed from ground. In figure 2.9 trigger rates observed during two consecutive orbits are shown: the maximum number of events per minute is detected in the polar regions ($\sim$ 35 Hz) while the minimum is detected around the Equator ($\sim$ 15 Hz). When the satellite passes through the SAA region the trigger rate increases up to $\sim$ 70 Hz. The missing acquisition time after the SAA peak corresponds to the calibration time of the detectors. The calibrations of the anticounter, the tracker, the calorimeter and the S4 scintillator are performed by the PSCU when the satellite crosses the equator and it lasts about 1 minute [38]. Furthermore, the calorimeter is equipped with a self-trigger system which allows high energy electrons, between 300 GeV and $\sim$ 1 TeV, to be detected. In order to collect sufficient statistics for these rare events it is necessary to have a large geometrical factor. Thus, the PAMELA geometrical factor is increased to $\sim$ 600

cm^2 sr by requiring that particles enter only from one of the first four planes and cross at least 10 radiation lengths in the calorimeter [43].
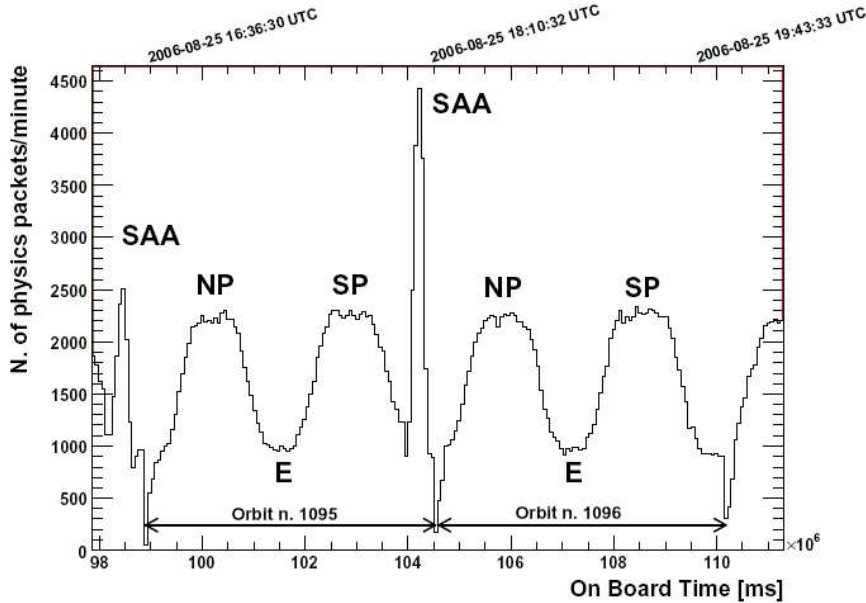

Figure 2.9. The PAMELA trigger rate during two consecutive orbits. The trigger rate is strongly dependent on the position of the satellite: the minimum is reached at the Equator (E) while the maximum at the North Pole (NP) or South Pole (SP); the highest peak corresponds to the South Atlantic Anomaly region (SAA). The missing acquisition time after the peaks of the SAA is due to the detector calibrations passing through the equator [38].

2.3   PAMELA scientific goals

The PAMELA detector has been designed and optimised for the study of the antimatter component in the cosmic radiation. Compared to previous satellites or balloon-borne experiments, the PAMELA apparatus has increased significantly the statistics over a wider energy range in detecting cosmic rays particles and, mainly, antiparticles. The importance of antiparticle studies is linked to the production and propagation mechanisms of cosmic rays in the galaxy. Positrons and antiprotons are believed to be mainly created as secondary products in the interactions between cosmic ray nuclei and atoms in the interstellar medium [24]. High energy antiparticles could also be produced during annihilation or decay processes of dark matter particles, or be produced by nearby sources such as pulsars, for the

positrons case. In table 2.1 the PAMELA design performances in detecting cosmic ray particles and antiparticles are shown. The identification between particles and antiparticles is performed by combining information coming from the magnetic spectrometer and the electromagnetic calorimeter. Another important task is to measure the antihelium/helium ratio with a sensitivity of the order of 10^{-7}. The detection of antihelium nuclei would be a significant discovery and it could indicate the presence of antimatter domains in a baryon symmetric Universe. Furthermore, the reconstruction of electron spectra up to 2 TeV allows to investigate a possible contribution of local sources to the cosmic radiation. Solar physics and solar modulation of cosmic ray particles can be studied by analysing low energy particles, i.e. $\lesssim 10$ GeV.

Cosmic ray particle	Energy range
Antiprotons	80 MeV - 190 GeV
Positrons	50 MeV - 270 GeV
Electrons	50 MeV - 400 GeV
Protons	80 MeV - 700 GeV
Electrons + positrons	up to 2 TeV
Light nuclei (up to Z = 6)	100 MeV/n - 250 GeV/n
$\overline{He}/He$	$O(10^{-7})$

Table 2.1. PAMELA performances for the detection of cosmic ray particles and antiparticles [38].

Chapter 3

Shower development in the PAMELA calorimeter

The PAMELA calorimeter is used to identify positron and antiproton events over a large background of protons and electrons respectively. Since leptons and hadrons interact in different ways, a powerful way to distinguish between these two types of events is to analyse the longitudinal and transverse shower profiles inside the calorimeter. An important characteristic of the hadronic showers is that neutral pions are produced during hadronic interactions and those π^0 rapidly decay into two photons thus initiating a component which propagates electromagnetically. This electromagnetic component could become prominent at high energies and could affect the discrimination between electromagnetic and hadronic showers in the calorimeter. The purpose of this thesis is to study neutral pion contamination in hadronic showers and the consequence for positron identification.

In this chapter the development of electromagnetic and hadronic showers in the calorimeter are described together with a description of the π^0 contamination. Furthermore, a detailed description of the transverse shower profile variables used in this work is presented.

3.1 Electromagnetic showers

An electromagnetic shower begins when an high-energy electron, positron or photon interacts with a material. A sketch of an electromagnetic shower is shown in figure 3.1.

The energy loss of electrons or positrons is dominated by the *bremsstrahlung* process above few tens of MeV in most materials, while *ionization* processes are predominant at low energies ($\lesssim 10$ MeV) [44]. During the *bremsstrahlung* process, electrons and positrons lose their energy via Coulomb interactions with the electric
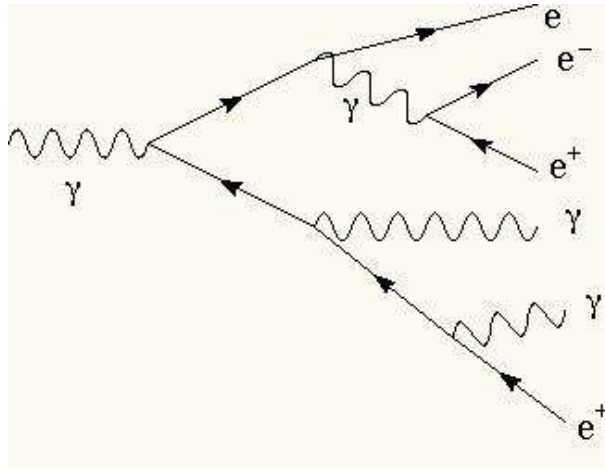
Figure 3.1. An electromagnetic shower initiated by a photon.

field generated by the atomic nuclei: the energy spectrum of the photons emitted during this interaction falls off as E^{-1} [45].

Photons instead interact with matter mainly via the *photoelectric effect*, *Compton scattering* and *electron-positron pair production*. Figure 3.2 shows the contributions of different processes to the photon total cross section as a function of energy in the case of lead [44].

The *photoelectric effect* occurs when an atom absorbs a photon and emits an electron. The photoelectric cross section varies with the photon energy as E^{-3} so this process dominates at low energies and it loses its importance very rapidly as the energy increases.

At higher energies, between approximately a few hundred keV and around 5 MeV, *Compton scattering* is the most likely process to occur [45]. In the Compton scattering process high energy photons lose energy colliding with stationary electrons and transferring to them some of their energy and momentum. The cross section for Compton scattering is almost proportional to the atomic number Z and decreases with increasing photon energy as $\sigma \sim E^{-1}$. Therefore, above a certain threshold energy, Compton scattering becomes more likely than the photoelectric effect. This threshold ranges from 20 keV for carbon (Z = 6) to 700 keV for uranium (Z = 92) [45].

When the photons have energies larger than twice the electron rest mass, i.e. 1.022 MeV, they may create, in the electric field of nuclei, *electron-positron pairs*. The cross section for pair production increases with energy and it reaches an asymptotic value for energies greater than 1 GeV; furthermore, since it is the only process where the cross section increases directly with energy, it is the most likely process to occur at high energies. Usually, the electron-positron pairs are caused by nuclear
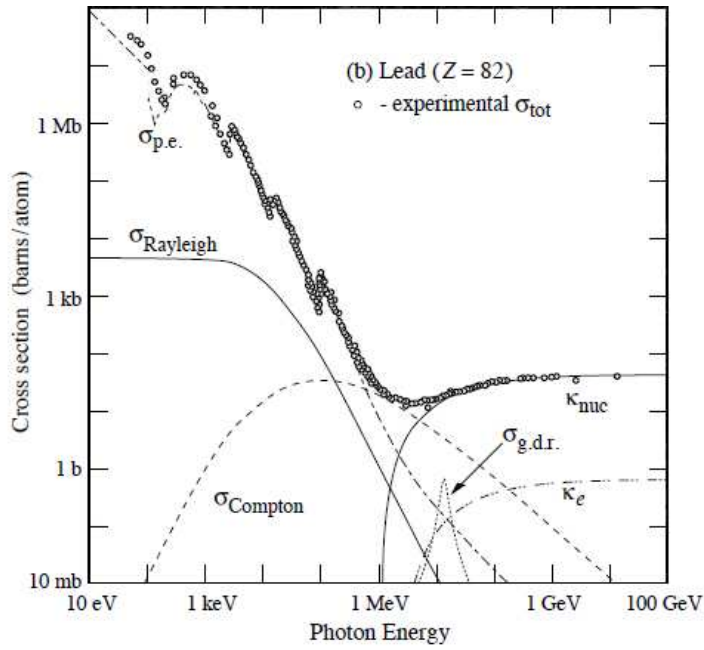
Figure 3.2. Contributions of different processes to the photon total cross section as a function of energy in lead: $\sigma_{p.e.}$ = photoelectric effect, $\sigma_{Rayleigh}$ = Rayleigh scattering, $\sigma_{Compton}$ = Compton scattering, K_{nuc} = pair production-nuclear field, K_e = pair production-electron field, $\sigma_{g.d.r.}$ = photonuclear interactions [44].

electromagnetic field; sometimes, for low-Z elements and at high energies they can also be created in the fields of the atomic electrons [45].

Since the development of electromagnetic showers is primarily determined by the electron density in the absorber medium, it is often convenient to describe the shower characteristics in a material-independent way, mainly using the **radiation length X_0** for the longitudinal development and the **Molière radius ρ_M** for the transverse one.

The *radiation length* is defined as the distance over which an electron or positron loses 63.2 % on average of its energy due to the bremsstrahlung process [45]. The radiation length for a single material (with atomic number Z and mass number A) can be evaluated by the following expression [44]:

$$X_0 = \frac{716.4 \ A}{Z \ (Z+1) \ ln(287/\sqrt{Z})} \ g \ cm^{-2} \tag{3.1}$$

The radiation length for a mixture of different material can be calculated as follows [45]:

$$\frac{1}{X_0} = \sum_i \frac{V_i}{X_i} \tag{3.2}$$

where V_i and X_i are respectively the fraction by volume and the radiation length (in mm) of the ith component of the mixture. This formula is needed in order to evaluate for instance the effective radiation length of the PAMELA calorimeter, consisting mainly of tungsten absorbers and silicon detectors.

The *Molière radius* is defined as follows [45]:

$$\rho_M = E_s \cdot \frac{X_0}{E_c} \tag{3.3}$$

where X_0 is the radiation length, E_c is the critical energy (see section 3.1.1) and the scale energy $E_s = m_e c^2 \sqrt{4\pi/\alpha} = 21.2$ MeV. About 90 % of the energy of an electromagnetic shower is deposited in a cylinder with radius ρ_M around the shower axis. Furthermore, the Molière radius is much less dependent on Z than the radiation length and to first approximation the Z dependence cancels. In fact, the radiation length is proportional to A/Z^2 and assuming $A \sim Z$ one obtains $X_0 \propto Z^{-1}$; considering that the critical energy is also proportional to Z^{-1} it is easy to see that ρ_M is independent of Z in first approximation [45].

3.1.1   The shower profiles

Via all the mechanisms described above, electromagnetic showers develop in the calorimeter. The average energy of the shower particles decreases until no further multiplications take place. The depth at which this occurs is called *shower maximum* and beyond this point the number of shower particles decreases. The

shower maximum is reached at a so-called *critical energy, E_c*. The critical energy is defined as the energy at which the average energy losses from radiation processes equal those from ionization. Among alternate definitions is that of Rossi [46], who defines the critical energy as the energy at which the ionization loss per radiation length X_0 is equal to the electron energy [44]:

$$\left[\frac{dE}{dX}\right]_{ion} X_0 = E \tag{3.4}$$

The critical energy is parameterised by the Particle Data Group as [44]:

$$E_c = \frac{610 \ MeV}{Z + 1.24} \tag{3.5}$$

This formula is valid for solids and liquids and shows the Z^{-1} dependence.

Note that if one describes the development of an electromagnetic shower in units of X_0 and ρ_M it becomes approximately material-independent.

The longitudinal profile

The longitudinal development is governed by the high-energy part of the cascade and therefore scales as the radiation length X_0 in the material. Figure 3.3 shows the longitudinal development of 10 GeV electron showers in different absorber materials. All the three profiles look very similar which means that they roughly scale with X_0. However, a couple of small differences are present: as Z increases, the shower maximum shifts to greater depth and beyond it the shower profile decreases more slowly. The result of these effects is that, for instance, a larger number of radiation lengths is needed in order to contain an electromagnetic shower in lead than in aluminium [45].

Another characteristic of the longitudinal shower profile is that it has a logarithmic energy dependence. Consider, for instance, an electron that emits a photon via the bremsstrahlung process. After having traversed one radiation length, the energy of the photon produced is half of the initial electron energy E_0. Thus, after n radiation lengths the electron has produced $N = 2^n$ secondaries (i.e. photons, electrons and positrons) each with an average energy $E = E_0/N$. As already mentioned, the cascade particles multiplication goes on until the average energy per particle drops below the critical energy E_c. The maximum development is reached after $n_{max} = ln \ (E_0/E_c) \ / \ ln \ 2$ radiation lengths and the maximum number of particles produced is $N_{max} = E_0/E_c$ [1].

The transverse profile

The transverse shower profile provides information about the energy deposit in a direction perpendicular to the shower axis. In the early stages of the shower development the transverse spread is caused by multiple scattering of electrons
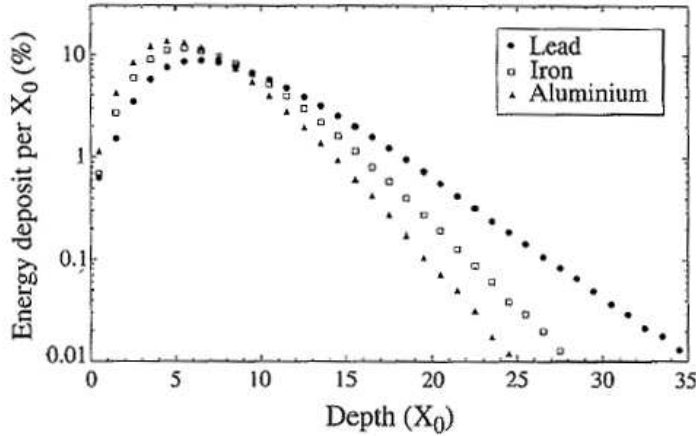
Figure 3.3. Longitudinal development of 10 GeV simulated electron showers in aluminium (black triangles), iron (open squares) and lead (black circles) [45].

and positrons, while beyond the shower maximum it is mainly due to the photons and electrons produced via Compton scattering and the photoelectric effect. Thus, radial shower profiles are characterised by a pronounced central core (the first component) surrounded by a halo (the second component). These features allow electromagnetic showers to be separated from hadronic ones. Usually transverse profiles are described in units of Molière radius ρ_M.

Electromagnetic shower development in the PAMELA calorimeter is shown in figure 3.4: the shower is initiated by a 100 GeV positron and is obtained by a GEANT3 simulation. The narrow core around the shower axis, where most of the energy is released, is clearly visible.

3.2   Hadronic showers

A hadronic interaction takes place when a hadron, e.g. a proton, enters a thick material. Strong interactions can arise between the shower particles and the nuclei of the absorbing medium resulting in a more complicated shower development compared to the electromagnetic one. Charged hadrons can ionize the atoms of the traversed medium and usually they interact strongly with the atomic nuclei. Neutral hadrons instead cannot ionize the medium: they lose their energies only by nuclear interactions. An important feature which characterises hadronic shower development is that *neutrons* are abundantly produced in nuclear interactions. On the contrary, the production of neutrons is lower in electromagnetic showers: thus,

Figure 3.4. Electromagnetic shower development in the PAMELA calorimeter: the shower is initiated by a 100 GeV positron and is obtained by a GEANT3 simulation. On the left and on the right the x-view (bending) and y-view (non-bending) of the apparatus are shown respectively; a view of the event from above is depicted too. The vertical red line corresponds to the z-axis. The colour scale indicates the detected energy in each calorimeter strip.

the neutrons detection could be a very powerful way to distinguish between electromagnetic and hadronic showers. Another important difference is the scale of the shower development which, in the hadronic case, is governed by the cross section for nuclear interactions.

In the first nuclear reaction mainly mesons, nucleons and photons are produced. These particles may lose their energy by ionization or interact in the calorimeter material causing a shower development. This is the case of neutral pions which rapidly decay into two photons, thus initiating electromagnetic shower development inside the hadronic one (see section 3.3).

3.2.1   The shower profiles

Hadronic shower development is governed by the **nuclear interaction length** λ_{int}. The nuclear interaction length of an absorber medium is defined as the average distance a hadron has to travel inside that medium before a nuclear interaction occurs. The relationship between λ_{int} and the total cross section σ_{tot} for nuclear interactions is [45]:

$$\sigma_{tot} = \frac{A}{N_A \; \cdot \; \lambda_{int}} \tag{3.6}$$

The total cross section is determined by the interactions between incident particles and target nuclei. The total cross section scales with $A^{2/3}$. The target cross section is related to the nuclei radius as r^2 and the volume is proportional to the atomic weight A, i.e. $r^3 \propto A$. Thus, using the previous formula, one can obtain that the radiation length λ_{int} is proportional to $A^{1/3}$ when λ_{int} is expressed in units of $g \cdot cm^{-2}$ [45].

Secondary particles, mainly pions, produced in the hadronic interactions, are emitted in the forward direction of the primary hadron. The spallation fragments are emitted instead more or less isotropically in the laboratory frame. For this reason the longitudinal and the transverse profiles are very different from those of the electromagnetic showers.

The longitudinal profile

Longitudinal profiles of hadronic showers have some similarities with those of electromagnetic showers. The number of particles produced during hadronic interactions rises roughly linearly and reaches a maximum which depends on the particle energy. Beyond the maximum particle multiplication is balanced by the absorption of shower particles; thus, the number of secondaries decreases and this decay is much less steep than the initial rise. In this case anyway any maximum lies deeper in the calorimeter for a given incident energy than in the electromagnetic showers: this is due to the fact that the mean free path for hadronic interactions is much longer than for electromagnetic processes. Thus, the absorption of hadronic showers requires more material compared to the absorption of electromagnetic showers of the same energy.

The transverse profile

Hadronic showers develop deeper in the calorimeter and are also much broader than electromagnetic ones. The lateral profile is usually composed by a narrow core, generated by the electromagnetic component, and a halo produced by the non-electromagnetic shower component. The narrow core is generated by neutral pions which induced an electromagnetic shower development inside the hadronic one (see section 3.3).

Hadronic shower development in the PAMELA calorimeter is shown in figure 3.5: the shower is initiated by a 100 GeV proton and is obtained by a GEANT3 simulation. Comparing this figure with an electromagnetic shower induced by a positron of the same energy (figure 3.4) it is clearly visible that a proton interacts deeper in the calorimeter and that the lateral profile of the initiated shower is broader.
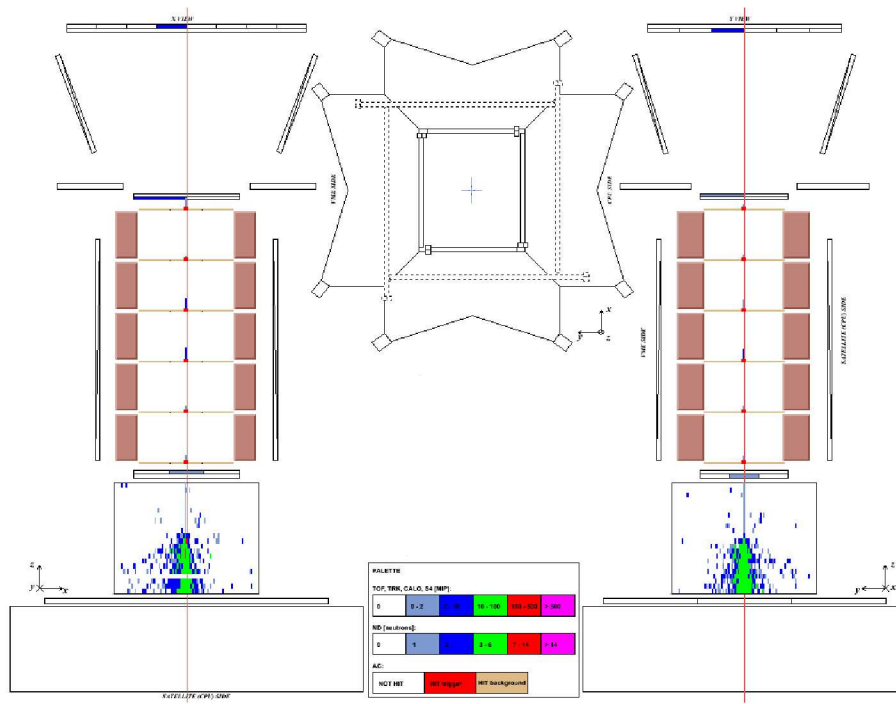
Figure 3.5. Hadronic shower development in the PAMELA calorimeter: the shower is initiated by a 100 GeV proton and is obtained by a GEANT3 simulation. On the left and on the right the x-view (bending) and y-view (non-bending) of the apparatus are shown respectively; a view of the event from above is depicted too. The vertical red line corresponds to the z-axis. The colour scale indicates the detected energy in each calorimeter strip.

3.3   The π^0 contamination of hadronic showers

As already mentioned, hadronic showers generally contain a component that propagates electromagnetically. For instance, when protons interact with nuclei in the first interaction charged and neutral pions are produced

$$p \; + \; N \to \pi^+, \; \pi^-, \; \pi^0 \tag{3.7}$$

While charged pions can interact with nuclei and produced other pions, neutral pions immediately decay into two photons

$$\pi^0 \to \gamma + \gamma \tag{3.8}$$

The mean lifetime for this process is $\tau = 8.4 \cdot 10^{-17}$ s [14] with a probability of about 0.99 [44]. Thus, these photons induce an electromagnetic shower producing electrons, positrons and other photons via Compton scattering, photoelectric effect and electron-positron pair production. It is important to stress that process 3.8 is not the only way in which photons are produced in hadronic interactions. During the first proton interaction with nuclei η mesons can be produced also and they can decay into two photons

$$\eta \to \gamma + \gamma \tag{3.9}$$

with a probability that is about 0.28 [44]. In the work described in this thesis only the process 3.8 has been taken into account.

Considering process 3.7, the average fraction f_{elm} of the initial hadron energy converted into π^0 increases according to a power law:

$$f_{elm} = 1 - (1 - f_{\pi^0})^n \tag{3.10}$$

where f_{π^0} is the fraction of neutral pions produced in the first interaction, $(1 - f_{\pi^0})$ is the non-electromagnetic component of the shower and n is the number of generations of reactions. On average, approximately $1/3$ of the mesons produced in the first interaction are neutral pions. It is necessary to stress that other particles are produced than just charged and neutral pions and therefore $f_{\pi^0} = 1/3$ should be considered as an upper limit [45]. Furthermore, the number of generations n is directly proportional to the energy of the particle that initiated the shower.

The transverse profiles of hadronic showers are thus characterized by an electromagnetic core caused by neutral pions. Since the electromagnetic showers develop in a smaller amount of material compared to the hadronic ones, on average the energy density is larger close to the shower axis and in the first stages of the shower development where most of the π^0s are generated.

In the PAMELA experiment hadrons and leptons with E > 2 GeV cannot be discriminated by using the dE/dx measurements provided by the time-of-flight system [39]. Thus, the different longitudinal and transverse shower profiles inside the electromagnetic calorimeter allow a high identification power between electromagnetic and hadronic showers. Since the identification of positrons over a large background

of protons is one of the main goal of the PAMELA experiment, the electromagnetic contamination of hadronic showers due to neutral pions could affect the discrimination between positron and proton events and it becomes extremely important within the context of the positron analysis. Schubnell [47] argues that the rise in PAMELA positron fraction [20] for energies greater than 10 GeV could be due to π^0 contamination of hadronic showers. A more detailed discussion is presented in section 4.5.

3.4 The PAMELA electromagnetic calorimeter

As already described in chapter 2 (section 2.1.3), the PAMELA electromagnetic calorimeter is formed by 44 single-sided silicon sensor planes interleaved with 22 plates of tungsten absorber. The silicon detectors form a total sensitive area of about (24×24) cm^2 and are arranged in a 3×3 matrix. Each silicon detector is segmented into 32 read-out strips thus forming 96 total strips for each plane. Furthermore, all the strips are connected creating 24 cm long strips.

The calorimeter was designed in order to contain electromagnetic showers: its total depth is 16.3 X_0 and up to energies of the order of 1 TeV the maximum of the electromagnetic cascade is well contained inside the calorimeter [43]. On the contrary, the total depth corresponds to ~ 0.6 nuclear interaction lengths only, thus ~ 40 % of the hadronic particles pass through the calorimeter without interacting. The longitudinal and transverse segmentation of the calorimeter combined with the energy released in each silicon strip gives a powerful way to identify electromagnetic showers [38].

The calorimeter reconstructs the energy of incident electrons independently from the tracking system. Figure 3.6. shows the energy dependence of the energy resolution of the calorimeter: the energy resolution for electrons shows a square root dependence on the energy reaching a constant value above 20 GeV of ~ 5.5 %. Up to 200 GeV it follows a quasi-linear behaviour as a function of the electron energy with deviations accounting for the partial containment at the highest energy. For energies greater than ~ 800 GeV the resolution decreases because of increasing longitudinal leakage and saturation of the signal from the strips (~ 1100 MIP) [43]. One MIP is the energy deposited by a minimum ionising particle. The mean rate of energy loss by relativistic particles traversing a material is governed by the Bethe-Bloch equation: the trend of this equation as a function of the particle momentum has a minimum due to ionisation processes which lies around $1 - 2$ MeV cm^2 g^{-1} [44].

3.4.1 Shower profile variables

In order to study the π^0 contamination of hadronic showers in the PAMELA calorimeter, shower profiles have been studied in a detailed way using GEANT3 simulations (see chapter 4). The variables used to distinguish between electromagnetic and hadronic interactions are described below, where the term *strips* refers to
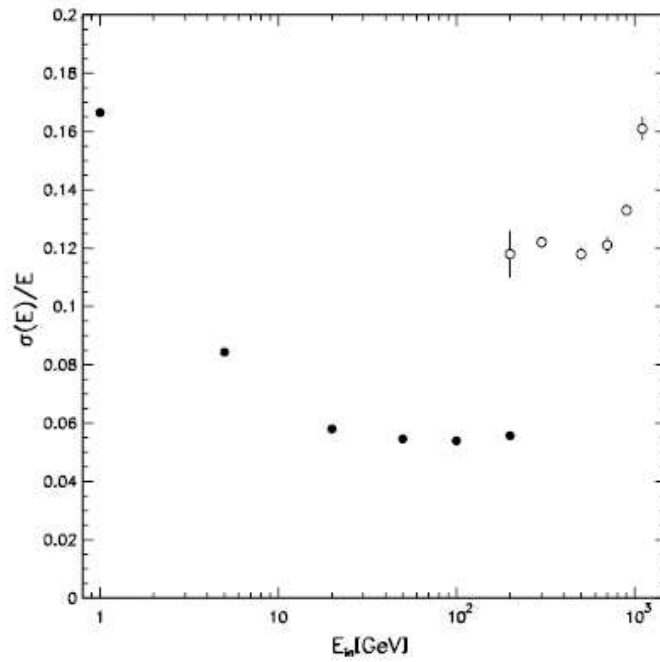
Figure 3.6. The energy dependence of the energy resolution of the electromagnetic calorimeter. The black filled points are for normal operation (experimental data) and the open circle points are for the self-trigger mode (simulations) described in section 2.2.1 [38].

.

the silicon strips which constitute each detector plane (see section 2.1.3) and *track* refers to the track as reconstructed by the tracker:

- ***qtot*** $\rightarrow$ total energy detected in the calorimeter;

- ***qtrack*** $\rightarrow$ energy deposited in the strips along the track and in the neighbouring strips on each side;

- ***qmax*** $\rightarrow$ the maximum energy detected in a strip;

- ***qcyl*** $\rightarrow$ energy deposited in a cylinder of radius 8 strips around the shower axis;

- ***qtr*** $\rightarrow$ energy deposited in a cylinder of radius 4 strips around the shower axis;

- ***qpresh*** $\rightarrow$ energy deposited in a cylinder of radius 2 strips around the shower axis and only in the first 4 planes of the calorimeter;

- ***qtotimp*** $= qtot \ / \ rigidity$;

- ***qm*** $= qmax \ / \ qtrack$;

- ***q1*** $= qcyl \ / \ qtot$;

- ***q2*** $= qtrack \ / \ qtr$;

- ***q3*** $= qtrack \ / \ qtot$;

- ***qt1*** $= qtrack \ / \ qcyl$;

- ***nstrip*** $=$ total number of strips hit in the calorimeter;

- ***ncyl*** $=$ number of strips hit in a cylinder of radius 8 strips around the shower axis;

- ***ncore*** $= \sum_{j=1}^{2} \sum_{i=1}^{pl_{max}} n_{hit}(i,j) \cdot i$, where n_{hit} is the number of hit strips in the ith plane of view j^{th} within a cylinder of radius $2\rho_M$ around the shower axis; the final value is obtained summing over all the calorimeter planes up to the plane number pl_{max} closest to the calculated electromagnetic shower maximum.

In the PAMELA calorimeter a radius of $2\rho_M$ around the shower axis corresponds to 8.5 silicon strips [43]. Furthermore, the shower axis is defined by extrapolating the particle track reconstructed by the spectrometer. Figures 3.7, 3.8, 3.9, 3.10 and 3.11 show the distributions of the quantities listed above for simulated 100 GeV positrons and protons.

The *ncore* distribution (figure 3.8-*top*) shows that in electromagnetic showers the particle multiplicity increases with the calorimeter depth up to the shower maximum and also that shower particles are collimated along the shower axis.

Furthermore, it is clear that showers induced by protons are broader since a lower number of strips are hit inside a cylinder of radius $2\rho_M$ around the shower axis.

The *qtotimp* variable corresponds to the total energy deposited in the calorimeter divided by the rigidity reconstructed by the spectrometer. Its distribution (figure 3.8-*bottom*) is essentially flat for protons with a peak at low energies for the non-interacting ones. In the positron case, the energy is normally distributed as long as most of the shower is contained inside the calorimeter [43]. This behaviour can also be seen in figure 3.7 where the distribution of the total energy detected in the calorimeter, *qtot*, is plotted.

The *qm* quantity displays the differences of transverse profiles (figure 3.9-*top*): in the shower induced by positrons the maximum energy is released along the event track and thus the *qm* distribution shows a narrow peak close to zero; *qm* assumes higher values in the proton case, since hadronic interactions or nuclei fragmentations can take place far away from the shower axis.

The *qpresh* variable is related to the starting point of the shower. In fact, the probability that an electromagnetic shower starts in the first 3 planes of the calorimeter is greater than 89 % [43] while for hadronic showers the starting point is distributed more uniformly. Thus, the *qpresh* distribution (figure 3.9-*bottom*) shows that showers induced by positrons start mostly in the first planes of the calorimeter while protons with the same initial energy interact deeper.

The distributions of *q1*, *q2*, *q3* and *qt1* (figures 3.10 and 3.11) are very similar. These quantities describe the fraction of calorimeter energy deposited inside a cylinder around the shower axis. In the electromagnetic showers these distributions show a sharp peak according to the fact that mostly of the energy is released along the shower axis. In the hadronic showers the energy deposited close to the shower axis is lower than in the electromagnetic case. Furthermore, all the four distributions in the proton case show a peak about unity which corresponds to non-interacting protons. The *q1* variable is the fraction of calorimeter energy deposited inside a cylinder of radius 8 strips ($\sim 2\rho_M$) around the shower axis: in the electromagnetic showers *q1* ~ 0.9, thus 90 % of the energy released in the calorimeter is detected within 8 strips from the shower axis. The *q3* quantity is similar to *q1* but in this case it is the fraction of calorimeter energy deposited in the strips closest to the event track: showers initiated by positrons have *q3* ~ 0.5 - 0.6. A simple calculation shows that *qt1* = *qtrack* / *qcyl* = *q3* / *q1* and its distribution in the positrons case has a sharp peak around 0.6: this means that ~ 60 % of the energy detected within 8 strips from the shower axis is deposited in the strips closest to the track. The variable *q2* is similar to *qt1* but in this case it is the ratio between the energy deposited in the strips closest to the track and that deposited inside a cylinder of radius 4 strips around the shower axis.
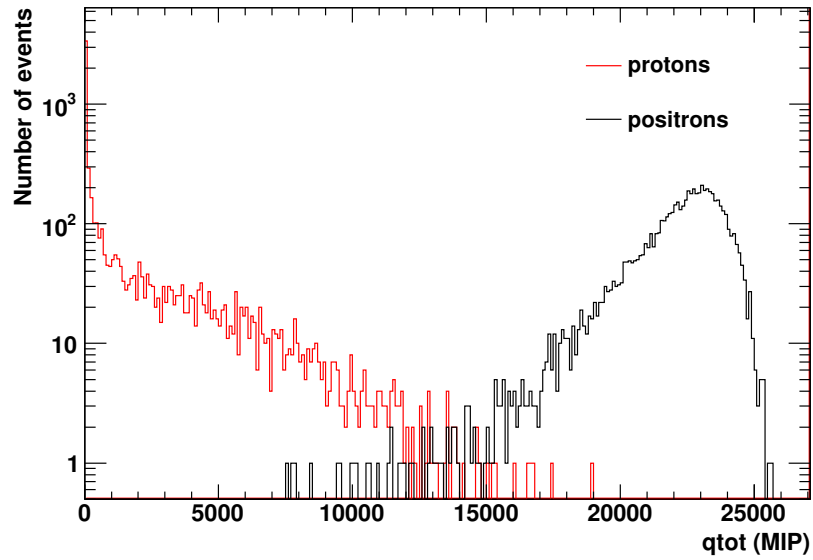
Figure 3.7. Distribution of the total energy detected in the calorimeter (*qtot*) for 100 GeV simulated positrons (black line) and protons (red line). 1 MIP is the energy deposited by a minimum ionising particle.
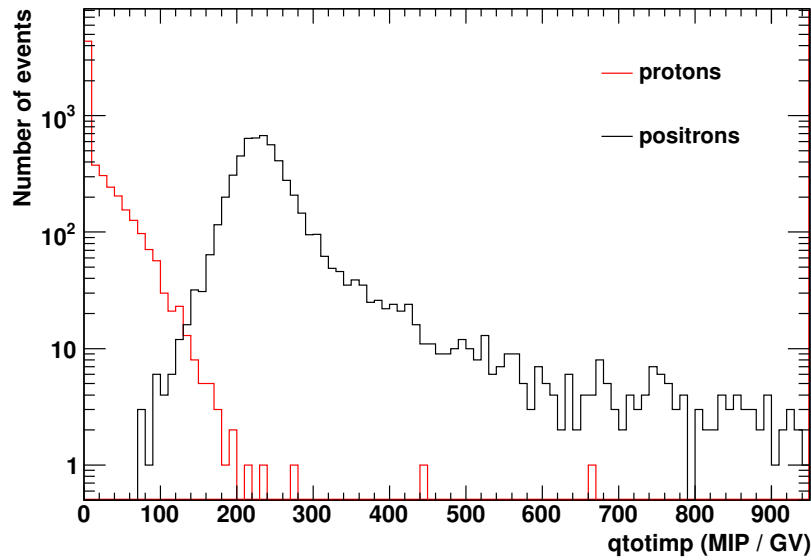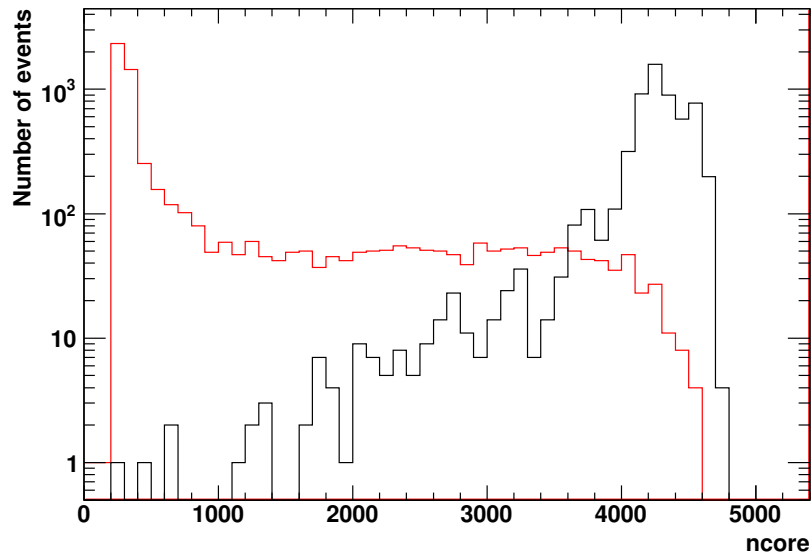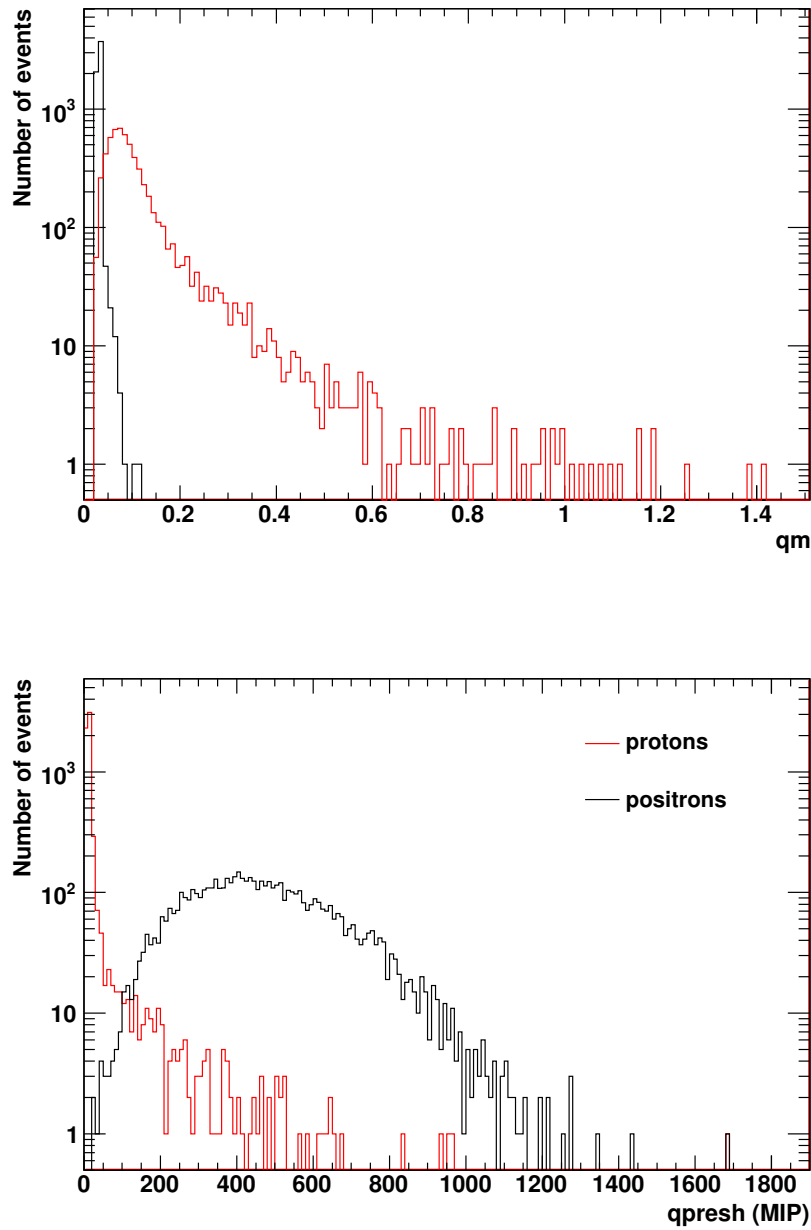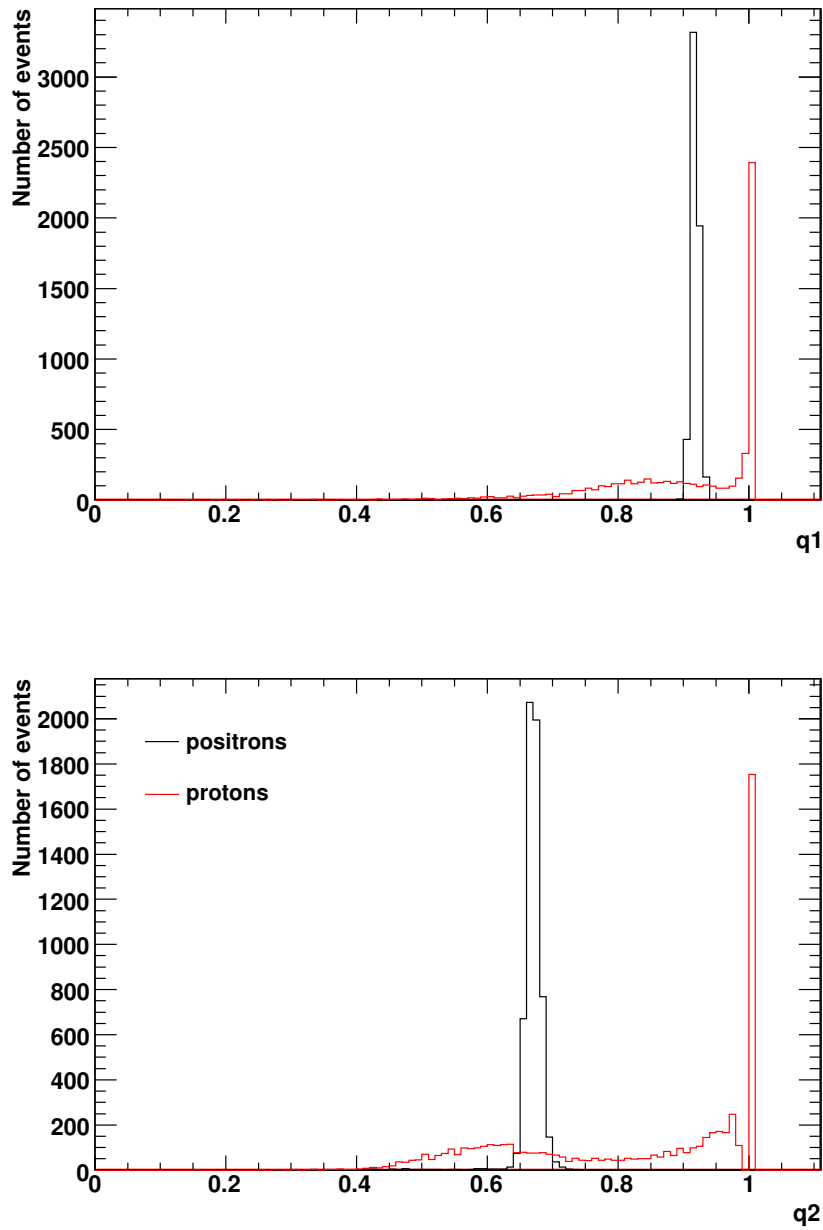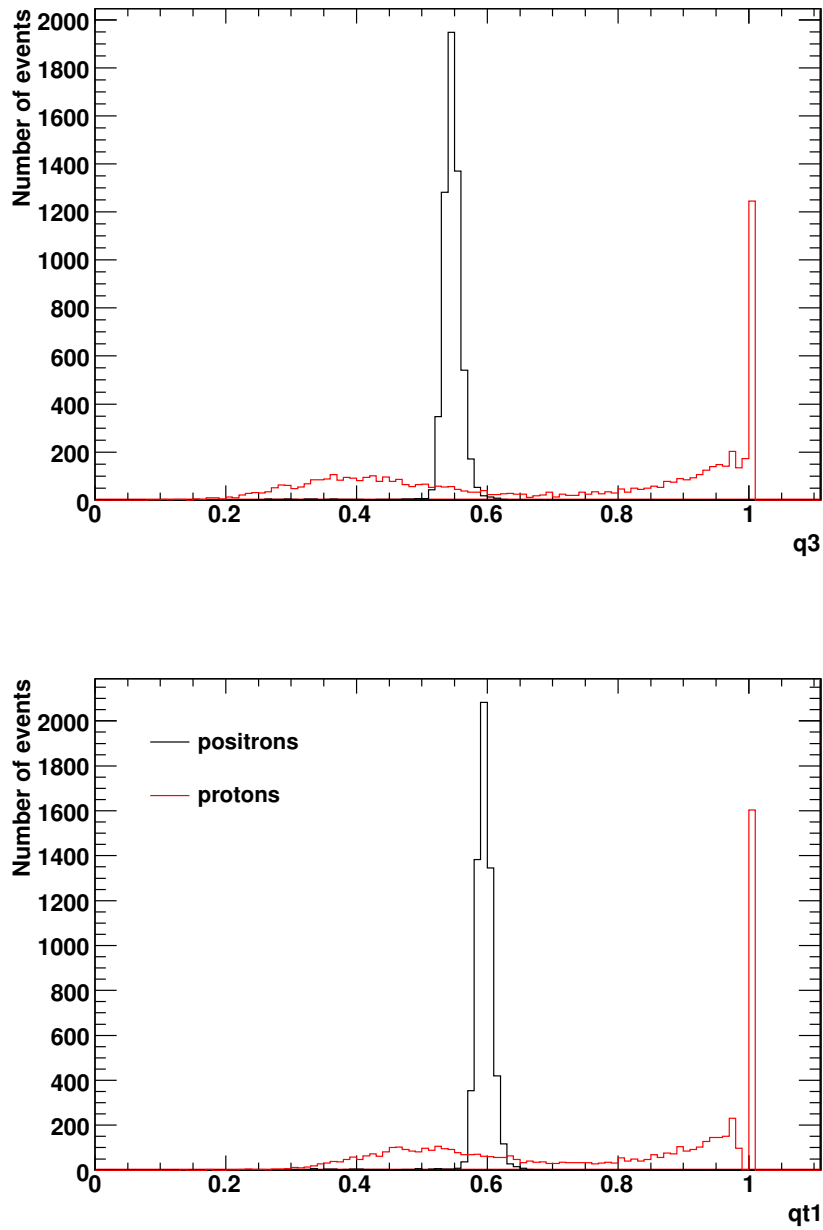
Figure 3.8. Distributions of some shower profile variables for 100 GeV simulated positrons (black line) and protons (red line). *Top*: distribution of *ncore* as defined in the text. *Bottom*: distribution of *qtotimp = qtot / rigidity*. 1 MIP is the energy deposited by a minimum ionising particle.

Figure 3.9. Distributions of some shower profile variables for 100 GeV simulated positrons (black line) and protons (red line). *Top*: distribution of $qm = qmax / qtrack$. *Bottom*: distribution of $qpresh$ as defined in the text. 1 MIP is the energy deposited by a minimum ionising particle.

Figure 3.10. Distributions of some shower profile variables for 100 GeV simulated positrons (black line) and protons (red line). *Top*: distribution of *q1 = qcyl / qtot*. *Bottom*: distribution of *q2 = qtrack / qtr*. 1 MIP is the energy deposited by a minimum ionising particle.

Figure 3.11. Distributions of some shower profile variables for 100 GeV simulated positrons (black line) and protons (red line). *Top*: distribution of $q3 = qtrack / qtot$. *Bottom*: distribution of $qt1 = qtrack / qcyl$. 1 MIP is the energy deposited by a minimum ionising particle.

Chapter 4

Simulation studies of π^0 contamination

Hadronic interactions in the calorimeter produce mainly charged and neutral pions. Charged pions can interact with nuclei and produce other pions while neutral pions decay mostly into two photons. These photons initiate electromagnetic showers which develop inside the hadronic cascades (see section 3.3) and which may result in a proton being misidentified as a positron.

In order to study this electromagnetic component in hadronic showers, simulations of hadronic and electromagnetic showers induced by protons and positrons respectively have been produced and studied. The simulation code of the entire apparatus is a Monte Carlo program based on the GEANT code, version 3.21, and it was developed by the PAMELA Collaboration. The simulation code was also modified in order to artificially increase the number of neutral pions produced in hadronic showers and study the consequences for positron identification.

In this chapter part of the simulation code and the related changes used in this analysis are described. Positron selection criteria used to derive the published PAMELA positron fraction are then presented and applied to positron and proton simulated samples respectively. Furthermore, a new approach using shower profile variables in the calorimeter have been studied in preparation for extending the positron selection to higher energies (> 100 GeV). Results and conclusions of this analysis are shown at the end of the chapter.

4.1 GEANT3 simulations

As described in section 3.3, hadronic showers contain an electromagnetic component initiated by the neutral pions. In order to study the π^0 contamination of hadronic showers simulations of protons and positrons interacting in the calorimeter have been produced and studied.

The simulations have been performed using GPAMELA, the PAMELA Collaboration's official simulation code. GPAMELA is a Monte Carlo program based on the GEANT package [48] version 3.21 and was developed by the PAMELA Collaboration. The simulation code reproduces in detail PAMELA subdetectors, including all the mechanical parts inside the experiment acceptance and the pressurized vessel which contains the apparatus.

The GPAMELA code consists of three main parts; each part calls different subroutines which were implemented for different tasks. These three main parts are:

1. *initialization* → this is the initial phase where all the data structures and parameters are initialized and prepared for the event simulation. This phase is controlled by the user in the subroutine UGINIT. Each step is controlled both by default GEANT subroutines and GPAMELA user subroutines which are identified by the prefix GP:

   - the input datacards, chosen by the user in the subroutine GPFFR, are interpreted;

   - the subroutine GSPART creates the data structure JPART with the particle properties;

   - the subroutine GPMAT creates the data structure JMATE with the characteristics of the materials used;

   - the geometrical volumes which constitute the detector are defined in the subroutines GPGEO and GPDAT and stored in the JVOLUM data structures;

   - the tracking medium parameters are defined in the subroutine GPMED;

   - the sensitive elements of the geometrical volumes are defined in the subroutine GPHIT;

   - all the geometrical information defined by the user are processed in the subroutine GGCLOS;

   - the energy loss and cross section tables are calculated and store in the data structure JMATE by the subroutine GPHYSI.

   At the end of this phase everything is ready for the particle transportation;

2. *event processing* → this is the main phase where primary particles are followed inside the detector, from the generation point to the final step; it is controlled by the subroutine GRUN. Each step of the generated events is analysed by different subroutines; here a list of the most important ones:

   GUKINE reads or generates the kinematics of the primary particle track (i.e. particle arrival direction (θ, ϕ), energy, etc.) and stores it in specific data structures;

GUTREV controls the propagation of each particle by calling the subroutine GUTRACK;

GUTRACK controls the tracking of one event; if a particle passes through a sensitive detector, all useful information "hits" are stored in the data structure JHITS;

GUSTEP controls each tracking step along the track. This subroutine can store a hit or transfers a secondary product; also, coordinates of points along the track are stored;

GUPHAD calls the hadronic package for cross section calculation, in case of hadronic interaction; the hadronic package is selected by the user;

GUDIGI controls the response of different detectors using information stored during the particle transportation in the data structures JHITS; the results are then stored in a specific data structure;

GUOUT is called at the end of one event and performs the final processes, such as output the relevant data structures.

3. *termination* → this is the last phase, where final results are printed and histograms are saved; it is controlled by the subroutine UGLAST.

The default configuration of geometric volumes defined in GPAMELA is shown in figure 4.1. The geometric volumes included in this configuration are: the time-of-flight system (S1, S2 and S3), the magnetic spectrometer, the electromagnetic calorimeter, the anticoincidence system (CAS, CAT and CARD), the neutron detector and the bottom scintillator plane S4. The pressurized vessel which encloses the whole apparatus is also included. With respect to the PAMELA reference system (figure 2.2) the GPAMELA reference system is shifted *49.229 cm* down along the z-axis; thus, in the GPAMELA reference system, the origin of the PAMELA reference system has coordinates $(x_0, y_0, z_0) = (0, 0, 49.229)$ [49]. Also, all the simulated events presented in this work have been generated on a surface with dimensions 2×2 m^2 positioned at z = 1.095 m (figure 4.1).

Proton events have been simulated using the FLUKA hadronic generator package. In FLUKA different models are used depending on the energy of the primary particle [49]. The total cross section for hadronic interactions is evaluated during the *event processing* phase since it depends on the nature of the incident particle. Thus the cross section is evaluated during the particle tracking process by FLUKA subroutines.

4.2 "Only-π^0 case" simulations

As described in section 3.3, hadronic showers contain an electromagnetic component which could have relevant consequences for positron identification. Thus, the main goal was to quantify the electromagnetic contamination of hadronic showers using GEANT3 simulations (see section 4.1).
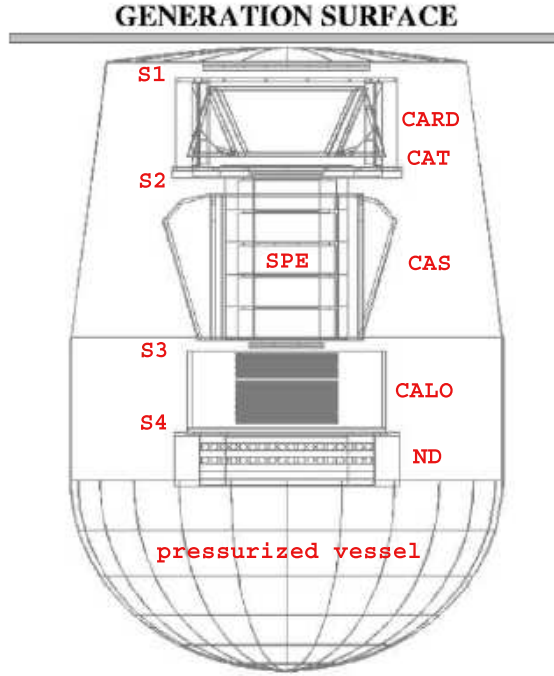
Figure 4.1.   Configuration of the PAMELA apparatus as simulated by the GPAMELA code [49]. This configuration includes: the time-of-flight system (consisting of the scintillator planes S1, S2 and S3), the magnetic spectrometer (SPE), the electromagnetic calorimeter (CALO), the anticoincidence system (CAS, CAT and CARD), the neutron detector (ND) and the bottom scintillator plane S4. The pressurized vessel which contains the whole apparatus is also included. The generation surface is shown on the top: it has dimensions 2×2 m and it is positioned at z = 1.095 m.

The fundamental idea of the work described in this thesis is to *increase* the number of π^0s produced in hadronic showers and to study the characteristics of the corresponding shower profiles. An artificial way of increasing the number of π^0s is to change *all the charged pions* produced in one hadronic shower into neutral ones, assuming similar production characteristics for charged and neutral pions, like for instance angular distribution and cross section. Of course, this is a non-physical process but it allowed the π^0 contamination to be studied in a straight-forward way, without modifying the cross section of the primary proton in the GEANT3 simulation package. As mentioned in section 4.1 the cross section is evaluated by FLUKA subroutines during the particle tracking process since it depends on the nature of the particle and on the interaction type. Thus changing the cross section of the primary proton imply changes in the cross section calculations of all the other secondary interaction processes, a thing that is difficult to handle.

The changes of all the charged pions into neutral ones were made to the GUSTEP subroutine of the GPAMELA code where the secondary particles are processed (section 4.1). In this subroutine secondary particles are transfered either to the JSTAK stack or to the JVERTX and JKINE event structures by calling the GSKING subroutine. In the JSTAK data structure secondary particles generated by the current transported particle are processed before proceeding to the next particle [49]. The changes were written at the end of the GUSTEP subroutine, just before the call to the GSKING subroutine. Furthermore, this change was made for all the π^+ and π^- produced in hadronic interactions in all the PAMELA apparatus, but in the subsequent analysis (sections 4.5, 4.6 and 4.7) only events interacting in the calorimeter have been considered (section 4.4).

Note that, from now on, proton simulations produced with this change will be mentioned as **only-π^0 case** while usual proton simulations will be mentioned as **normal case**.

4.2.1 Preliminary results

In order to check the method described in section 4.2 the number of charged and neutral pions produced in hadronic showers in both the *only-π^0* and the *normal case* were counted and compared. Simulations of 10000 monoenergetic protons, vertically incident on the generation surface (figure 4.1), have been produced in both cases. The results obtained are shown in tables 4.1, 4.2 and 4.3 for proton simulations with energy 30 GeV, 50 GeV and 100 GeV respectively.

Observing the number of secondary pions produced one can notice that the total number of pions in the *normal* and in the *only-π^0 case* (Total_{normal} and $\text{Total}_{only-\pi^0}$) for all the three monoenergetic simulations are different. This is due to the fact that in the normal case charged pions produced in the proton first interaction can have hadronic interactions producing other π^+ and π^-. In the only-π^0 case however as soon as $\pi^\pm$s are produced they are immediately converted into π^0s, thus interrupting the production of further $\pi^\pm$s.

Case	π^0	π^+	π^-	Total pions
Normal	31416	28286	27490	87192
Only-π^0	61137	0	0	61137
$\text{Total}_{only-\pi^0}$ / $\text{Total}_{normal} = 0.70$				

Table 4.1. Counts of charged and neutral pions produced in hadronic showers in both the *normal* and the *only-π^0 case*. 10000 vertically incident and monoenergetic protons are simulated; in this case **E = 30 GeV**. Only secondary particles produced in the calorimeter are counted.

Case	π^0	π^+	π^-	Total pions
Normal	42621	38554	38005	119180
Only-π^0	81124	0	0	81124
$\text{Total}_{only-\pi^0}$ / $\text{Total}_{normal} = 0.68$				

Table 4.2. Counts of charged and neutral pions produced in hadronic showers in both the *normal* and the *only-π^0 case*. 10000 vertically incident and monoenergetic protons are simulated; in this case **E = 50 GeV**. Only secondary particles produced in the calorimeter are counted.

Case	π^0	π^+	π^-	Total pions
Normal	62875	57422	57619	177916
Only-π^0	110722	0	0	110722
$\text{Total}_{only-\pi^0}$ / $\text{Total}_{normal} = 0.62$				

Table 4.3. Counts of charged and neutral pions produced in hadronic showers in both the *normal* and the *only-π^0 case*. 10000 vertically incident and monoenergetic protons are simulated; in this case **E = 100 GeV**. Only secondary particles produced in the calorimeter are counted.

The same results for 100 GeV protons are also shown in figures 4.2, 4.3, 4.4 and 4.5 where the distribution of total secondary particles, π^0, π^+, π^-, positrons, electrons and photons are shown. As one can notice (figure 4.2 and 4.3-*top*), in the *only-π^0 case* (blue line) there are no charged pions and the number of π^0 is larger than in the *normal case* (red line). Consequently, since in the *only-π^0 case* a larger number of π^0 is produced, a larger number of electrons, positrons and photons is produced too (figure 4.3-*bottom* and 4.4). This results also in an increase of all the secondary particles produced in the calorimeter (figure 4.5).

4.3 Simulations analysis

In order to study the electromagnetic contamination of hadronic showers, simulations of positron and proton events have been produced and studied. Standard selection criteria for positron identification (see section 4.4) have been applied to:

- simulated positron sample, in order to find the cut efficiencies

- simulated proton sample (*normal case*), in order to study the contamination

- simulated proton sample (*only-π^0 case*), in order to study the contamination

Two sets of simulations have been produced in different energy ranges:

1. 20 - 100 GeV

2. 100 - 300 GeV

All the events have been randomly generated with an inclination angle $\theta = (0, 20)°$ (the maximum track inclination allowed by the PAMELA geometrical factor is $20°$ [42]) and an azimuth angle $\phi = (0, 359)°$. The events have been generated with an energy spectrum $\propto \mathrm{E}^{-2.7}$ for protons and $\propto \mathrm{E}^{-3.0}$ for positrons, in agreement with cosmic ray measurements of proton and electron spectra (see section 1.1).

The simulations produced in this work are summarized in table 4.4. Hadronic shower developments in the *only-π^0 case* are also shown in figure 4.6: the events belong to simulations produced in the energy range $20 - 100$ GeV. The shower development in the calorimeter looks very different in the two cases: the event depicted in figure 4.6-*top* is similar to an hadronic cascade without any pion modifications (see figure 3.5); the event shower development shown in figure 4.6-*bottom* has instead a very pronounced core and is more similar to an electromagnetic cascade (see figure 3.4).

In the following section, the analysis of the simulations listed in table 4.4 is described.
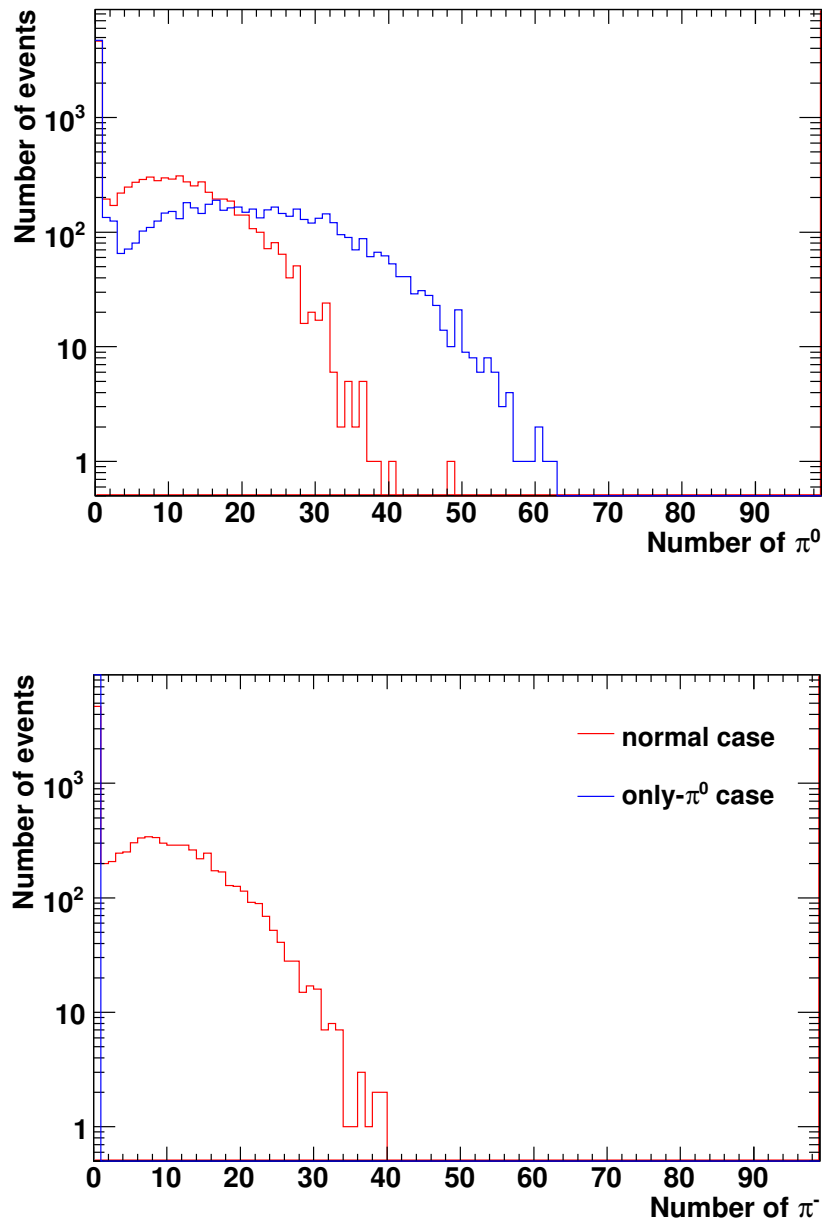
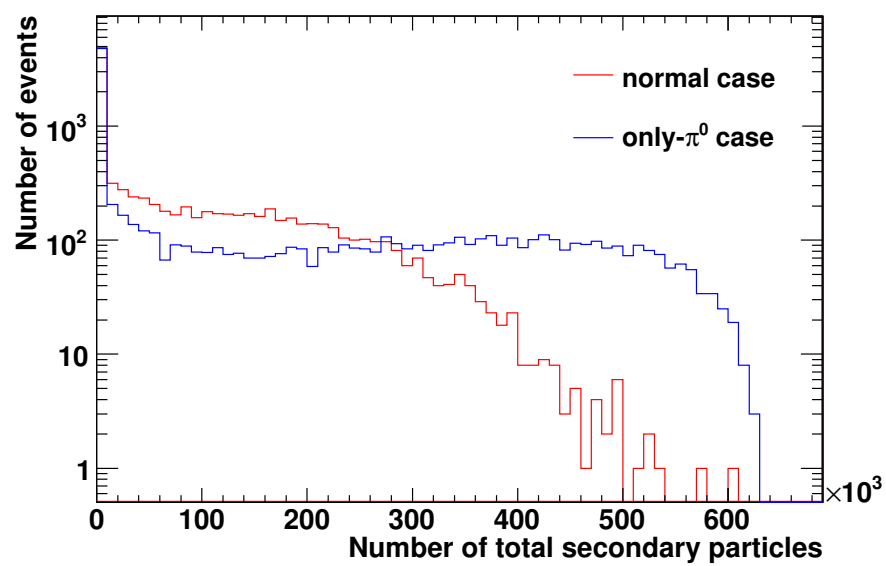**Figure 4.2.** Distributions secondary particles produced in the PAMELA calorimeter and obtained by simulations of 100 GeV protons in the *normal case* (red line) and in the *only-π^0 case* (blue line). *Top*: distributions of π^0. *Bottom*: distributions of π^-.
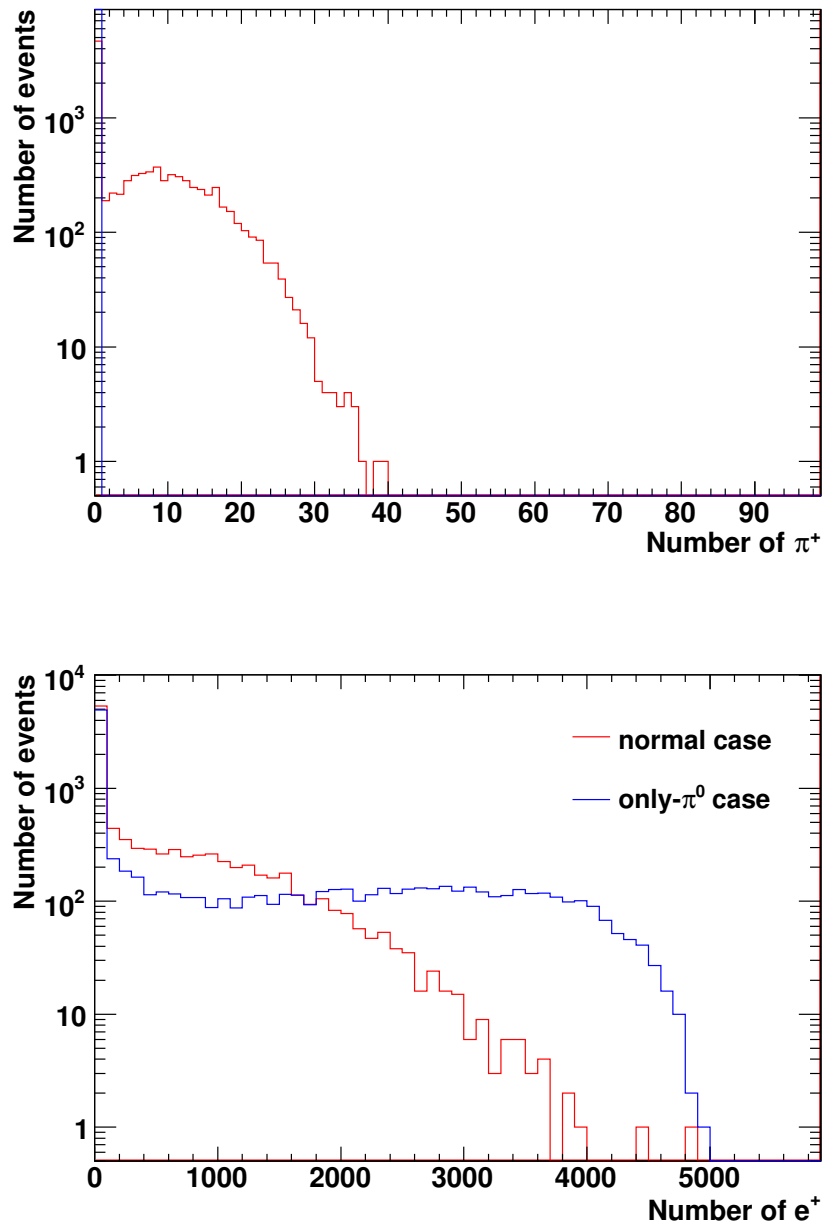
Figure 4.3. Distributions of secondary particles produced in the PAMELA calorimeter and obtained by simulations of 100 GeV protons in the *normal case* (red line) and in the *only-π^0 case* (blue line). *Top*: distributions of π^+. *Bottom*: distributions of positrons.
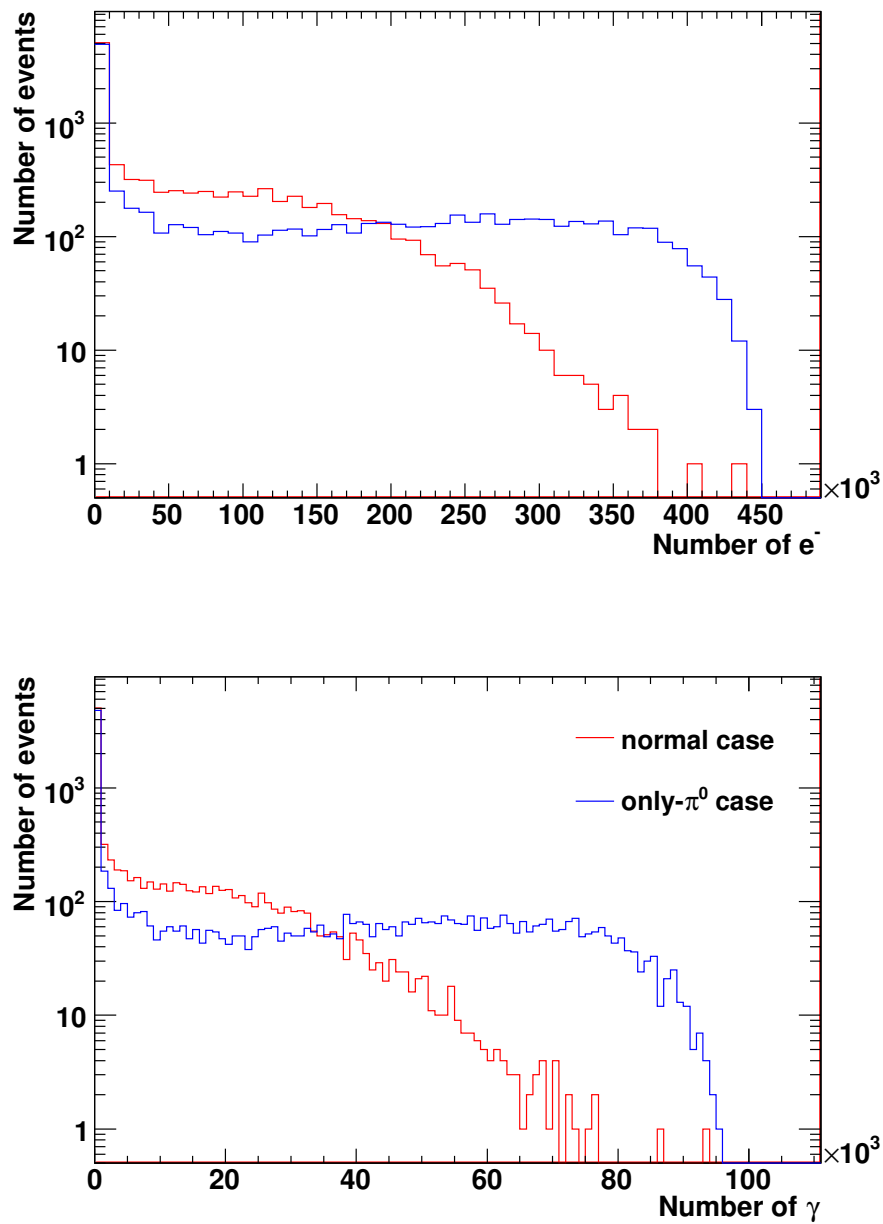
Figure 4.4. Distributions of secondary particles produced in the PAMELA calorimeter and obtained by simulations of 100 GeV protons in the *normal case* (red line) and in the *only-π^0 case* (blue line). *Top*: distributions of electrons. *Bottom*: distributions of photons.

Figure 4.5. Distributions of all secondary particles produced in the PAMELA calorimeter and obtained by simulations of 100 GeV protons in the *normal case* (red line) and in the *only-π^0 case* (blue line).
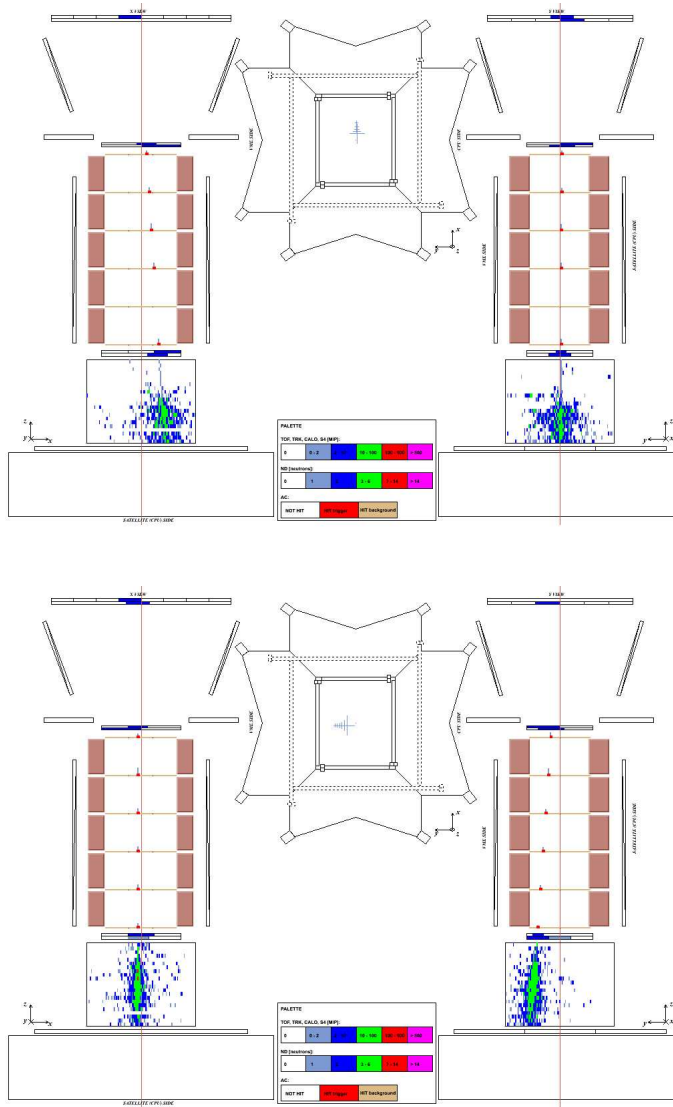
Figure 4.6.   Two different examples of hadronic shower development in the PAMELA calorimeter in the *only-π^0 case* simulations. The events have been randomly generated with an inclination angle $\theta = (0, 20)^\circ$ and an azimuth angle $\phi = (0, 359)^\circ$, also according to an energy spectrum $\propto E^{-2.7}$. The vertical red line corresponds to the z-axis. *Top*: event with a tracker reconstructed rigidity of 47.6 GV; the shower development is similar to an hadronic one generated in the normal case (see figure 3.5). *Bottom*: event with a tracker reconstructed rigidity of 41.6 GV; in this case the shower development has a very pronounced core and is more similar to an electromagnetic shower development (see figure 3.4).

E = (20 - 100) GeV	E = (100 - 300) GeV
10^5 positrons	$6 \cdot 10^4$ positrons
10^5 protons (*normal case*)	10^5 protons (*normal case*)
$5 \cdot 10^5$ protons (*only-π^0 case*)	$5 \cdot 10^5$ protons (*only-π^0 case*)

Table 4.4. Number of simulated positrons and protons (*normal* and *only-π^0 case*) in two different energy ranges.

4.4 Positron selection criteria

The standard positron selection criteria can be summarized as:

- tracker selections

- ToF selections

- anticoincidence selections

- calorimeter selections

- shower topological selections in the calorimeter

4.4.1 Tracker selections

As described in section 2.1.2, the magnetic spectrometer allows charged particle deflection η to be measured as well as the rigidity. Furthermore, particle tracks are reconstructed using spatial information from the energy released in the six silicon layers. The following cuts are used in order to select events with a good reconstructed track:

1. $\chi^2 > 0$

2. number of integration steps in the track fitting algorithm < 100

3. $(\chi^2)^{0.25} < 1.97 + 1.85 \cdot \eta$

4. number of hits in the x-view ≥ 4

5. number of hits in the y-view ≥ 3

6. MDR $> 6 \cdot$ rigidity

7. dE/dx averaged over all the planes < 2 MIP

The first two selections put constraints on the quality of the fitted track and select events with a single track reconstructed by the tracker. The third selection sets an upper limit on the evaluated χ^2, rejecting particles scattered on the tracker planes or events with multiple tracks. The fourth and the fifth cuts select tracks

with limits on the number of hits, used to perform the fit, on the tracker layers, both on the bending x-view and non-bending y-view, ensuring a good quality of the track. Furthermore, it is also required that the MDR for each event should be 6 times larger than the reconstructed rigidity (sixth cut): since MDR = $1 / \Delta\eta$, this selection eliminates all the events with a high error $\Delta\eta$ on the estimated deflection. Finally, the last cut selects events which do not release an energy greater than 2 MIP in all the silicon layers (1 MIP is the energy deposited by a minimum ionising particle); thus, particles which pass through the tracker without interacting are selected.

4.4.2   Time-of-flight selections

The time-of-flight system (see section 2.1.1) provides the main PAMELA trigger, where coincidental energy deposits are required in the three scintillator planes. The absolute value of charge, z, of the incident particles is also determined by measuring the ionisation energy loss (dE/dx) in the scintillators. Furthermore, the ToF system measures the time-of-flight of the particles passing through its planes: thus, the velocity β of incident particles is derived combining this information with the track length obtained from the spectrometer. The selection criteria regarding the time-of-flight system are the following:

1. no more than one hit paddle on the scintillator layers S11, S12, S21 and S22

2. no more than 20 hit photomultipliers

These cuts select non-interacting particles on the silicon layers above the tracker and also reject multiparticle events.

4.4.3   Anticoincidence selections

As already mentioned in section 2.1.5, the anticoincidence system permits identification of secondary particles produced via interactions of the primary ones with the PAMELA apparatus. In order to remove these *false trigger events*, the following events are selected:

1. events without signals in CARD scintillators

2. events without signals in CAT scintillator

Events which produce signals in CAS scintillators are instead not rejected since particles backscattered from the calorimeter can hit the anticoincidence scintillators surrounding the tracker.

4.4.4   Calorimeter selections

The main task of the electromagnetic calorimeter is the identification of electromagnetic and hadronic showers allowed by its longitudinal and transverse segmentation (see section 2.1.3).

Selections on the hit strips are applied for a containment requirement: since a radius of 2 ρ_M around the shower axis corresponds to 8.5 silicon strips [43] only events that shower $\sim 8 - 9$ strips away from the calorimeter borders are selected thus ensuring that $\sim 95\,\%$ of the shower energy is contained inside the calorimeter. Selections regarding the shower development are also considered:

1. $tmaximp = tmax\ /\ log(qtot) < 1.5$

2. $noint < 5 \cdot (1 + 5 \cdot \mathrm{e}^{-0.1\,\cdot\,R})$

where $qtot$ is the total energy detected in the calorimeter and is measured in MIP, i.e. the energy deposited by a minimum ionising particle.

The first selection is related to the shower longitudinal development: for each event, the shower longitudinal development in the calorimeter is fitted and the maximum $tmax$ of the fit is evaluated in units of radiation length X_0. Simulations in the energy range $20 - 100$ GeV show that $tmaximp < 1.5\ \mathrm{X_0/MIP}$ selects $97.5\,\%$ of positrons and $43.2\,\%$ of protons (see figure 4.7). This is because hadronic showers develop deeper in the calorimeter than electromagnetic cascades.
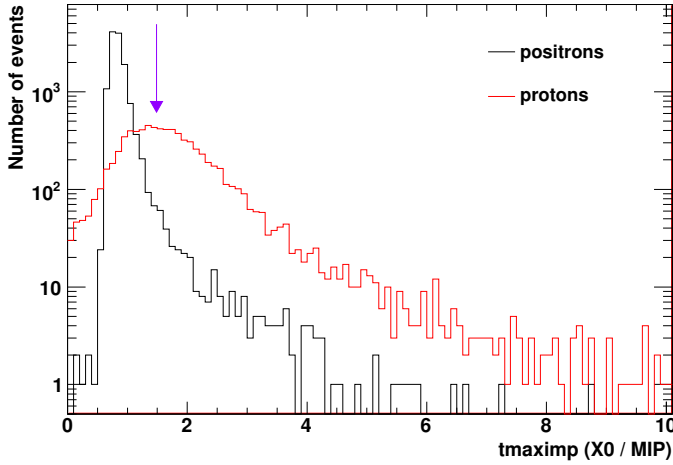
Figure 4.7. Distribution of the variable *tmaximp* for simulated positrons (black line) and protons in the *normal case* (red line). The violet arrow shows the cut $tmaximp < 1.5\ \mathrm{X_0/MIP}$ which selects $97.5\,\%$ of positrons and $43.2\,\%$ of protons. The distributions are obtained from simulated events in the energy range $20 - 100$ GeV.

The second selection is related to the starting point of the shower. The variable *noint* is defined as follows:

$$noint = \sum_{j=1}^{2} \sum_{i=1}^{22} \theta(i,j) \cdot i \qquad (4.1)$$

where $\theta(i,j) = 1$ if the deposited energy is typical of a proton (~ 1 MIP) within 4 mm from the reconstructed shower axis, otherwise $\theta(i,j) = 0$. The final value is evaluated summing over all the 22 calorimeter tungsten planes and for both the *x-view* and *y-view*. The *noint* value increases as the interactions start deeper in the calorimeter: thus, it assumes low values for electromagnetic showers which have a high probability to start in the first three calorimeter planes.

4.5   The "Nature analysis" approach

As described in Chapter 3, showers induced by hadronic events differ significantly from those induced by electromagnetic ones. In the hadronic case the lateral profile is broader than in electromagnetic showers which also have a pronounced central core surrounded by a more diffuse halo.

Information about the energy deposit in a direction perpendicular to the shower axis is provided by the variable *q3*. This variable describes the fraction of calorimeter energy deposited in the strips closest to the shower axis as reconstructed by the tracker:

$$q3 = \frac{qtrack}{qtot} \tag{4.2}$$

where *qtrack* is the energy deposited in the strips along the track and in the neighbouring strips on each side and *qtot* is the total energy detected in the calorimeter.

The selections described in section 4.4 have been used to produce the widely discussed[1] positron fraction published in the journal Nature [20] (see section 1.5.1). The selection approach primarily uses the longitudinal development and the starting point of the shower in the calorimeter in order to separate electromagnetic and hadronic events; furthermore, evaluating these variables in the upper and in the lower part of the calorimeter, a clean sample of protons and positrons was obtained. The procedure is the following: the 22 tungsten planes which constitute the calorimeter have been divided in two parts: the upper part from plane 1 to plane 20, and the lower part from plane 3 to plane 22. All the variables related to the calorimeter, i.e. the total detected energy and the shower profile variables, have been evaluated separately for both parts. Among positively charged events a clean sample of protons can be obtained selecting particles that do not interact in the first two planes, i.e. considering only the lower part of the calorimeter, since only 2 % of positrons with rigidities greater than 1.5 GV pass this condition [20]. For positron identification only variables evaluated in the upper part of the calorimeter have been used thus reducing the proton contamination. The number of electron and positron candidates in each energy interval was evaluated by fitting procedures of the calorimeter energy fraction *q3* [20]. Schubnell [47] argues that the rise in PAMELA positron fraction for energies greater than 10 GeV could be due to π^0 contamination of hadronic showers.

---

[1] There have been 607 citations to date, 28 - 9 - 2010, according to SPIRES.

In order to investigate this, the selections used in the Nature approach were applied to proton (*normal* and *only-π^0 case*) and positron simulated samples. The $q3$ distributions for the selected events are shown in the upper panels of figures 4.8, 4.9 and 4.10 and are plotted in three different rigidity ranges. Simulations show that distributions for protons in the *only-π^0 case* are well separated from those of positrons. The distributions related to simulated positrons and protons in the *only-π^0 case* have then been compared to the $q3$ distributions for positively charged particles in flight data selecting through the Nature approach (figures 4.8-*bottom*, 4.9-*bottom* and 4.10-*bottom*). In this procedure it has been assumed that all the positive particles in flight data are protons (the proton-to-positron flux ratio is $\sim 10^4$ at 100 GV). The $q3$ distribution for positively charged particles in flight data (red line) appear as a mixture of two components: one for $q3 < 0.5$ and one which lies around $q3 \sim 0.5 - 0.6$. This means that the $q3$ distribution for positively charged particles in flight data can not be explained considering only the $q3$ distribution for simulated protons in the *only-π^0 case*; thus, in order to fully describe it a considerable component of positrons must be introduced. The $q3$ distribution for simulated positrons well reproduces the distribution for positive flight data with $q3 \sim 0.5 - 0.6$. Furthermore, the distribution for simulated protons in the *only-π^0 case* is consistent with the proton component of the positive flight data thus indicating that an artificial increase of neutral pions does not drastically affect the hadronic shower development in the calorimeter and that it is still possible to obtain a clean sample of protons and positrons.

Looking at the $q3$ distribution for negatively charged particles in flight data selected as electrons in the upper part of the calorimeter (figure 4.11) it is possible to see that a cut $q3 \geq 0.5$ selects about 99 % of electrons in all the three rigidity ranges. Thus, considering the comparison between flight positive particles and simulated protons in the *only-π^0 case*, the cut on $q3$ selects how many protons in this artificial configuration fake the positron distribution. The cut $q3 \geq 0.5$ was used in the rigidity range $28 - 42$ GV while the cut $q3 \geq 0.52$ was used in the rigidity ranges $42 - 65$ GV and $65 - 100$ GV.

Rigidity (GV)	p *only-π^0*	positive particles	p *only-π^0* / positive particles
28 - 42	$3 \, ^{+\,5}_{-\,2}$	71	$0.042 \, ^{+\,0.066}_{-\,0.030}$
42 - 65	$4 \, ^{+\,5}_{-\,3}$	39	$0.102 \, ^{+\,0.131}_{-\,0.067}$
65 - 100	$2 \, ^{+\,4}_{-\,2}$	19	$0.105 \, ^{+\,0.226}_{-\,0.086}$

Table 4.5. Number of events selected by the cuts listed in section 4.4 for simulated protons in the *only-π^0 case* and for positive charged particles in flight data in three different rigidity ranges (related to bottom plots of figures 4.8, 4.9 and 4.10). Also, the cut $q3 \geq 0.5$ was used in the rigidity range $28 - 42$ GV and the cut $q3 \geq 0.52$ was used in the rigidity ranges $42 - 65$ GV and $65 - 100$ GV. The last column shows how many protons in this artificial configuration can fake the positron $q3$ distribution. The errors have been evaluated at 90 % confidence level.
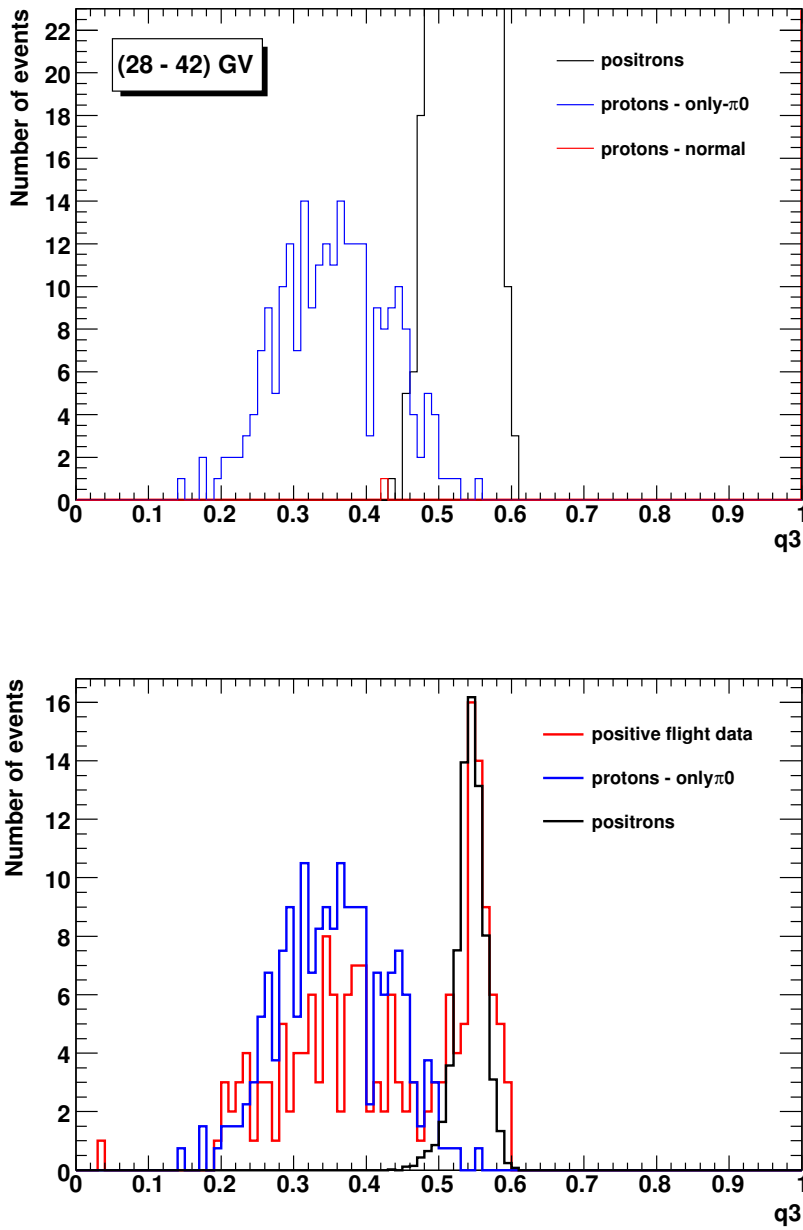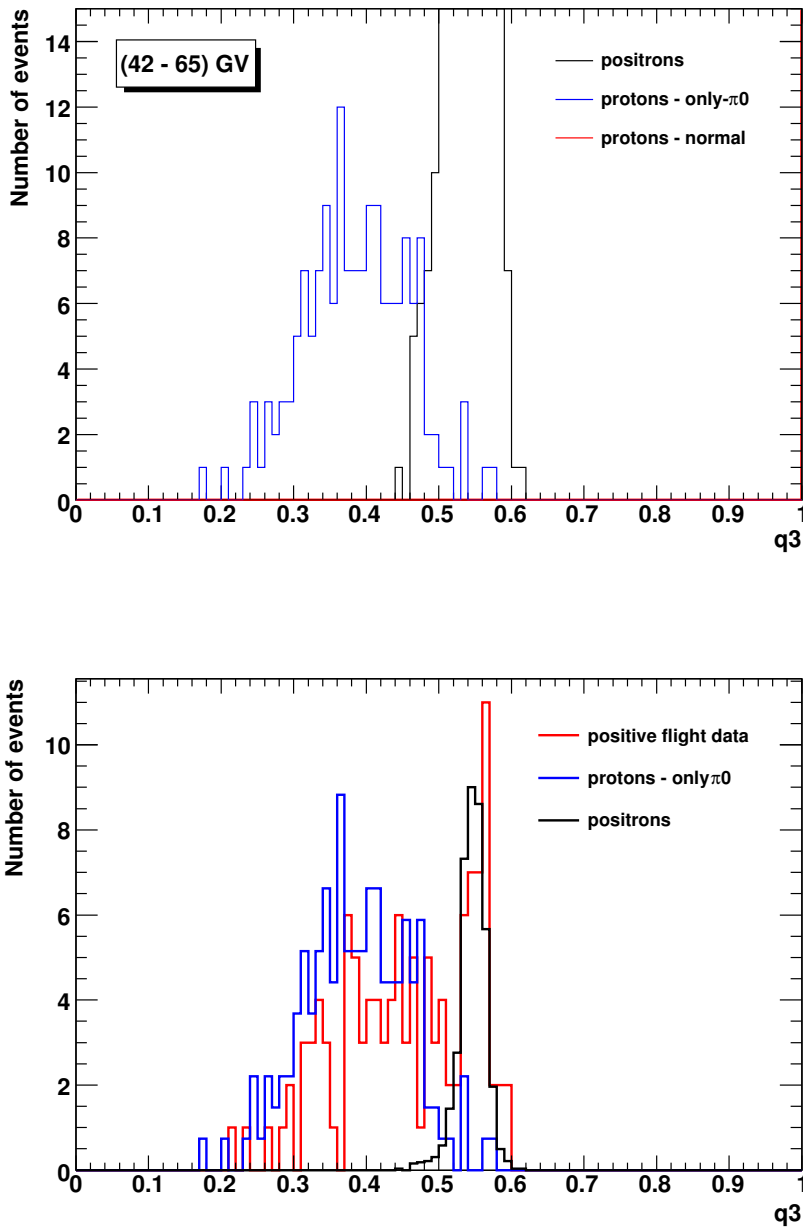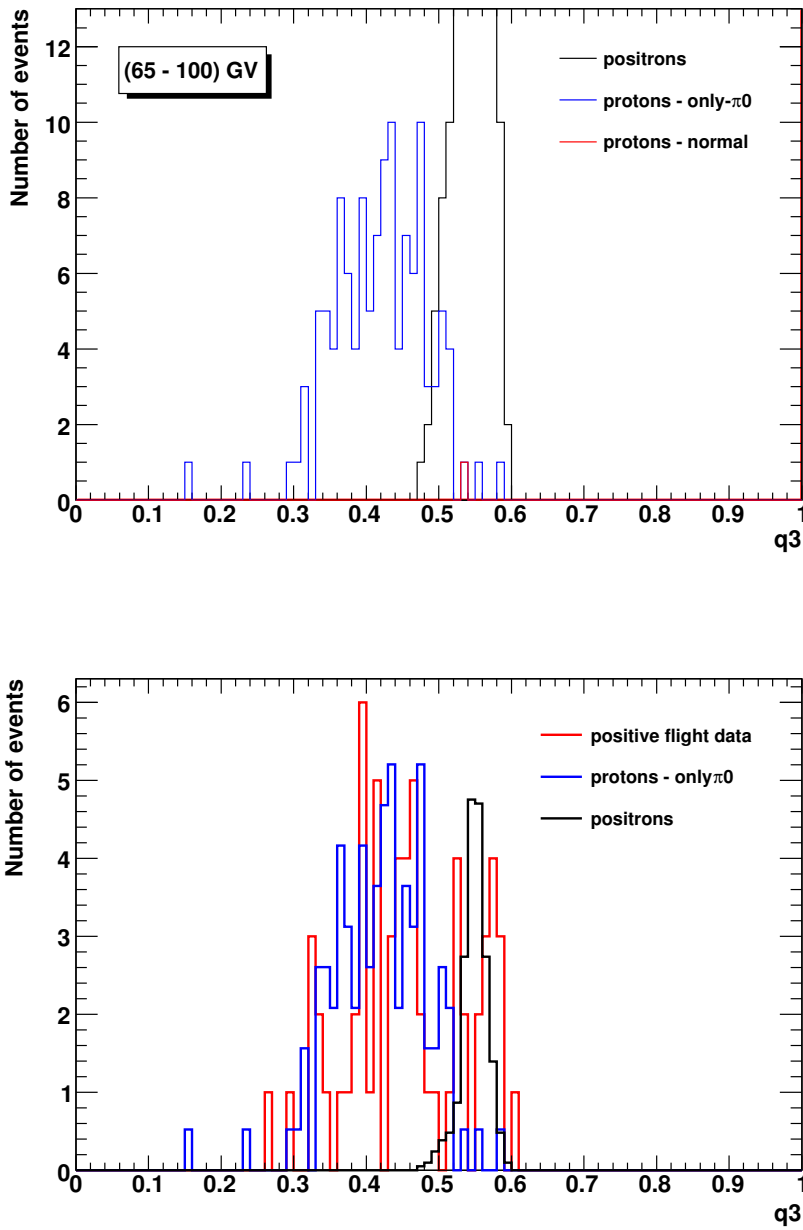
Figure 4.8. Calorimeter energy fraction in the rigidity range $28 - 42$ GV. *Top*: *q3* distribution for simulated positron and proton events (*normal* and *only-π^0 case*). *Bottom*: *q3* distribution for simulated positron (black line) and proton events in the *only-π^0 case* (blue line) compared to the *q3* distribution for positive charged particles in flight data (red line). The *q3* distributions for simulated positron and proton events are normalized to the *q3* distribution for flight positive particles.

Figure 4.9. Calorimeter energy fraction in the rigidity range $42 - 65$ GV. *Top*: *q3* distribution for simulated positron and proton events (*normal* and *only-π^0 case*). *Bottom*: *q3* distribution for simulated positron (black line) and proton events in the *only-π^0 case* (blue line) compared to the *q3* distribution for positive charged particles in flight data (red line). The *q3* distributions for simulated positron and proton events are normalized to the *q3* distribution for flight positive particles.

Figure 4.10. Calorimeter energy fraction in the rigidity range $65 - 100$ GV. *Top*: *q3* distribution for simulated positron and proton events (*normal* and *only-π^0 case*). *Bottom*: *q3* distribution for simulated positron (black line) and proton events in the *only-π^0 case* (blue line) compared to the *q3* distribution for positive charged particles in flight data (red line). The *q3* distributions for simulated positron and proton events are normalized to the *q3* distribution for flight positive particles.
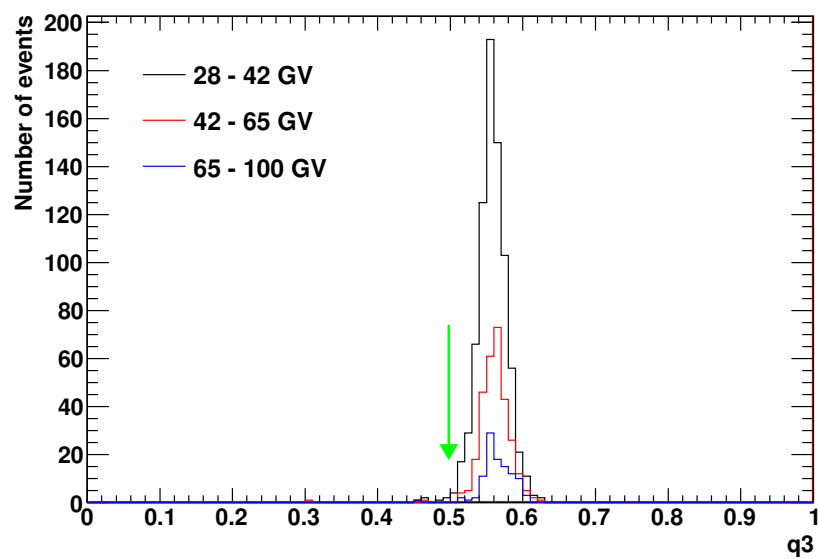
Figure 4.11. $q3$ distribution for negative charged particles in flight data selected as electrons in the upper part of the calorimeter and in the rigidity range 28 - 42 GV (black line), 42 - 65 GV (red line), 65 - 100 GV (blue line). The green arrow shows the cut $q3 \geq 0.5$ which selects 99 % of electrons.

Furthermore, the positron fraction can be evaluated for each rigidity range and the results are shown in table 4.6. The number of positrons N_{e+} is evaluated as difference between positive flight particles and simulated protons in the *only-π^0 case* (see table 4.5) and the number of electrons N_{e-} are negatively charged particles in flight data selected by $q3 \geq 0.5$ (in the range $28 - 42$ GV) and $q3 \geq 0.52$ (in the ranges $42 - 65$ GV and $65 - 100$ GV). The last column shows the positron fraction values published in Nature [20]. The comparison between the positron fraction evaluated in this artificial configuration with the positron fraction published in Nature is also shown in figure 4.12: the agreement is good thus indicating that the rise in the positron fraction for energies greater than 10 GeV is not due to misidentified positrons from π^0 contamination.

Rigidity (GV)	N_{e+}	N_{e-}	$N_{e+} / (N_{e+} + N_{e-})$	$N_{e+} / (N_{e+} + N_{e-})$
28 - 42	$68 ^{+ 14}_{- 13}$	780	$0.080 ^{+ 0.016}_{- 0.015}$	0.0831 ± 0.0093
42 - 65	$35 ^{+ 11}_{- 10}$	292	$0.107 ^{+ 0.031}_{- 0.029}$	$0.106 ^{+ 0.022}_{- 0.023}$
65 - 100	$17 ^{+ 8}_{- 7}$	101	$0.144 ^{+ 0.061}_{- 0.054}$	$0.137 ^{+ 0.048}_{- 0.043}$

Table 4.6. Values of the positron fraction in three different rigidity ranges. The number of positrons N_{e+} is evaluated as difference between positive flight particles and simulated protons in the *only-π^0 case* (see table 4.5); the number of electrons N_{e-} are negatively charged particles in flight data selected by $q3 \geq 0.5$ in the rigidity range $28 - 42$ GV and by $q3 \geq 0.52$ in the rigidity ranges $42 - 65$ GV and $65 - 100$ GV; the errors have been evaluated at 90 % confidence level. The last column shows the positron fraction values published in Nature [20].

The conclusions of this analysis can be summarized as follows:

- the approach followed in the Nature analysis permits a clean sample of positrons and protons to be selected; this clearly appears in the $q3$ distribution of positively charged particles in flight data which can be fully described considering two components: these components are well reproduced by simulations of protons in the *only-π^0 case* and positrons (see figures 4.8, 4.9 and 4.10);

- even in the artificial case when all the charged pions are converted into neutral ones, it is impossible to reproduce a double peaked $q3$ distribution and the distribution is still consistent with the proton component of the positive flight data; π^0 contamination can therefore be excluded;

- the positron fraction evaluated from proton simulations in the *only-π^0 case* is compatible with the positron fraction values published in Nature [20] (see table 4.6 and figure 4.12); thus the rise in the positron fraction for energies greater than 10 GeV is not due to misidentified positrons from π^0 contamination as argued by Schubnell [47];

- the discrimination between positron and proton events following the Nature approach becomes problematic at energies around 100 GeV.
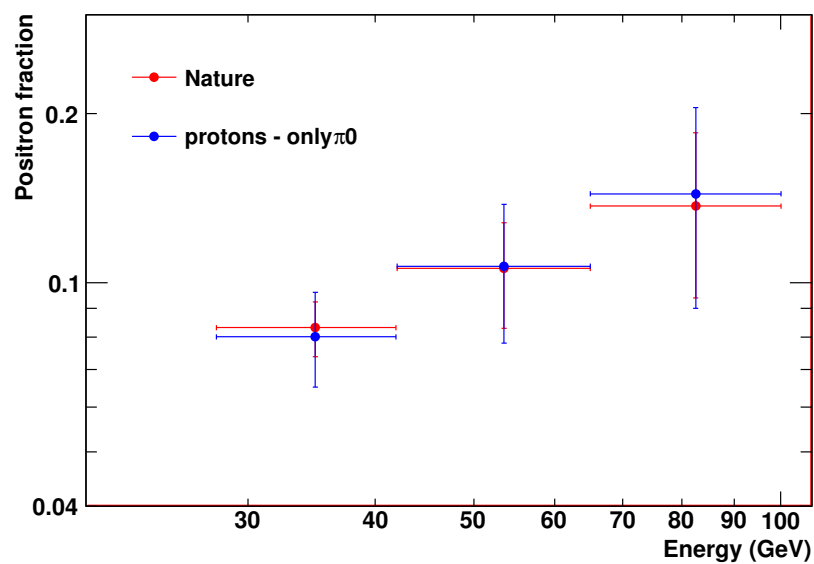
Figure 4.12. Positron fraction as function of the energy evaluated using simulations of protons in the *only-π^0 case* (blue points) compared to the values published in Nature [20] (red points); the values with errors are listed in table 4.6. The full version of the positron fraction measured by the PAMELA experiment is shown in figure 1.9 [20].

The remainder of this chapter describes a method to improve positron selection in the calorimeter in this *only-π^0 case* configuration and to find out what shower profile variables permit to select positrons in an efficient way with the less proton contamination.

4.6   A new approach for positron identification

As described in section 3.4.1, shower profile variables assume different values in hadronic and electromagnetic showers (see also figures 3.7, 3.8, 3.9, 3.10 and 3.11). Thus, these variables could be very efficient in selecting proton or positron events.

Variable distributions for both proton and positron events have been studied in a detailed way in order to obtain an efficient positron selection. In particular, the goal of this selection study is to answer the following questions:

- is it possible to discriminate between positrons and protons (*only-π^0 case*) in an efficient way?

- what are the shower profile variables which permit the most efficient selection?

All the shower profile variables depend on the reconstructed rigidity of the simulated particles. Thus, in order to identify which variables permit the most efficient discrimination between positrons and protons, distributions of variables versus the reconstructed rigidity have been studied. Figure 4.13 shows the ratio between the energy deposited in a cylinder of radius 8 silicon strips around the shower axis, *qcyl*, and the number of strips hit inside the same cylinder, *ncyl*. The proton and positron distributions are well separated and a cut of *qcyl / ncyl > 8* selects 99.1 % of positrons and 1.0 % of protons.

The first step in this procedure was to choose shower profile variables for which distributions as function of the rigidity are well separated between positron and proton simulated events (as in figure 4.13). Then, the *CALCHI* variable was constructed using different shower profile variables combinations in order to find the one that selects positrons in the most efficient way.

The variable *CALCHI* is constructed in the following way:

$$CALCHI = \sum_{i=1}^{n} \chi^2_{variable[i]} = \sum_{i=1}^{n} \frac{(variable[i] - \overline{variable[i]})^2}{\sigma^2_{variable[i]}} \qquad (4.3)$$

where n is the number of shower profile variables considered.

For each variable, the mean and the standard deviation values are functions of the tracker reconstructed rigidity. For instance, figure 4.14 shows the distribution of the variable *q2* as function of the rigidity for simulated positrons in the energy range $20 - 100$ GeV; *q2* is the ratio between the energy deposited in the neighbouring strips on each side along the track and the energy deposited in a cylinder of radius 4 strips around the shower axis. Observing this plot in slices along the rigidity x-axis, the values of *q2* follow a gaussian distribution with a certain mean and standard
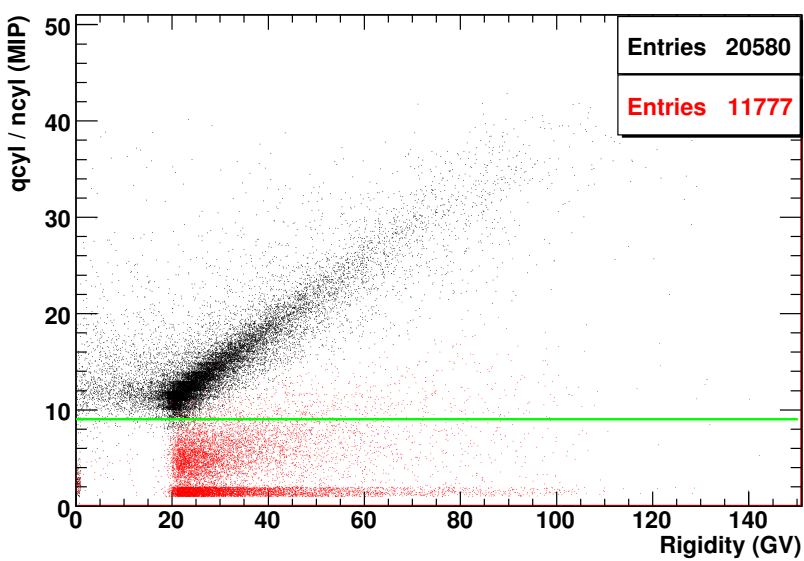
Figure 4.13. Distribution of *qcyl/ncyl* as function of the reconstructed rigidity for simulated positrons (black points) and protons *normal case* (red points) in the energy range $20 - 100$ GeV. The green line shows the cut *qcyl/ncyl* > 8 which selects 99.1 % of positrons and 1.0 % of protons.

deviation in each rigidity bin. The distribution of the $q2$ variable in the rigidity bin $30 - 31$ GV is shown in figure 4.15 and is well described by a gaussian distribution. This procedure was repeated for each rigidity bin, thus obtaining a distribution of $\overline{q2}$ and σ_{q2} as function of the rigidity (figure 4.16). Both these distributions have been fitted with a straight line in the reconstructed rigidity range $(20 - 100)$ GV and the best fit equations are respectively:

$$\overline{q2} = 0.6634 + 0.0001213 \cdot rigidity \tag{4.4}$$

$$\sigma_{q2} = 0.02085 - 0.0001339 \cdot rigidity \tag{4.5}$$

The same procedure as illustrated for the variable $q2$ has been applied to other shower profile variables. The distributions of $\overline{variable[i]}$ and $\sigma_{variable[i]}$ have been fitted mostly with linear or exponential functions.
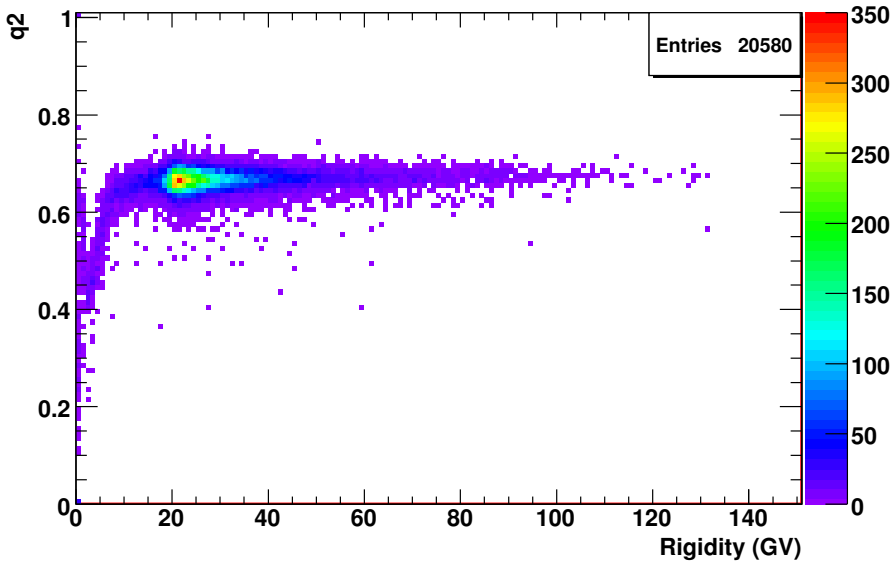
Figure 4.14. Distribution of the $q2$ variable as function of the rigidity for simulated positrons in the energy range $20 - 100$ GeV.

4.7   Positron selection efficiencies

As already mentioned in section 4.6 selection criteria on shower profile variables have been studied in order to obtain an efficient positron selection. Positron selection criteria have been tuned on simulated positron samples in order to obtain a good positron selection efficiency. These same positron selection criteria have
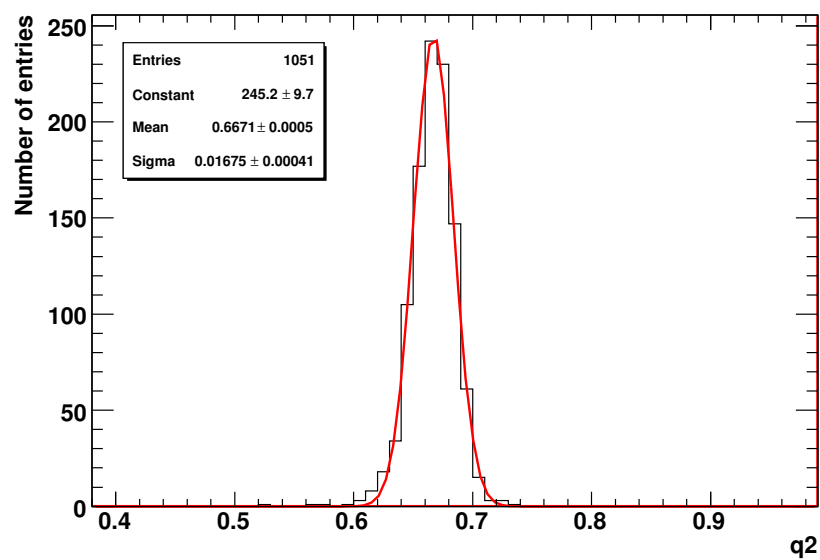
Figure 4.15. Distribution of the *q2* variable in the rigidity bin $30 - 31$ GV for simulated positrons in the energy range $20 - 100$ GeV (black line). The values are well approximated by a gaussian distribution (red line).
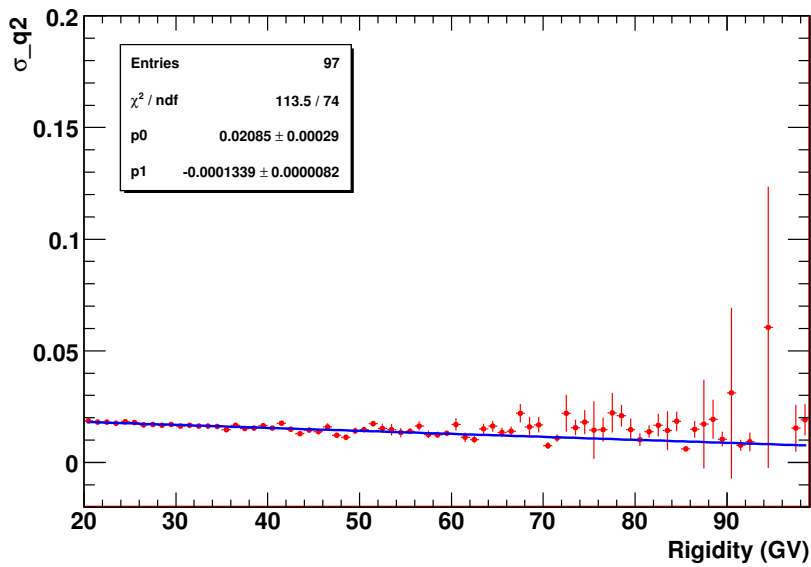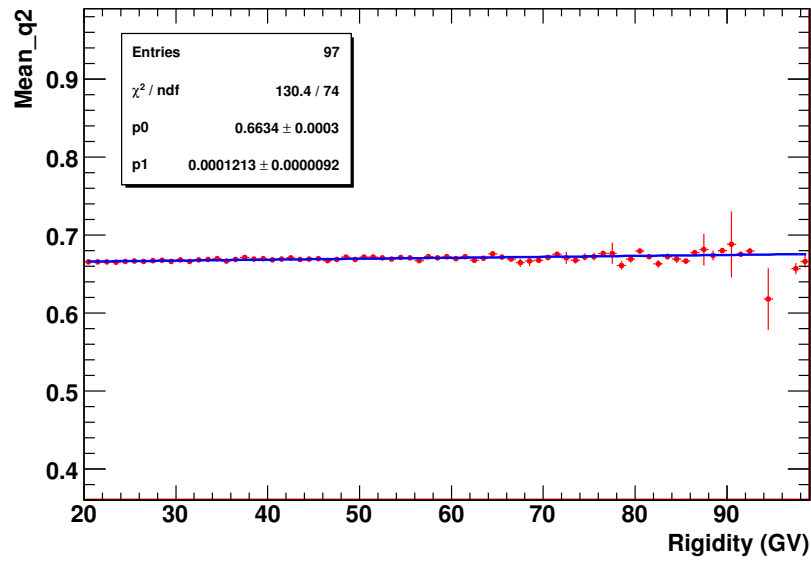
Figure 4.16. *Top*: distribution of mean values $\overline{q2}$ as function of the reconstructed rigidity (red points); the best fit is also shown (blue line) and has equation: $\overline{q2} = 0.6634 + 0.0001213 \cdot$ rigidity. *Bottom*: distribution of σ_{q2} as function of the reconstructed rigidity (red points); the best fit is also shown (blue line) and has equation: $\sigma_{q2} = 0.02085 - 0.0001339 \cdot$ rigidity.

then been applied to proton simulation samples (both *normal* and *only-π^0 case*) in order to study the electromagnetic contamination of hadronic showers, i.e. how many protons are detected as positrons. The combination which selects positrons with the highest efficiency and with the lowest proton contamination (see section 4.9) was found to be:

1. $\overline{ncore} - 3 \cdot \sigma_{ncore} < ncore < \overline{ncore} + 3 \cdot \sigma_{ncore}$

2. $ncyl > \overline{ncyl} - 3 \cdot \sigma_{ncyl}$

3. $\overline{qcyl/ncyl} - 3 \cdot \sigma_{qcyl/ncyl} < qcyl/ncyl < \overline{qcyl/ncyl} + 3 \cdot \sigma_{qcyl/ncyl}$

4. $qpresh > 50$

5. $qtot/nstrip > 6$

6. $CALCHI < CALCHI_{cut}$

where

$$CALCHI = \sum_{i=1}^{6} \chi^2_{variable[i]}$$
$$= \chi^2_{ncore} + \chi^2_{q3} + \chi^2_{qpresh} + \chi^2_{ncyl} + \chi^2_{qcyl/ncyl} + \chi^2_{qtot/nstrip} \qquad (4.6)$$

Thus, selections *1* and *2* listed in section 4.4.4 have been substituted by these new six cuts.

Figures 4.17 and 4.18 show distributions of *ncyl*, *qcyl/ncyl*, *qpresh* and *qtot/nstrip* for simulated positrons and protons; the cuts used for selecting positrons are also displayed.

The cut on the *CALCHI* variable dominates the selection efficiency and many combinations of different shower profile variables have been used in order to obtain the best positron selection efficiency with the smallest proton contamination (see section 4.9). By definition (equation 4.3) *CALCHI* is a χ^2 distribution with n degrees of freedom, where n is the number of shower profile variables considered. In this case (equation 4.6) *CALCHI* is constructed using six variables: thus, if the six variables are totally independent the probability for a χ^2 distribution to be ≤ 6 for 6 degrees of freedom is ~ 60 %. Figure 4.19 shows the *CALCHI* distribution (*top*) and the *CALCHI* distribution as a function of the reconstructed rigidity (*bottom*). The distribution shows a peak around $CALCHI = 2$ and a cut $CALCHI < 6$ selects 55.4 % of the events.

Using all the selections described in section 4.4 the selection efficiencies of the cuts described above were studied for different values of $CALCHI_{cut}$. The positron selection efficiency is given by the ratio between the cuts listed above and those listed in section 4.4. The number of positrons which pass the cuts listed in section 4.4 are 20581 ± 229 at 90 % confidence level for 10^5 simulated positrons. Figure 4.20-*top* shows the trend of the selection efficiencies for different values of $CALCHI_{cut}$ for simulated positrons in the energy range $20 - 100$ GeV. Thus,
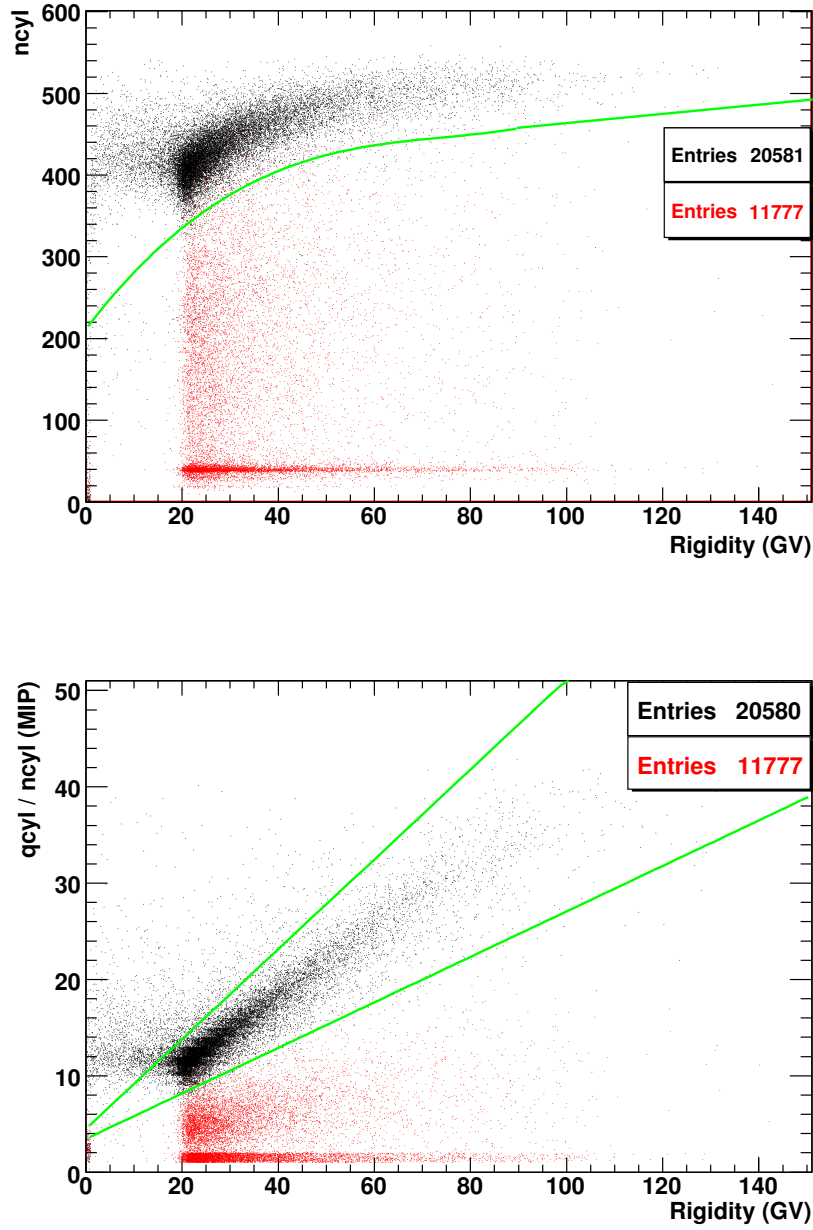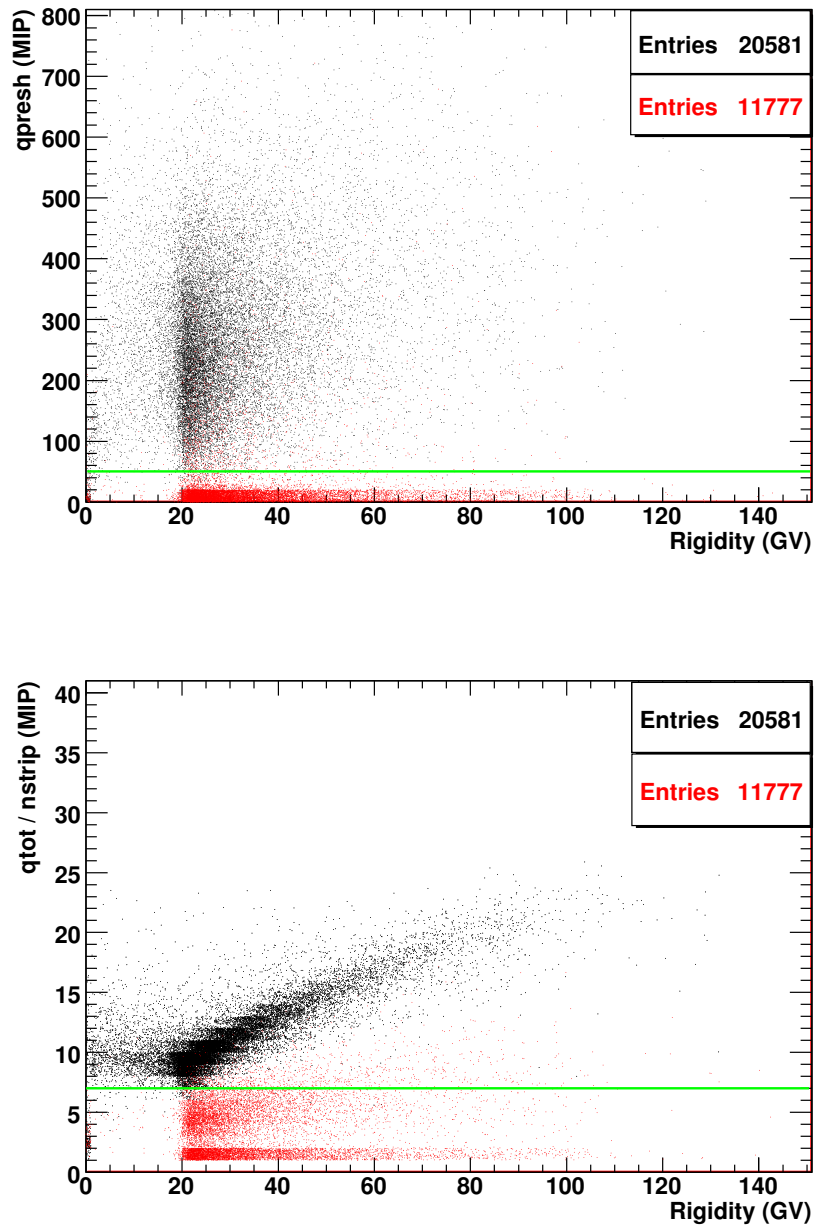
Figure 4.17.   *Top*:   distribution of *ncyl* as function of the reconstructed rigidity for positrons (black points) and protons *normal case* (red points); the green line shows the selection $ncyl > \overline{ncyl} - 3 \cdot \sigma_{ncyl}$.   *Bottom*: distribution of *qcyl/ncyl* as function of the reconstructed rigidity for positrons (black points) and protons *normal case* (red points); the green line shows the selection $\overline{qcyl/ncyl} - 3 \cdot \sigma_{qcyl/ncyl} < qcyl/ncyl < \overline{qcyl/ncyl} + 3 \cdot \sigma_{qcyl/ncyl}$.

Figure 4.18. *Top*: distribution of *qpresh* as function of the reconstructed rigidity for positrons (black points) and protons *normal case* (red points); the green line shows the selection *qpresh* > 50. *Bottom*: distribution of *qtot/nstrip* as function of the reconstructed rigidity for positrons (black points) and protons *normal case* (red points); the green line shows the selection *qtot/nstrip* > 6.
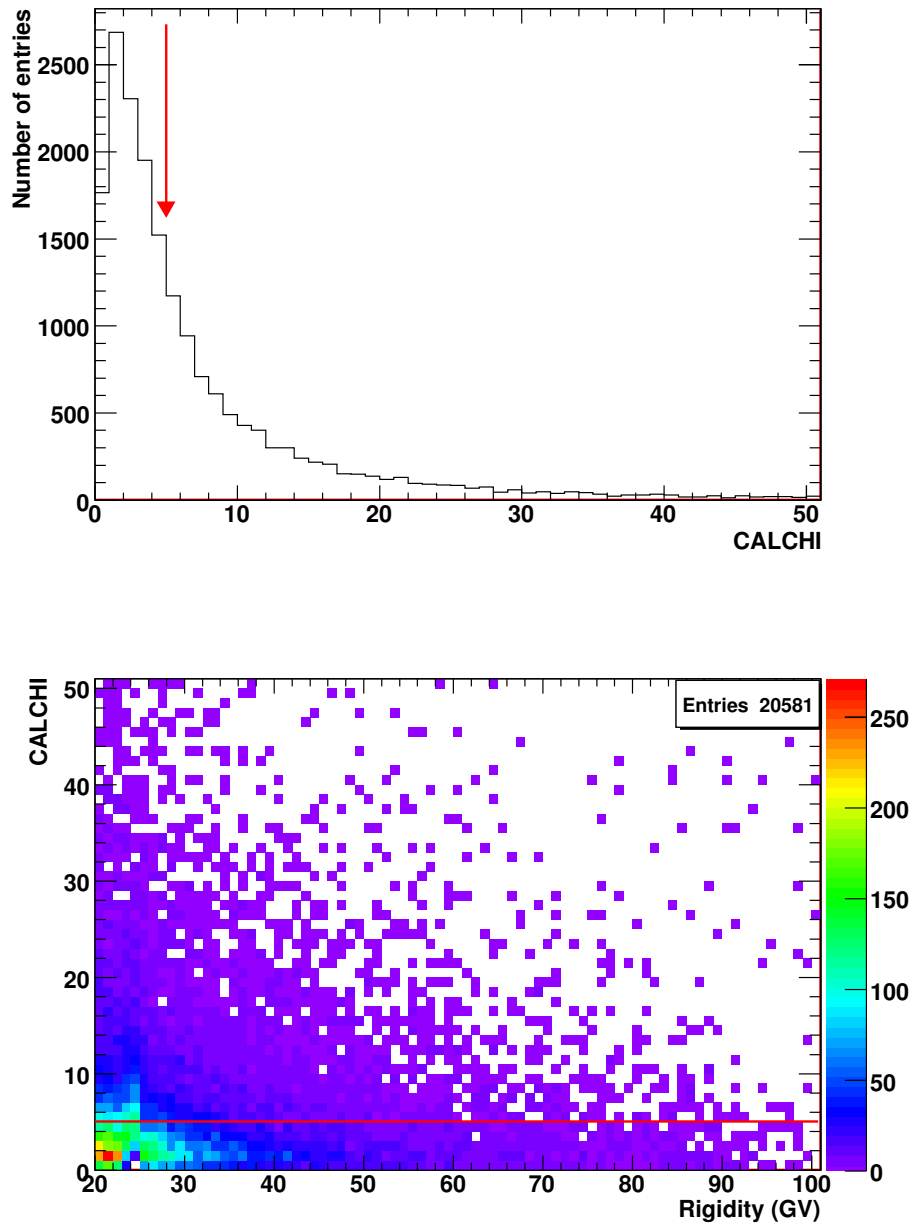
Figure 4.19. *Top*: distribution of the *CALCHI* variable for simulated positrons in the energy range $20 - 100$ GeV; the red arrow shows $CALCHI = 5$. *Bottom*: distribution of the *CALCHI* variable as function of the reconstructed rigidity for simulated positrons in the energy range $20 - 100$ GeV; the red line shows $CALCHI = 5$. The cut $CALCHI < 5$ selects 49.7 % of the events as positrons.

choosing for instance a value of $CALCHI_{cut} = 5$, the positron selection efficiency is ~ 0.50. Some results for different values of $CALCHI_{cut}$ shown in figure 4.20-*top* are also summarized in table 4.7.
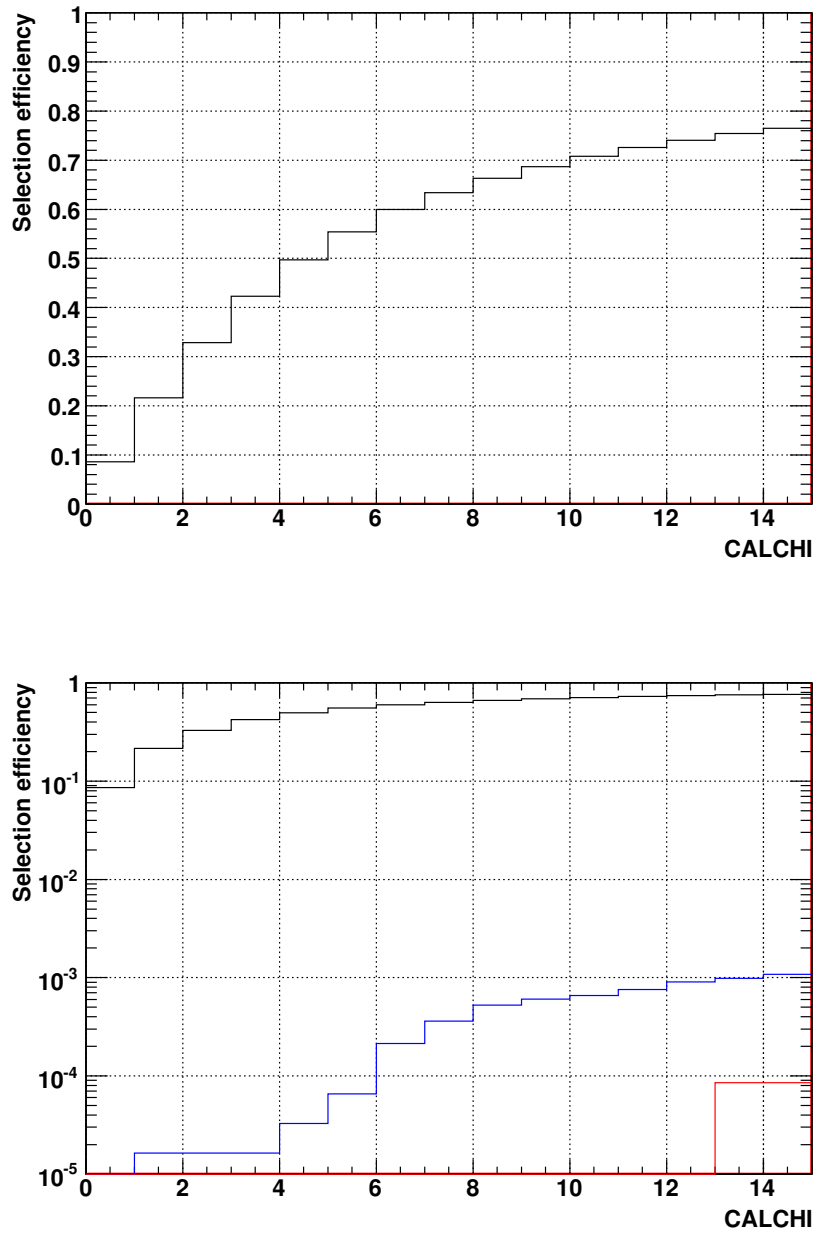
Figure 4.20. Selection efficiency as function of cut values on the *CALCHI* variable and for simulation in the energy range $20 - 100$ GeV. *Top*: positrons selection efficiency. *Bottom*: positrons selection efficiency (black line) compared to the protons selection efficiency in the *normal case* (red line) and in the *only-π^0 case* (blue line).

4.8 Proton contamination

The same selections described in sections 4.4 and 4.7, previously applied to simulated positrons, have been then applied to simulated protons in order to study the contamination, i.e. how many protons pass the positron cuts. Figure 4.20-*bottom* shows the trend of the selection efficiency as function of $CALCHI_{cut}$ for protons in the *normal case* (red line) and in the *only-π^0 case* (blue line) together with the positron selection efficiency (black line) already displayed in figure 4.20-*top*. In this case, the proton selection efficiency is given by the ratio between the number of proton events which pass the cuts listed in section 4.7 and those which pass the cuts listed in section 4.4. Simulating 10^5 protons in the *normal case* and $5 \cdot 10^5$ protons in the *only-π^0 case* the number of protons in the two cases which pass the cuts listed in section 4.4 are respectively 11777 ± 173 and 60975 ± 395 at 90 % confidence level. Observing figure 4.20-*bottom* one can notice that:

- no proton events are selected as positrons in the *normal case* up to high $CALCHI_{cut}$ values (> 13);

- the number of proton events selected as positrons in the *only-π^0 case* is of order of 10^{-5} for $CALCHI_{cut} < 6$.

Furthermore, for each value of $CALCHI_{cut}$ the proton contamination is evaluated considering the corresponding positron selection efficiency:

$$\text{proton contamination} = \frac{\text{proton selection efficiency}}{\text{positron selection efficiency}} \quad (4.7)$$

Some results for different $CALCHI_{cut}$ values are summarized in table 4.7.

Only-π^0 case			
$CALCHI_{cut}$	e$^+$ efficiency	p efficiency	proton contamination
3	0.328 ± 0.006	$(1.6 \; {}^{+ \; 6.0}_{- \; 1.5}) \cdot 10^{-5}$	$(0.49 \; {}^{+ \; 1.84}_{- \; 0.46}) \cdot 10^{-4}$
4	0.423 ± 0.007	$(1.6 \; {}^{+ \; 6.0}_{- \; 1.5}) \cdot 10^{-5}$	$(0.49 \; {}^{+ \; 1.84}_{- \; 0.46}) \cdot 10^{-4}$
5	0.497 ± 0.008	$(3.3 \; {}^{+ \; 7.1}_{- \; 2.7}) \cdot 10^{-5}$	$(0.66 \; {}^{+ \; 1.42}_{- \; 0.54}) \cdot 10^{-4}$
6	0.554 ± 0.008	$(6.6 \; {}^{+ \; 8.5}_{- \; 4.3}) \cdot 10^{-5}$	$(1.19 \; {}^{+ \; 1.53}_{- \; 0.77}) \cdot 10^{-4}$
7	0.600 ± 0.009	$(2.1 \pm 1.0) \cdot 10^{-4}$	$(3.50 \pm 1.67) \cdot 10^{-4}$
8	0.634 ± 0.009	$(3.6 \pm 1.3) \cdot 10^{-4}$	$(5.68 \pm 2.05) \cdot 10^{-4}$

Table 4.7. Proton selection efficiency and proton contamination for different values of $CALCHI_{cut}$. The analysis was performed on $5 \cdot 10^5$ simulated protons in the *only-π^0 case* and in the energy range $20 - 100$ GeV. The errors have been evaluated at 90 % confidence level. The number of protons which passes the cuts listed in section 4.4 are 60975 ± 395 at 90 % confidence level.

Thus, choosing a value of $CALCHI_{cut} = 5$ no contamination is found for simulated protons in the *normal case* while a contamination of $6.6 \cdot 10^{-5}$ is found for protons in the *only-π^0 case*. Using this kind of analysis some conclusions can be summarized as follows:

- the shower profile variables *ncore, q3, qpresh, ncyl, qcyl/ncyl* and *qtot/nstrip* permit an efficient positron selection (~ 0.50 considering a $CALCHI_{cut} = 5$);

- the shower profile variables used for positron selection yield no proton contamination in the *normal case* sample;

- considering that the proton-to-positron flux ratio at 100 GV is approximately 10^4 [20] the proton contamination should be lower than $\sim 10^{-5}$; the proton contamination in the *only-π^0 case* sample is of order of 10^{-5} with a corresponding positron selection efficiency of ~ 0.50, i.e. the discrimination between positrons and protons is quite good considering the fact that this is an artificial case where all the charged pions are converted into neutral ones and thus the contamination should be highest.

4.9 Conclusions and outlook

The analysis presented in this chapter was performed on simulated events generated by using a Monte Carlo program developed by the PAMELA Collaboration and based on the GEANT 3.21 code. The aim was to study the electromagnetic component inside hadronic cascades, usually initiated by neutral pions during hadronic interactions in the calorimeter. η mesons can also initiate an electromagnetic shower but they were not considered in this thesis (see section 3.3). Furthermore, the simulation code was modified in order to artificially increase the number of π^0 in hadronic showers and study the consequences for positron identification. The simulated events produced are listed in table 4.4. The analysis consisted of two parts:

- evaluate the neutral pion contamination in the positron selection when following the Nature approach (section 4.5);

- study a new approach for positron identification based on shower profile variables in the calorimeter (section 4.6) and evaluate the corresponding proton contamination.

The results show that the Nature approach selects a mixture of two distributions which is still correct even when the number of π^0s in hadronic showers is artificially boosted (*only-π^0 case* simulations). The positron fraction evaluated considering this artificial case is in good agreement with the positron fraction published in Nature [20]. Thus, it is unlikely that the rise in the PAMELA positron fraction for energies greater than 10 GeV is due to π^0 contamination of hadronic showers, as argued by Schubnell [47].

The Nature approach starts being less efficient in the last energy range considered (65 − 100 GeV) and probably it would be difficult to apply this method at higher energies. In view of improving positron selection for energies greater than 100 GeV and up to ∼ 300 GeV (see table 2.1), a new approach based on selections on shower profile variables was studied and tested on simulations in the energy range 20 − 100 GeV. Some results of this analysis are summarized in table 4.7. This method permit to obtain a positron selection efficiency of ∼ 0.50 with a corresponding proton contamination of order of 10^{-5} in the energy range 20 − 100 GeV. This new approach, which uses transverse shower profile variables in the calorimeter, is efficient in discriminating between positrons and protons and it will be tested at higher energies, up to 300 GeV. At these energies the method can be still handled in an efficient way even if probably new shower profile variables should be considered.

The next step in the analysis will be to apply the new positron selection approach on positive charged particles in flight data and reproduce the positron fraction. It has been proved that this method is efficient in selecting a clean positron sample in the energy range 20 − 100 GeV and it is planned to be studied at higher energies.

Acknowledgments

First of all, I want to thank Prof. Mark Pearce to have accepted me as a PhD student in the Astroparticle and Particle Physics group at KTH in 2007 and for all the support in the daily work. Funding received from the Swedish National Space Board for my PhD position is gratefully acknowledged.

I would like to thank all the persons in the PAMELA Collaboration. A special thanks goes to Mirko Boezio for his continuous help during the work at this thesis, to Emiliano Mocchiutti for having answered all my questions and doubts, and to Francesco Cafagna and Alessandro Bruno for having helped me with the simulations. My thanks also to the PAMELA group at KTH (Per, William, Juan and Petter) for all the help and the interesting discussions.

I would like to thank all the people working in the Astroparticle and Particle Physics group at KTH for all the nice time and funny lunches we shared together. A particular thanks to my office colleagues, Mózsi and Oscar, for sharing the daily work in a really nice atmosphere. To Cecilia: thank you so much for all your help!

Thanks to all the people that lived with me in the corridor in Lappis (Amanuensvägen 5, first floor): it was really a pleasure to meet all of you guys and I really enjoyed living together as a big family. To Bego, Ingeborg, Usman, Pierre, Catarina, Pia, Marc and Ellen: thank you so much for your great friendship!

Agli amici di Torino: anche se da lontano, grazie mille per il vostro continuo sostegno.

Infine, ringrazio la mia famiglia per tutto l'aiuto datomi in questi tre anni di vita a Stoccolma. Papà e mamma: grazie per avermi sempre dato la forza di andare avanti, soprattutto nei periodi più difficili. Antonio: nonostante tutte le difficoltà affrontate, grazie per essermi sempre rimasto accanto, per i magnifici momenti trascorsi insieme e per avermi dato quella serenità che cercavo da tempo.

List of Figures

List of Tables

Bibliography

[1] M.S. Longair. *High energy astrophysics: particles, photons and their detection.* Cambridge University Press, vol.1, 1994.

[2] S.P. Swordy. *The energy spectra and anisotropies of cosmic rays.* Space Science Review, **99**: 85 – 94, 2001.

[3] J. Blümer for the Pierre Auger Collaboration. *Cosmic rays at the highest energies and the Pierre Auger Observatory.* Journal of Physics G, **29**: 867 – 879, 2003.

[4] F. Schüssler for the Pierre Auger Collaboration. *Measurement of the cosmic ray energy spectrum above 10^{18} eV using the Pierre Auger Observatory.* Proceeding for the 31st International Cosmic Rays Conference, Łódź 2009.

[5] M. Aglietta et al. *The cosmic ray primary composition in the "knee" region through the EAS electromagnetic and muon measurements at EAS-TOP.* Astroparticle Physics, **21**: 583 – 596, 2004.

[6] W.D. Apel et al. *Energy spectra of elemental groups of cosmic rays: Update on the KASCADE unfolding analysis.* Astroparticle Physics, **31**: 86 – 91, 2009.

[7] T. Antoni et al. *KASCADE measurements of energy spectra for elemental groups of cosmic rays: Results and open problems.* Astroparticle Physics, **24**: 1 – 25, 2005.

[8] A. Haungs et al. *Results on the cosmic ray energy spectrum measured with KASCADE-Grande.* Proceeding for the 31st International Cosmic Rays Conference, Łódź 2009.

[9] K. Greisen. *End to the cosmic-ray spectrum?* Physical Review Letters, **16**: 748 – 750, 1966.

[10] G.T. Zatsepin and V.A. Kuz'min. *Upper limit of the spectrum of cosmic rays.* JETP Letters, **4**: 78 – 80, 1966.

[11] J. Abraham et al. *Observation of the Suppression of the Flux of Cosmic Rays above 4×10^{19} eV.* Physical Review Letters, **101**: 061101–1 – 7, 2008.

[12] *http://www.srl.caltech.edu/ACE/ACENews/ACENews83.html.*

[13] *http://www.srl.caltech.edu/ACE/ace_mission.html.*

[14] M.S. Longair. *High energy astrophysics: stars, the Galaxy and the interstellar medium.* Cambridge University Press, vol.2, 1994.

[15] *http://jemeuso.riken.jp/en/about2.html.*

[16] A.W. Strong, I.V. Moskalenko, and V.S. Ptuskin. *Cosmic-Ray Propagation and Interaction in the Galaxy.* Annu. Rev. Nucl. Part. Sci., **57**: 285 – 327, 2007.

[17] A.W. Strong and I.V. Moskalenko. *Propagation of cosmic-ray nucleons in the galaxy.* The Astrophysical Journal, **509**: 212 – 228, 1998.

[18] N. Tomassetti on behalf of the AMS-01 Collaboration. *Measurement of the Cosmic ray B/C Ratio with the AMS-01 Experiment.* Proceeding for the 31st International Cosmic Rays Conference, Łódź 2009.

[19] D. Maurin, R. Taillet, and F. Donato. *New results on source and diffusion spectral features of Galactic cosmic rays: I B/C ratio.* Astronomy and Astrophysics, **394**: 1039 – 1056, 2002.

[20] O. Adriani et al. *Observation of an anomalous positron abundance in the cosmic radiation.* Nature, **458**: 607 – 609, 2009.

[21] *http://www.nmdb.eu/?q=node/138.*

[22] *http://neutronm.bartol.udel.edu/.*

[23] J.R. Jokipii and B. Thomas. *Effects of drift on the transport of cosmic rays.* The Astrophysical Journal, **243**: 1115 – 1122, 1981.

[24] I.V. Moskalenko and A.W. Strong. *Production and propagation of cosmic-ray positrons and electrons.* The Astrophysical Journal, **493**: 694 – 707, 1998.

[25] R.J. Protheroe. *On the nature of the cosmic ray positron spectrum.* The Astrophysical Journal, **254**: 391 – 397, 1982.

[26] S.W. Barwick et al. *Measurements of the cosmic-ray positron fraction from 1 to 50 GeV.* The Astrophysical Journal, **482**: L191 – L194, 1997.

[27] L. Zhang and K.S. Cheng. *Cosmic-ray positrons from mature gamma-ray pulsars.* Astronomy and Astrophysics, **368**: 1063 – 1070, 2001.

[28] M. Boezio et al. *PAMELA and indirect dark matter searches.* New Journal of Physics, **11**: 105023–1 – 25, 2009.

[29] D. Hooper, P. Blasi, and P.D. Serpico. *Pulsars as the sources of high energy cosmic ray positrons.* Journal of Cosmology and Astroparticle Physics, **0901**: 025, 2009.

[30] O. Adriani et al. *New Measurement of the Antiproton-to-Proton Flux Ratio up to 100 GeV in the Cosmic Radiation.* Physical Review Letters, **102**: 051101, 2009.

[31] Y. Asaoka et al. *Measurements of Cosmic-ray Low Energy Antiproton and Proton Spectra in a Transient Period of Solar Field Reversal.* Phys. Rev. Lett., **88**: 051101, 2002.

[32] J. Clem and P. Evenson. *Cosmic Ray Positron Fraction Observations During the A- Magnetic Solar Minimum.* Proceeding for the 30th International Cosmic Rays Conference, Merida 2007.

[33] T. Delahaye et al. *Galactic secondary positron flux at the Earth.* Astronomy and Astrophysics, **501**: 821 – 833, 2009.

[34] PAMELA Collaboration. *To be published.*

[35] M. Kamionkowski and M.S. Turner. *Distinctive positron feature from particle dark-matter annihilations in the galactic halo.* Phys. Rev., D **43**: 1774 – 1780, 1991.

[36] L. Bergström, T. Bringmann, and J. Edsjö. *New Positron Spectral Features from Supersymmetric Dark Matter - a Way to Explain the PAMELA Data?* Physical Review, D **78**: 103520, 2008.

[37] H.C. Cheng, J.L. Feng, and K.T. Matchev. *Kaluza-Klein Dark Matter.* Physical Review Letters, **89**: 211301–1 – 4, 2002.

[38] P. Picozza et al. *PAMELA - A payload for antimatter matter exploration and light-nuclei astrophysics.* Astroparticle Physics, **27**: 296 – 315, 2007.

[39] G. Osteria et al. *The time-of-flight system of the PAMELA experiment on satellite.* Nucl. Inst. and Meth., **A 535**: 152 – 157, 2004.

[40] O. Adriani et al. *The magnetic spectrometer of the PAMELA satellite experiment.* Nucl. Inst. and Meth., **A 511**: 72 – 75, 2003.

[41] *http://pamela.roma2.infn.it.*

[42] O. Adriani et al. *The magnetic spectrometer of the PAMELA experiment: on-ground test of the flight-model.* 29th International Cosmic Ray Conference, Pune, **00**: 101 – 104, 2005.

[43] M. Boezio et al. *High granularity imaging calorimeter for cosmic rays physics.* Nucl. Inst. and Meth., **A 487**: 407 – 422, 2002.

[44] Particle Data Group. *Review of Particle Physics.* Physics Letters, **B 667**: 1, 2008.

[45] R. Wigmans. *Calorimetry, Energy Measurement in Particle Physics.* Oxford science publications, 2000.

[46] B. Rossi. *High-Energy Particles.* Englewood Cliffs, N.J.: Prentice Hall, 1952.

[47] M. Schubnell. *The cosmic-ray positron and electron excess: an experimentalist's point of view.* arXiv:0905.0444, 2009.

[48] R. Brun et al. *Detector Description and Simulation Tool.* CERN Program Library Long Writeup W5013, 1994.

[49] A. Bruno. *Cosmic ray antiprotons measured in the PAMELA experiment.* Ph.D. Thesis, Physics Department of University of Bari, Italy, 2008.